POLITECNICO DI TORINO

Facoltà di Ingegneria

CORSO DI LAUREA IN CIVIL ENGINEERING

Gabriele Milone

Numerical Study of Stress Identification in Concrete using Coda-Wave Interferometry

Tesi di Laurea Magistrale

Relatore:
Prof. Rosario Ceravolo

Correlatori:
Dr. Yuguang Yang
Dr. Cornelis Weemstra
Dr. Deyan Draganov

Anno Accademico 2018-2019

Abstract

Over the past few years, in the civil engineering field, the understanding of ultrasonic wave propagation and scattering has started to show useful and promising attributes aimed for heterogeneous media inspection. Among the several non destructive tests, the structural-health monitoring technique which exploits Coda-Wave Interferometry has recently found its breakthrough. Instead of being focused on the first arrivals, this theory employs the information carried by the late section of the signal which, combined with a probabilistic evaluation, allows to recover the stress changes in concrete. The use of ultrasonic coda-waves, however, still presents some room for improvement; the thesis aimed at highlighting, solving, and improving all the possible issues regarding the output implementation as well as the detection sensitivity. By means of a numerical simulation, the research focused on investigating the mapping limits of the technique and relative potential for developement. Once processed in a synthetic environment, we applied the methodology to a physical - laboratory - application, in order to prove it relevant in association with the various monitoring methodologies. In the end, we obtained reliable outcomes, for what concerned the numerical study, while non consistent results in the physical application. The study assessed how the theory of Coda-Wave Interferometry has the potentiality to be a solid ally in the monitoring field, although its practical feasibility still requires further investigation.

Acknowledgements

In drafting this thesis, I cannot leave unnoticed the substantial help and sustain I have received over the last years.

First of all, I would particularly thank my three co-tutors: Dr. Yuguang Yang, for his incredible guidance I have had the honour to receive; Dr. Kees Weemstra, who has had both the patience to prepare me and the ability to enthuse me about the complex topics of this work; and Dr. Deyan Draganov, whose support has been essential for this thesis completion. I would like to express a particular appreciation to Prof. Rosario Ceravolo, who has given me the great opportunity of developing a project abroad while constantly sustaining me as main tutor, and to Prof. Cecilia Surace who has repeatedly encouraged me during these past years. I must also specify the great help I have received from Fengqiao Zhang who has adviced me since the very beginning of this work.

To my beloved ones, I would immediately express my gratitude to my mother, who has literally sustained me with her immeasurable love, and to my father who has been, and will always be, my mentor. Colgo l'occasione per ringraziare mia nonna Angela che ha sempre posto innanzi a qualsiasi cosa il mio benessere e la mia riuscita accademica, così come nonna Francesca e nonno Rodolfo.

Because no achievement is worth without friends, I would take the opportunity to especially thank Antonio, Giorgio and Giuseppe who have thought me that true friendship keeps on growing, even beyond the longest distance. Also to my roommate Lorenzo, who has been my adventure partner in these long five years, as well as Angelo, Tusco, Eugenio, Gabriele, Alessio, Francesco, Gianmarco, Luigi and all my dorm flatmates, with whom I have lived the greatest experiences in Turin. I thank also my exceptional team of colleagues: Elena, Giuseppe, Fabio, Riccardo, Paolo, Marta, and in particular Bartolomeo, who have been my anchor during this tough and extraordinary five years in the *Settentrione*. With them, I would like to thank for the immense backing Gianmarco, Adriano, Michele, Francisco and all the amazing people I have had the opportunity to share friendship with in Catania, Milan, Delft and Turin. Finally, to all my Civil Engineering course friends and my colleagues from the student associations.

Last but not least, and probably the most, I would express my gratitude to my beloved sister Daria Francesca, whose limitless support and encouragement were so strong they have solely driven my academic success. I entirely dedicate this thesis to her.

Contents

List of Figures

List of Tables

Summary

This study is based on a multidisciplinary work which finds its origins in the field of geophysics and gets adapted to an engineering area. For the success of this research, some basic background studies on wave-propagation and wave-distribution have been combined with the theories of structural and concrete engineering.

The thesis main ambition investigates whether or not the application of ultrasonic coda-waves can actually be an improvement in the already wide and developed Structural Health Monitoring environment and to quantify, up to what extent, such a procedure can recover stress variation in concrete. As discussed in the following paragraphs, a methodology capable to estimate and predict a possible load and damage alteration takes an essential role in the increasingly complex maintenance of civil structures. 'Maintenance' refers to both resilience assessment, at the end of the design life-time, as well as safety estimation and relative intervention, after the occurrence of an extreme event. The research questioned the description of the overall Coda-Wave Interferometry (referred in the thesis as **CWI**) in concrete, while concentrating on its strengths and weaknesses, drawing the starting line for further and detailed investigation. The work is structured to present and interpret the outputs, as they were obtained during the research, by carefully following the relative application procedure. In order to properly understand CWI prospects, a numerical analysis was performed. Such a simulation was based on applying a velocity change before the entire CWI procedure, in order to synthetically generate the perturbed medium; this gave the opportunity to compare the detected stress field with respect to the actually applied one. The laboratory development was structured in an analogous manner to the synthetic application, although the investigation was entirely unknown and no sensitivity check was possible.

To comprehend the detection system, it is crucial to describe the current infrastructural situation with relative problems, where the ultrasonic-wave propagation may provide useful information.

The initial - numerical - step was developed to investigate the theoretical reliability of such a methodology while setting up a series of simplistic assumptions, avoiding any possible drawback characterising a practical evaluation. An important amount of resources were directed to this simulation and to the derived parameters. After that, to reach a certain level of practical understanding, CWI was applied to laboratory data. It was also possible to properly calibrate a series of input factors related to concrete, impossible to assume otherwise; the thesis was structured to exhaustively examine the definition of these parameters, questioning their practical feasibility.

The aim of CWI lies in two main development areas: stress detection, investigated in the present research, and crack identification, which is only introduced in this thesis. The idea behind the application is based on providing the engineer with a sensible and correct analysis of the state of stress in structural elements. This way, it should be possible to immediately assess whether or not a specific component is suffering the load it was designed for and, at the same time, to properly quantify and locate any eventual anomaly of stress distribution within the system. A possible in-field application is described in the following chapter.

Although this research mainly focuses on concrete bridges and viaducts, the theory finds its applications in every field of beton structures. Furthermore, even if only purely concrete components were cited, CWI studies on steel-reinforced elements have been developed. Therefore, the reader shall not consider this as a methodology purely limited to infrastructural constructions, but with respect to wider and far reaching horizons. At the same time, monitoring of steel structures using analogous techniques is starting to catch on. However, being the focus on concrete already a quite challenging topic, steel systems were not treated in this work.

1

Introduction

1.1 Current European Infrastructural Situation

The Economic Miracle and the Birth of the European Network

The great European infrastructural network finds its origins right after the World War II period. Since 1946, every country in the old continent had dealt with a deep cultural, social and economical change. This period is identified by historians as the *Long Boom*, referring to the post World-War II economic expansion. Over these years, thanks to the U.S. aid (i.e. *Marshall plan*), the golden age of European industry (e.g. steel, iron, etc.) got triggered [91]. It kept on rising during the 60's until the 1973-1975 recession [53].

In this background, a parallel growth of infrastructure, both domestic and international, led to the great majority of what is presented today as the European Network [39].

1.1.1 Past Construction Methodologies and Present Problems

Clearly, over the past 70 years, the society has deeply mutated and, at the same time, a strong technological progress has occurred. Such great improvements have led all technical fields to change and evolve towards a more complete and reliable knowledge level.

Also the civil engineering has drastically changed throughout the past decades. From erection methods to building materials, the construction industry is now different from the recent past. In fact, the birth and spreading of calculators has brought the national and international building codes to require a much more complex as well as solid analysis of the design.

The past national codes were based on a limited knowledge, and relied on several simplistic theories, as a result of hand-calculation limits. Furthermore, in Europe, different countries had different ways of construction, so today, all bridges and viaducts have various allowed behaviours for specific stress and load configuration, and respect distinct safety concept. The modern codes, instead, are all based on a common base (i.e. the **EuroCodes**). These regulations rely on different probabilistic concept, defining various limit states to base the design on (e.g. *Ultimate Limit State*, ULS, and *Serviceability Limit State*, SLS). Now, the level of performance is much higher and the life duration, needed by the structure, is much longer than in the past, meanwhile, cost optimisation has become a fundamental requirement throughout the entire construction process.

Therefore, all the structures built during the above-mentioned period of growth are not able to fulfil the requirements stated by modern codes. It is further true that neither the resources nor the economic availability are present to demolish and rebuilt such a quantity of important network elements. This ends up in the present use of outdated structures which, according to the current basic design limitations, would be considered **not safe**. Civil-engineering societies have to deal with this sensitive problem by:

1. `Identifying` which infrastructure is not able to fulfil specific ULS and SLS requirements.
2. `Renovating` where needed, in an efficient way, to properly handle the problems and reach the modern specifications.
3. `Re-evaluate` the new design life span with respect to both ULS and SLS.

In the past years, signals regarding these problems have been sent by many infrastructures, globally. Due to the increased awareness about the issue, societies of engineers have started to draw paths towards maintenance directions. On this matter, the most recent event relates to the *Viadotto Polcevera* (a.k.a. Morandi bridge), an important infrastructure in Italy, which collapsed in August 2018. Other than causing the death of 43 people, this tragedy highlighted the substantial logistical damages to which the subjected metropolitan area can suffer. This event, in addition to several previous ones, underlines the seriousness of the problem and the urgency for a proper and efficient methodology of damage control and prevention.

1.1.2 The Administrative Effort

Among the several governmental activities, it is worth mentioning the European Union actions to tackle the progressive damaging of existing structures. Since November 2017, the European Commission has set a focus on the previous *Europe on the Move* initiative, with the main goal to reach a concrete reality in the mobility sector all over the continent [65]. With respect to the past, a new push towards safety, related to the anti-terrorism protection system, has been developed (CIPS). It consists of a much wider program which takes into account the logistic role of the European network as '*a sensitive asset to be protected against any possible threat*' [65]. This directive takes the name of *European Program for Critical Infrastructure Protection* (EPCIP). It consists of [19]:

1. `Identifying` and `designating` critical European infrastructures, and `planning` a common intervention line.
2. `Direct measures` to facilitate EPCIP to have a prepared `action plan` as well as a network of continental warning systems.
3. `Emergency directives` and relative `scenarios`.
4. `Financial management plan`.

It is alongside these directives that the EU, as every other country, is trying to properly handle and reduce, as much as possible, any potential threat triggered by a structural failure.

1.2 The Role of Structural Health Monitoring

With this premises, it is now fundamental to dwell on the scientific area charged with handling the aforesaid issue: the Structural Health Monitoring (**SHM**). Nowadays, SHM intends to characterise and detect damages on every level of the system. This sensing field of engineering has been widely used in other technical areas, such as aerospace engineering. However, the stationary building sector has only witnessed a relatively recent exploit with respect to the more general **resilience study**.

Over the past 20 years, SHM has quickly gained relevance in the most recent civil construction environment. From the classic, still mainstream, visual investigation to increasingly more evolved and structured Non-Destructive Tests (NDTs), the latest background for engineering societies is deeply linked with structural control. Moreover, the above highlighted reasons make the infrastructure inspection play an essential role in logistic and public safety over the next decades.

1.2.1 Approach

SHM currently takes into consideration various specific fields of intervention. Their descriptions are essentially derived from the definition and interpretation of damage. As discussed in "*A Review of Structural Health Monitoring in literature 1996-2001*" by Sohn et al., damage can "*alter the stiffness, mass, or energy dissipation properties of a system, which in turn alter the measured dynamic response of the system*" [84]. This gets usually stated in terms of length scale (e.g. from material level to component/system level) as well as temporal ones (e.g. corrosion/fatigue for long-term or earthquake as momentary study).

Basically, referring to monitoring processes implicates the system analysis. This way, it is possible to perform a structural-health assessment by means of a sensors cluster, which is composed by all system characteristics [87]. Farrar and Doebling addressed it as "*statistical pattern recognition paradigm*" in "*Damage Detection and Evaluation II*" [29]. It gets described as:

1. `Operational Evaluation`
2. `Data Acquisition, Fusion and Cleansing`
3. `Feature Extraction`
4. `Statistical Model Development`

The first point assesses the practical feasibility of the monitoring as well as its safety-economic evaluations. It also has the central role of identifying, on which level of time and length scale, the system needs to be investigated.

Secondly, the determination of specific characteristics, with related positioning and selection of receivers, takes place. Also the periodicity of data collection (e.g. continuously or discretely at time intervals) plays an important role. Moreover, *data fusion* becomes essential in the analysis of more complete and difficult structures [86]. This is usually followed by *data cleansing* which drives the set of information to filter, increasing its reliability. Such a process has resulted in several studies focused on the application of machine learning [7] [30] [16].

Successively, damage identification occurs by means of specific sensitive characteristics of the system. Clearly, analysis of these features can result in quite different properties of the structure. The bottom line consists in defining the appropriate combination and fusion of such features in order to obtain a redundant and coherent assessment. This is the range of SHM which allows a wide variety of approaches; several are the properties as well as the methodologies available for the damage identification step.

The final SHM phase, regarding the improvement of damage detection, investigates the statistical significance, which results in the most essential and noteworthy part when developing a monitoring technique. The statistical models, using structural dynamics techniques and analytical designs, have the role of assessing the following five points of damage [84] highlighted by Rytter [56]:

- `Existence`
- `Location`
- `Type`
- `Extent`
- `Remaining life`

Determining these points covers a relevant step also for CWI applications. While the `existence`, the `location`, and the `type` of damage would be directly issued in this research, its `extent` definition was examined as well, but without any useful results. The delicate point focuses on the system `remaining life`: in order to address this topic, the CWI methodology would require a solid implementation grown over some years of application. Stating the remaining life is an indirect process, largely driven by the engineer interpretation, which takes into account all the previous four points in combination with the general history of the structure.

For bridges and viaducts, several monitoring characteristics are placed under investigation in order to preserve these structures and increase their resilience: e.g. wind and weather, traffic, cables and pylons study. In the present study, the main ambition consisted of the analysis of structural elements, to achieve a proper stress-state extraction and, by means of that, estimate the load distribution according to the original design.

However, the designer is able to use monitoring techniques to reach other levels of evaluation, such as fatigue and remaining life-span [87].

In the end, it is not possible to state *a-priori* which is the most correct type of monitoring approach to be followed. This is related to: type of operational monitoring; Sensor nature; Sensor amount; Transmission of data and Energy received [51]. In the literature, a notable amount of examples is found for various types and conditions of damage, regarding infrastructures all over the world [88] [105] [38] [74].

1.2.2 Techniques

Nowadays, several structural-health monitoring techniques have been developed and have found utilisation in the building sector. Among them, notable are: *strain gauges*, *fibre optic strain*, *piezoelectric sensors*, *micro-electric sensors* [30], as well as *computed tomography* [81], and *capacitance-based strain sensors* [40]. These techniques are considered as the most reliable and noteworthy to be introduced and are often presented in the literature [92] [23] [20] [75] [45].

The available techniques get usually divided into Passive and Active sensing methodologies [76]. The main difference concerns the fact that Active sensing regards a monitoring technique, which induces some energy to the system, using a controlled source, while Passive sensing does not [22]. As an example, the SHM system investigated in the present work (Coda-Wave Interferometry) falls under the Active sensing because depending on active sources.

Another sensing approach distinction is based on wired and wireless setting. Where the latter setting, although coming with a higher cost, has the potentiality to develop a complete and more coherent monitoring. Wired sensors, instead, have the ability to exploit absolute positional analysis and to be applicable to various materials. However, this requires specific conditions of applicability when employing the particular monitoring methodology to various situations, each regarding an investigation of structural reliability to specific adverse conditions [21].

The SHM system investigated in the current work is a wired active-source methodology which exploits ultrasonic scattered waves in order to map the stress distribution inside a medium [102] [27].

1.3 CWI In-Field Application

Because monitoring of bridges has ben the central idea in the use of discussed Coda-Wave Interferometry theory, a possible practical application is here briefly hypothesised. Such a technique is developed by employing source-receiver sensors, defined in the next chapters as *Smart Aggregates*. The proper in-field study for bridges and viaducts requires to follow a specialised path, which can only be standardised up to a certain level. This sensing method is deeply related to the studied system, whose characteristics need to be specifically stated. Thus, it is complex to properly assess the uniqueness of the system, implemented in an intuitive computation, while giving a clear, and still reliable, CWI outcome.

The first step for an in-field application is the physical application of the sensors to the structural element to investigate (e.g. piers, cross-beams, etc.); the more accurate their utilisation, the more correct the stress detection can get. If not properly handled, it would present several issues concerning the logistical placing of the sensors in huge structures. To implement the technique, the focus must be placed on identifying which system element can be studied and which can be left out of the investigation. Statistical studies [31] have proven to precisely detect the safety level by monitoring just a few number of elements, which compose the system. This step underlines the challenging optimisation road for CWI, which becomes essential for applications in the field.

Consequently, a CWI study, continuous or intermittent, shall be performed. By emitting, detecting, and properly interpreting ultrasonic-waves, the coda-wave information of the element can be extracted. As the CWI is referred to the comparison between modified and unperturbed signals (see chapter 2), the definition of a perturbed signal will eventually come some time after the application of the sensors and the relative detection of the reference signal. This may state a limitation for existing bridges, especially after extreme events, where an immediate structural-health assessment is needed. Nevertheless, during the structural design, the expected stress distribution is already known, therefore, an alternative path may focus on the signal simulation from an identical numerical bridge: the synthetic signal would represent the reference to be compared with the actual signal, which now would provide the modified features. This application, although some potentiality, presents several challenges (e.g. does not take into account construction errors), thus it requires further investigation.

At the moment, obtaining data can be achieved by practically going in the field and plugging-in the wired technology to a portable calculator, every time a specific structure requires an evaluation; then, the software processes all the calculations, providing the results. Another possible data gaining and processing could be developed by a wireless communication system between the sensors and a data centre. This would result in a more effective monitoring methodology at the cost of additional specifications. In fact, every infrastructural department, by means of a unique connected base, would have the capability of constantly assessing the safety level of the entire transport network, at a minimum labour expense. If efficiently combined with *in-situ* skilled teams, such a CWI in-field application could trigger an immediate response by coordinating correct maintenance intervention, driving the health-assessment to a comprehensive analysis.

2

Coda-Wave Interferometry

The present research focuses on the limits and possibilities of CWI. This technique might result in a turning point in the monitoring of buildings, bridges, and viaducts. It enables the description of the the state of stress in a structural element. A consequence of this would be the identification of any possible variation in the expected stress distribution, allowing the proper comprehension of the structural behaviour (e.g. of a pillar, a beam, a bearing wall).

CWI originated in the field of geophysics: the interpretation of the late part of the wave is used to map changes in the earth. The seismic Interferometry methodology, in fact, involves the cross-correlation of seismic observations derived from sensors at various locations [25]. A series of sources are usually placed on the surface and their waves are collected by the receivers, after having scattered through the subsurface[1].

In order to explore this theory, it is noteworthy to mention an analogous and older monitoring technique: the Time of Flight (**ToF**).

---

[1] By means of this process, in fact, it is possible to identify the different layers composing the earth [97] [64] [78] [70].

Time of Flight

This monitoring method considers the arrival instant of a wave that propagated from the source to the receiver. By means of the simple rule $velocity = \frac{distance}{time}$, it establishes a time standard to extract the wave velocity of the medium [14]. As a result, it is possible to interpret such an output in order to investigate and verify the reasons behind a possible decreasing or increasing of the propagating wave velocity. This technique is quite straightforward; however, it shows a series of uncertainties and limits [28]. Its main application, in fact, does not allow to extract information from the surrounding area. Moreover, in a strongly heterogeneous medium, this technique cannot be applied. This is because, if there is too much scattering, there simply is no direct wave that can be observed. That is, the first arrival will, in this case, have scattered multiple times prior the arrival at the receiver. Furthermore, it is not able to distinguish any potential localised variations and the only possibility to have a consistent result relies on providing continuity over its application, both time and space wisely, which generates strong restrictions in practice. CWI can overcome these limits.

2.1 Acoustoelastic Effect

Before introducing the CWI, the following acoustoelastic effect needs to be specified. Once the overall velocity variation map has been extracted by means of CWI, it is essential to understand whether or not, and how, the obtained information gets related to the stress field, which, from an application point of view, is the final objective.

Considering the main assumption of concrete as an elastic material allows to exploit a series of properties. With respect to the classical linear elasticity theory, the velocity is assumed to change when the concrete is subjected to states of stress. The very basic relationship, regarding *small deformations*, introduces the generalised Hook's law [99]. The plain stress conditions make the Hook's law as follow:

$$\begin{bmatrix} \sigma_{11} \\ \sigma_{22} \\ \sigma_{12} \end{bmatrix} = \frac{E}{1-\nu} \begin{bmatrix} 1 & \nu & 0 \\ \nu & 1 & 0 \\ 0 & 0 & \frac{1-\nu}{2} \end{bmatrix} \begin{bmatrix} \epsilon_{11} \\ \epsilon_{22} \\ \epsilon_{12} \end{bmatrix} \tag{2.1}$$

From this, Murnaghan extended the linear elastic theory to *finite deformations* [57] and, later, Hughes and Kelly extracted numerical values for different elastic constants, under uniaxial compression and hydrostatic pressure [2].

The main goal of the research is based on investigating how the CWI monitoring technique is able to assess the changes in the stress-state. Nevertheless, as derived in the following section, the methodology allows to only extract the variation of velocity. Therefore, we assumed the *acoustoelastic effect* as the backbone observation of the entire study, to definitively relate velocity state to the state of stress, which is the starting point of the overall structural assessment.

2.2 Theoretical Fundamentals

Starting from the very same basics of the ToF methodology and relying on the above-mentioned acoustoelastic notion, CWI can undertake much more complex and wider structural analyses. However, its theoretical background gets more complex than its older analogous technique.

2.2.1 Wave Propagation and Scattering in Concrete

The main information is extracted from the waves propagating through the medium [78]. Assuming that the waves experienced a certain amount of scatterings through the medium, its **coda** part will be characterised by a specific *signature* of this setting. This characteristic can be related to a delay of the wave consisting in a faster or slower signal, i.e. shorter or longer in the time domain.

Basically, the theory takes into consideration the *first Fresnel Zone* ($F_1 = \frac{1}{2}\sqrt{\frac{cD}{f}}$), which describes the "*ellipsoidal regions of clearance regarding wave propagation*" [33]. In the previous relation: c is the speed of light in the air, f is the frequency of the signal, and D is the distance between the transmitter and the receiver. Different wave frequencies have different regimes of scattering and attenuation (figure 2.2). Planès and Larose (2012) [70] propose several ranges in heterogeneous media; such values are here listed in ascending order of the frequency band of influence: *Modal analysis*; *Simple scattering*; *Multi scattering*; and *Strong Absorption*.

A higher frequency results in a higher sensitivity to the medium change because the relation $f = \frac{v}{\lambda}$ underlines that a higher frequency leads to shorter wavelength, thus, smaller heterogeneities can be detected; e.g. with a wave velocity of $\approx 4000 m/s$, a central frequency of $4 MHz$ would be characterised by a wavelength sensitivity of $1 mm$. However, raising the frequency causes some energy absorption. In the end, the chosen central frequency of $88 kHz$ was a balance between these boundaries, which makes the

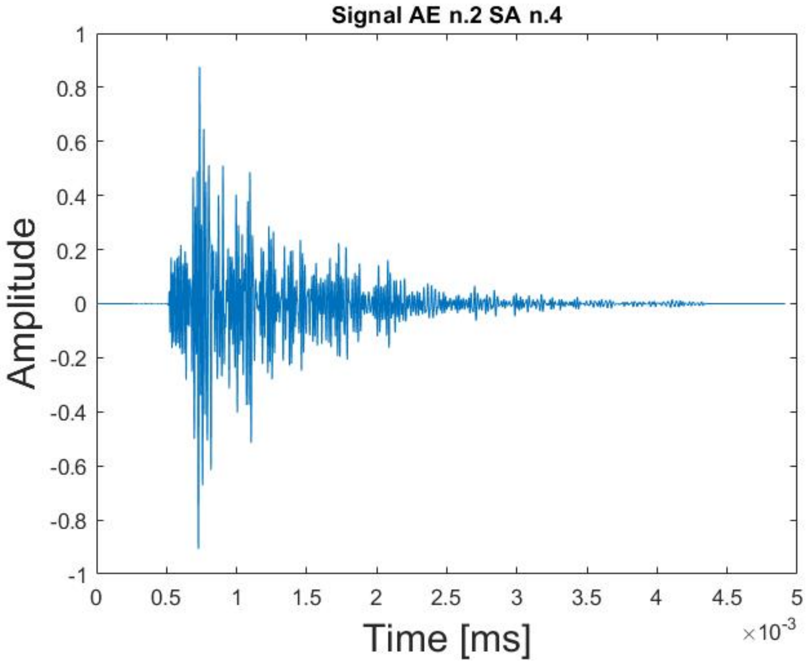

Figure 2.1: An example signal shape of wave propagating through concrete. This graph has been extracted from the laboratory data set, with respect to configuration Smart Aggregate n.4 - Acoustic Emitter n.2. The first arrivals appear at $t \approx 600\mu s$ and, from $t \approx 1200\mu s$, the exponential decay related to the scattering of the **coda** occurs. Shape characteristic regarding the imposed settings; different form if the medium would have been homogeneous or without boundaries.

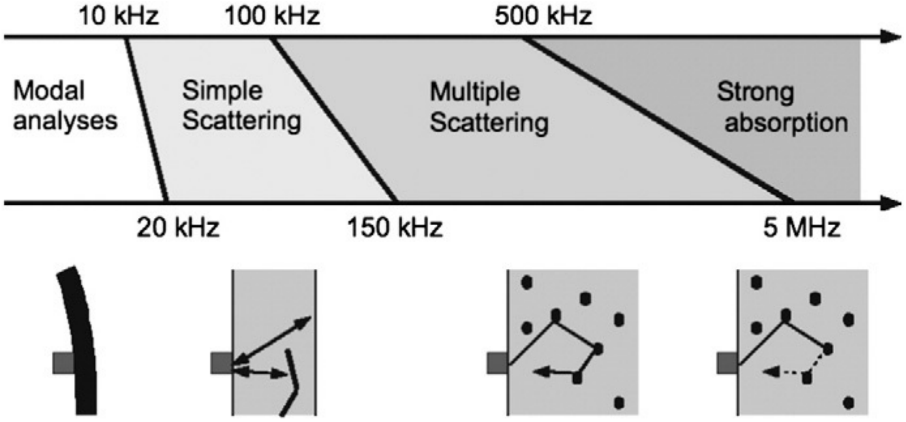

Figure 2.2: Four different scattering regimes and respective frequency boundaries. Only valid for a specific medium like concrete; for a homogeneous medium, this will not be the case [70].

wave attenuation fall in a *Multi-scattering regime*. This introduced a scattering sensitivity equal to $\approx 4.545cm$ (discussed in chapters 3 and 4). Due to the chosen frequency, this application can be considered as a *ultrasonic testing technique* [59].

2.2.2 The Diffusivity Question

Dwelling on the diffusion of wave through a medium is essential for the wave propagation and scattering determination in the research. The diffusion parameter allows to give a quantifiable magnitude of the scattering, the wave goes through. Such a value, usually referred to as D, reflects one of the very basic properties of the material under analysis. The D parameter refers to the wave capability of diffusing through a medium. Thus, (contrary to what may seem) while the diffusion decreases, the scattering inside the medium increases. Although several papers mentioned a series of values [104] [49] [78], over the present work, an extensive analysis was carried out in order to get a consistent and unique D value.

Moreover, due to the diffusivity definition, its identification carries a parallel investigation of the Von Karman numerical simulation of concrete (discussed in the following chapter). In fact, because the determination of the diffusion attribute is strongly linked to the nature of the medium itself, it necessarily leads to a connection between this value and the Von Karman input parameters (i.e. correlation distance and fractional velocity fluctuation).

The Time-Dependent Boltzmann equation

"*The spreading of particles, heat or radiations is one of the most universal topics in science*" [66]. The correct definition of an equation able to properly describe how waves propagate through random media has been investigated several years ago.

As described by Paasschens (1997) [66], the Boltzmann equation is a good definition of probability density which is a function of time and position of the source. Although a general analytical 3D form does not exist, an analytical 2D solution does [66] [64] (i.e. *radiative transfer equation*):

$$P(r,t) = \frac{e^{-ct/l}}{2\pi r}\delta(ct-r) + \frac{1}{2\pi lct}\left(1-\frac{r^2}{c^2t^2}\right)^{-\frac{1}{2}} e^{l^{-1}(\sqrt{c^2t^2-r^2}-ct)}\Theta(ct-r)\,, \tag{2.2}$$

$P(r,t)$ refers to the **Intensity** of the wave, averaged for every trajectory, propagating through the medium at a distance r and time t; l is the transport mean free path, c refers to the speed of the wave, Θ is the step-function, and r presents the source-receiver distance. Generally, the equation shows P values equal to zero for $r > ct$ and a correct estimation at short times (i.e. $t < l/c$).

Diffusion equation

Due to the formulation complexity, the solution to the Boltzmann equation gets usually approximated in its long-time limit (i.e. $t >> r/c$) by the solution to the *Diffusion equation* [66]

$$P(\boldsymbol{r}, t) = \frac{1}{(4\pi D t)^{d/2}} e^{-\frac{r^2}{4Dt} - \frac{t}{\tau}} \,. \tag{2.3}$$

where $P(\boldsymbol{r}, t)$ refers to the averaged **Intensity** of the wave, propagating through the medium at a distance $\boldsymbol{r}$ and time t, and the d parameter indicates the dimension for which the solution is valid (i.e. $d = 2$ in this bi-dimensional study). The main difference from the previous formula (2.2) lies in the simple presence of two factors, D and τ, which define the essential characteristics of the medium under study (extensively discussed in the following sections). D is the diffusivity parameter, and τ refers to the absorption time which describes the quantity of internal dissipation of the element. Due to the randomised theoretical base, sometimes in literature this equation gets referred to as *probability density.*

The choice between the *diffusion equation* 2.3 and the more complex, and more correct, *radiative transfer equation* 2.2 generates some difference in the sensitivity kernel (represented in Figures 2.7 and 2.8).

2.2.3 Stretching Method

When a wave gets modified, due to a local variation, its shape and amplitude can be altered with respect to the original. As numerically and physically extracted in the next chapters, the magnitude of variation of wave velocity leads to a simple slowing or speeding in the signal. In fact, it tends to keep its original shape with a slight deformation in the horizontal time axis [97] [78] (Figure 2.3).

The time axis, of the perturbed signal, needs to be *stretched* (or *compressed*) for a specific amount in order to compare the different signals. The new time axis, referred to as t', is expressed by $t' = t + \Delta t$, where t defines the instants of the unperturbed signal and Δt is the stretching amount. As mathematically derived, the delicate CWI step consists of relating this time variation to a change in the apparent velocity field: *apparent relative velocity variation* ϵ.

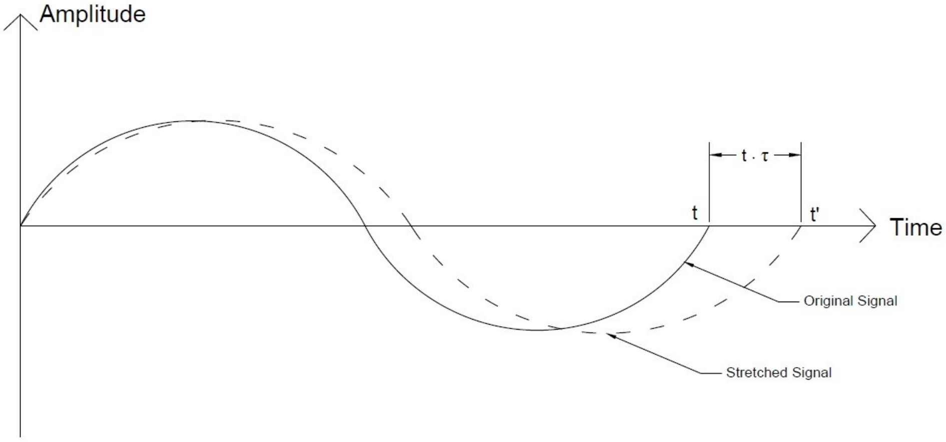

Figure 2.3: Theoretical representation of the stretching technique [43]. In this figure, τ coincides with $\frac{\Delta t}{t} \equiv \epsilon$.

The new time axis for the perturbed-stretched signal is identified as

$$t' = t + \Delta t\,, \tag{2.4}$$

where Δt is nothing but the time amount, both positive or negative, required by the perturbed signal to be shifted towards the unperturbed one:

$$t' = t\left(1 + \frac{\Delta t}{t}\right) = t(1+\epsilon) \tag{2.5}$$

For what concerns the velocity, it will experience a change (speeding or slowing) described by:

$$v' = v + \Delta v = v\left(1 + \frac{\Delta v}{v}\right)\,, \tag{2.6}$$

knowing that the velocity inside the non-modified medium follows the rule

$$v = \frac{l}{t} \tag{2.7}$$

where l is the distance crossed in a time t. Inside the perturbed medium, instead, the same distance l will now be crossed in a different time (i.e. *stretched* or *compressed*), resulting in a new velocity value:

$$v' = \frac{l}{t + \Delta t} \tag{2.8}$$

$$v' = \frac{\frac{l}{t}}{1 + \epsilon} \tag{2.9}$$

$$v' = \frac{v}{1 + \epsilon} \tag{2.10}$$

Finally, the velocity variation results in:

$$v = v'(1 + \epsilon) \tag{2.11}$$

From equation 2.6 the non perturbed velocity can be written as

$$v = v' - \Delta v = v' \left(1 - \frac{\Delta v}{v'}\right) \tag{2.12}$$

In the end, considering the equivalence between equation 2.11 and 2.12, the following relationship is found:

$$\frac{\Delta t}{t} \equiv \epsilon = -\frac{\Delta v}{v'} = -\frac{\Delta v}{v + \Delta v} \approx -\frac{\Delta v}{v} \tag{2.13}$$

The $-$ sign depends on the chosen convention; i.e. whether or not stretching is under consideration rather than compression. The approximation of equation 2.13 is obtained from the assumption that $v >> \Delta v$.

Another useful value, obtained in the stretching section, is the Correlation Coefficient. The relation between the apparent relative velocity variation and the cross-correlation coefficient present a change of the correlation factor between the unperturbed and the perturbed signal. Among the several ϵ values tested, the one, which maximised this factor, defined the specific change of apparent velocity.

What is usually done, in the classic SHM process, is to apply such stretching technique between the loaded and unloaded data, and to extract the $\frac{dv}{v}$ in the source-receiver line. In a second moment this gets interpolated with the Kernel, where it becomes possible to see whether some areas have undergone change in their velocity field, and thus a change in their stress distribution.

2.2.4 Velocity Variation

As mentioned, the stretching parameter ϵ becomes of fundamental importance for the overall study and, in order to extract it, a series of specification needs to be taken into consideration.
First of all, the timing window of analysis was discussed as well as the relationship between the stretched parameter ϵ and the already introduced *Correlation Coefficient*.

Between the perturbed and unperturbed forms of the signal, it was possible to observe that the wave propagation signals revealed an almost similar behaviour; the main difference lied on the *time-lag*. Figures 2.4 below represent the stretching development of the area setting of the first configuration in the numerical study: a velocity variation of $\Delta v = -150 m/s$ within an area of $500 mm^2$.

In the plots, shown in Figure 2.4, a zoom on the specific window of the sensor pair Acoustic Emitter 1 - Smart Aggregate 1 (generally indicated in the thesis as AE1-SA1) is highlighted, where the perturbed signal, if properly *stretched* forward, can be partly overlapped to the unperturbed one.

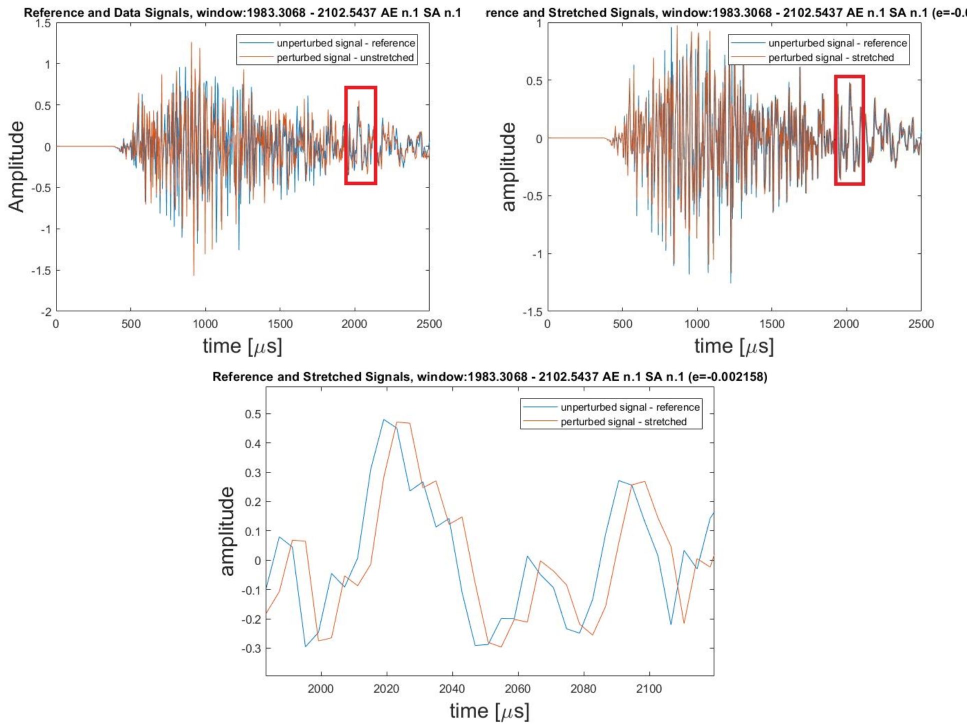
Reference and Data Signals, window:1983.3068 - 2102.5437 AE n.1 SA n.1

rence and Stretched Signals, window:1983.3068 - 2102.5437 AE n.1 SA n.1 (e=-0.

Reference and Stretched Signals, window:1983.3068 - 2102.5437 AE n.1 SA n.1 (e=-0.002158)

Figure 2.4: Perturbed and unperturbed signals, both stretched (right) and non-stretched (left). Highlighted in red the window of study (top figures) and zoomed image (bottom). Time window: $\Delta t = 1983\mu s$ - $2102\mu s$.

Time Window

An essential detail about the stretching - compressing step is the time windowing. The cross-correlation technique is time-windowed and its measuring gets a substantial role in identifying the velocity variation with respect to the width and the position of such framework.

The analysis of a wider segment would give higher reliability to the process helping to minimise the perturbations of the values from the mean one. On the other hand, a too expanded investigation may lead to a loss of accuracy in including all data. Pacheco and Snieder, in *Time-lapse travel time change of multiply scattered acoustic waves* [67], showed that, as the window length increases, the magnitude of the cross terms on the averaged intensity decreases, leading to a drop of the fluctuations of time-lag, while cross-correlating the perturbed signal with the unperturbed one. Furthermore, a too short window might result in extracting a non consistent output disturbing the stability of the estimation [70].

Another sensible decision to be taken consisted on the central position of the time frame. As previously mentioned, the location of the midpoint in the window, within the time axis, strongly affects the outcome of the entire procedure, therefore, the apparent relative velocity variation and the Correlation Coefficient are severally biased by it. In addition, a time window too close to the first arrivals might generate a severe influence in the test. This is due to the ballistic waves that are not able to detect any change outside the direct connection line between starting and ending points.

Correlation Coefficient

The correlation coefficient is a statistical measure, varying between $+1$ and -1, that calculates the strength of the relationship between two variables (e.g. signals). Negative values represent anti-correlation which is what we are not interested in. A positive factor, tending to $+1$, would state a complete correlation between the two signals, i.e. the reference and the stretched one. Usually, values lower than ≈ 0.80 / ≈ 0.70 are not considered. Hence, throughout the research, the aim to investigate ϵ which correlated the perturbed and unperturbed signals, being characterised by CC values higher than that threshold [34]. The CC is mathematically expressed as [97] [18]

$$CC(\epsilon) = \frac{\int_{t_1}^{t_2} \phi'[t(1-\epsilon)]\phi[t]\,dt}{\int_{t_1}^{t_2} \phi'^2[t(1-\epsilon)]\,dt \int_{t_1}^{t_2} \phi^2[t]\,dt}, \tag{2.14}$$

where t_1 denotes the starting time of the window while t_2 its end. Among the several ϵ values, the one which best stretches the perturbed signal with respect to the unperturbed one (i.e. in accordance with $t(1-\epsilon)$) results in the one ϵ which maximises the correlation coefficient.

Figure 2.5 shows the correlation coefficient with respect to each time segment and each source-receiver pair as a function of ϵ; the obtained curve is in accordance to the ones presented in the literature [43].

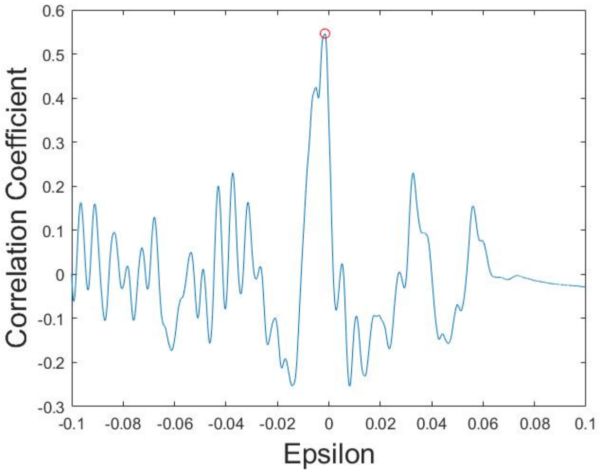

Figure 2.5: Relation between CC and ϵ for configuration Acoustic Emitter n.13 - Smart Aggregate n.3. The window under analysis is: $1983\mu s - 2380\mu s$.

In the literature [103] [80], the CC is used quite often as main element in the inversion procedure to conduct a parallel analysis with different aims: the Coda Wave Decorrelation (**CWD**). In fact, by means of the Decorrelation Coefficient ($DC = 1 - CC$) it is possible to detect possible cracks inside the medium. While the stretching factor is related to the variation of velocity, this approach aims at obtaining, by means of the DC, the *density of change in the effective scattering cross-section.* Such value, usually presented as $\sigma(x)$, can be associated with a change (e.g. macro/micro craks formation) in the medium under study, and, thus, it highlights existing cracks or various openings inside the element under investigation.

2.2.5 Sensitivity Kernel

Up to this point, the process appeared to be exactly the same as the classic Time of Flight analysis, with the only difference concerning the studied part of the signal (i.e.

coda rather than ballistic). After that, the analysis needs to be expanded further in order to gain the most from the late arrivals and their characterisation of the medium. In fact, a statistical approach is later developed around the connection line between the source and the receiver. By meand of to the Sensitivity Kernel, it is possible to re-elaborate the observed data, from the stretching step, in order to obtain reliable information about the surrounding area of the connecting line.

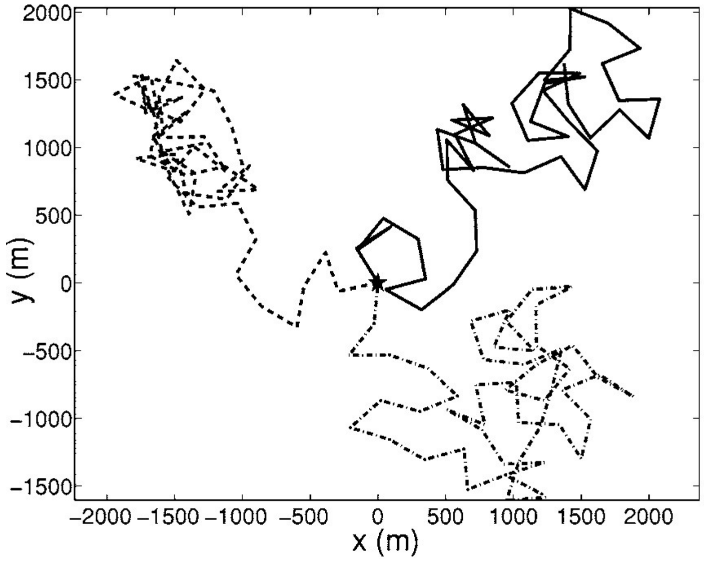

Figure 2.6: Graphical representation of the possible "random walks" of waves travelling through the medium [67].

Conceptually, the Kernel is nothing but the statistical probability that, in a specific time interval $(t' - t)$, the wave, starting from source $\mathbf{S}$ and arriving at receiver $\mathbf{R}$, passes through a generic point $\boldsymbol{x}$ within the medium. Apparently, this probability will increase as the generic point $\mathbf{x}$ gets closer to either the source or receiver. Furthermore, as t' grows, the probability of the wave scattering through a point at a longer distance from the departure-arrival line increases as well. On the other hand, the shorter the time interval, the lower the values of the kernel for $\boldsymbol{x}$ outside of the connecting line; because of the diminished probability of scattering far away from the introduced direction, during such a short period. Therefore, the Kernel is considered reliable inside the ellipse with the source and receiver as foci, and non-reliable outside.

Once knowing the signal shape, trying to extract the relationship of an energy impulse at time t with respect to a specific path might result in a complex operation. However, if the contributions of all possible trajectories, at the receiver at time t, are summed and, from it, the average wave field is extracted, the problem becomes simplified [67]. The statistical base of the above-mentioned simplification relies on the notion of *Brownian motion* [42].

It is thanks to the several possible paths the wave can scatter through (figure 2.6), that the simple stretching technique gets exploited into the more complete and general CWI. The wave-propagation process, indeed, can be approximated as a random-walk process (figure 2.6); thus, it can be successfully characterised by the diffusion equation. For this reason, the diffusively scattered wave field is obtained as a series of partial waves travelling towards different trajectories.

Radiative Transfer or Diffusion Approximation

The Sensitivity Kernel, applied in the following numerical and laboratory test, does not reflect the most correct definition but rather an approximation. It is function of the Intensity propagation probability, which is based on the diffusion approximation (equation 2.3). It results in a proper and correct analysis only when the velocity variations are distant from the source-receiver pair and the time instants to be considered are much later than the transport mean free time, i.e. when $t >> t^* = \frac{l^*}{c}$, where l^* is the transport mean free distance (see section 3.3.2) and c the velocity of wave propagation.

For the sake of completeness, also the Radiative Transfer definition of the Kernel gets briefly analysed. The just mentioned description, indeed, defines a more complete evaluation of the scattering in random media, which is reflected by the Intensity probability with respect to the Boltzmann solution (equation 2.2). It provides a better and more precise Kernel description than the diffusion definition, as it is possible to see from the surface plots in Figures 2.7 and 2.8.

Although the latter formulation includes more reliable and correct definition of the sensitivity kernel, as well as a smoother [66] and continuous curve, for the present study, the diffusion approximation resulted in a decent estimation - especially with respect to the study set up. Moreover, the inversion procedure, later presented, led to an equivalent output for the two different approaches.

In a mathematical definition, the Sensitivity Kernel is highly connected to the definition of intensity. In fact, similarly to the latter, also the Kernel is dependent on the boundaries and, thus, it requires the approximation of the reflected source with respect to the perfectly reflecting edges. It is defined by the convolution of the intensity as a function of time u at the numerator divided by wave intensity

$$K(\boldsymbol{S}, \boldsymbol{R}, \boldsymbol{r_0}, t) = \frac{\int_0^t P(\boldsymbol{S}, \boldsymbol{r_0}, u) P(\boldsymbol{r_0}, \boldsymbol{R}, t-u)\, du)}{P(\boldsymbol{S}, \boldsymbol{R}, t)}, \tag{2.15}$$

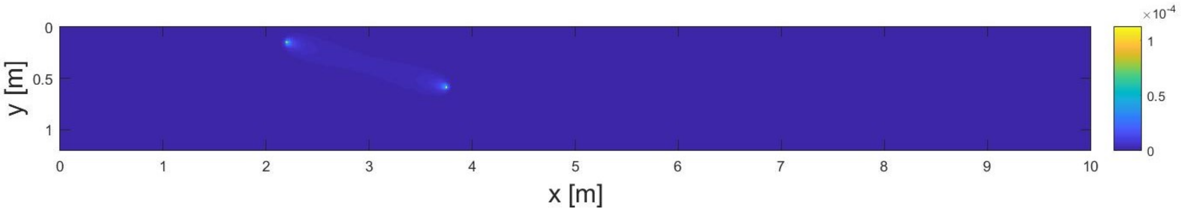

(a) Diffusive definition

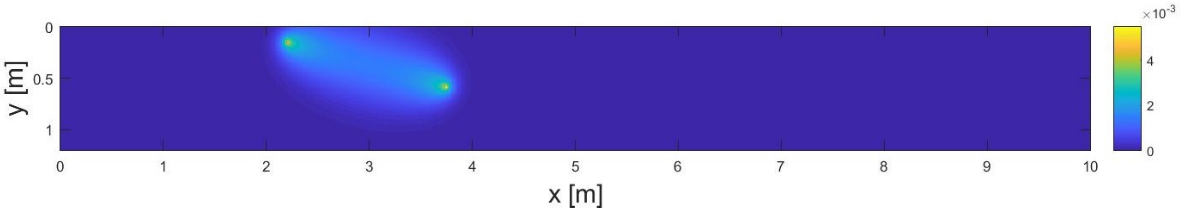

(b) Radiative transfer definition

Figure 2.7: Surface representation of the sensitivity kernel for configuration Acoustic Emitter n.5 - Smart Aggregate n.5. Central time of evaluation is $t = 1667\mu s$.

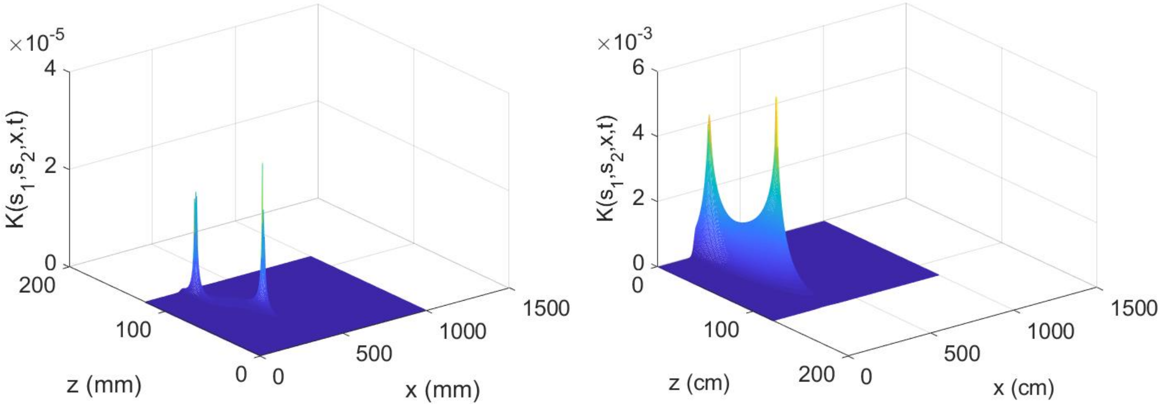

Figure 2.8: Mesh representation of the sensitivity kernel for Acoustic Emitter n.5 - Smart Aggregate n.5 pair. Left image refers to the diffusive definition while the right image to the radiative transfer solution. Central time of evaluation is $t = 1667\mu s$.

where $\mathbf{S}$ is the position of the Source and $\mathbf{R}$ is the Receiver location, t is the centre of time window, highlighted in the stretching step, and $\boldsymbol{r_0}$ is the position of the local velocity variation. The value $P(\boldsymbol{a}, \boldsymbol{b}, t)$, which reflects the *probability* of a wave travelling from $\mathbf{a}$ to $\mathbf{b}$ over a time t, must not be confused with I (sometimes indicated as ϕ^2), which, instead, represents the specific intensity for every trajectory. Thus, they are related as

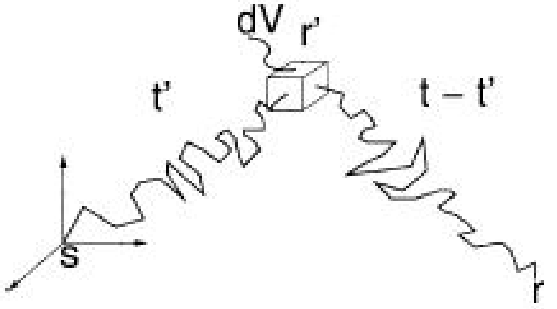

Figure 2.9: Graphical description of point moving from $\boldsymbol{s}$ to $\boldsymbol{r'}$ and from $\boldsymbol{r'}$ to $\boldsymbol{r}$ [67].

$P(\boldsymbol{r}, t) \equiv \langle I \rangle$, where $\langle I \rangle$ represents the envelope of all Intensities.

Mathematical Derivation

Starting from the basic concept of a random-walk process [42], the product of the diffusive intensity $P(\boldsymbol{r}, t)$ with an infinitesimal volume element dV at position $\mathbf{r}$, represents the probability of the path passing through that element. In an energy perspective, the overall value within volume V is:

$$W(V,t) = \int_V P(\boldsymbol{r}, t)\, dV(\boldsymbol{r}) \tag{2.16}$$

The normalised energy, if the volume V under consideration is the entire element, would result in being $W(t) = 1$. Increasing the detailing of the derivation[2], it is possible to identify the probability that the random walk starts at point $\mathbf{s}$ at $t = 0$ and ends at point $\mathbf{r}$ over the interval t, passing through point x at time instant $t' < t$. The mathematical definition comes from the simple product between the probability of all the trajectories starting from point $\mathbf{s}$ reaching $\boldsymbol{r'}$ in time t' and the probability of all trajectories starting from $\boldsymbol{r'}$ to point $\mathbf{r}$ in time $t - t'$ (see also figure 2.9):

$$P(\boldsymbol{r'}, \mathbf{r}, \mathbf{s}, t', t) = P(\boldsymbol{r'}, \mathbf{s}, t')P(\mathbf{r}, \boldsymbol{r'}, t - t') \tag{2.17}$$

The above definition comes from the total independence between the two probabilities. $P(\boldsymbol{r'}, \boldsymbol{s}, t')$ can be considered also as the diffuse intensity at time t' at $\boldsymbol{r'}$ due to an impulse

---

[2] Matematical derivation entirely depicted in accordance to Pacheco et al. [67]

at $\boldsymbol{s}$ initiated at $t = 0$. The same concept for $P(\boldsymbol{r}, \boldsymbol{r'}, t - t')$ which is the intensity at time t, at location $\boldsymbol{r}$, for a given impulse at $\boldsymbol{r'}$, at the instant $t - t'$.

The following step consists in summing the contributions to the intensity of all waves through any random walk between source and receiver, which results in having the previous equation integrated over all possible spatial elements: the *Chapman-Kolmogorov* equation is [77].

$$P(\mathbf{r}, \mathbf{s}, t) = \int_V P(\boldsymbol{r'}, \mathbf{r}, \mathbf{s}, t', t)\, dV(\boldsymbol{r'}) = \int_V P(\boldsymbol{r'}, \mathbf{s}, t') P(\mathbf{r}, \boldsymbol{r'}, t - t')\, dV(\boldsymbol{r'}) \tag{2.18}$$

Integrating both sides of the equation in time $0 < t' < t$, the following is obtained, characterised by the time convolution of previous equation inside the integral.

$$t\, P(\boldsymbol{r}, \boldsymbol{s}, t) = \int_V \int_0^t P(\boldsymbol{r'}, \mathbf{s}, t') P(\mathbf{r}, \boldsymbol{r'}, t - t')\, dt'\, dV(\boldsymbol{r'}) \tag{2.19}$$

Dividing both sides of formula 2.19 by the general probability leads to

$$t = \frac{1}{P(\boldsymbol{r}, \boldsymbol{s}, t)} \int_V \int_0^t P(\boldsymbol{r'}, \mathbf{s}, t') P(\mathbf{r}, \boldsymbol{r'}, t - t')\, dt'\, dV(\boldsymbol{r'}) \tag{2.20}$$

The kernel is present inside the integral:

$$K(\boldsymbol{r'}, \mathbf{r}, \mathbf{s}, t) = \frac{1}{P(\boldsymbol{r}, \boldsymbol{s}, t)} \int_0^t P(\boldsymbol{r'}, \mathbf{s}, t') P(\mathbf{r}, \boldsymbol{r'}, t - t')\, dt' \tag{2.21}$$

then the travel time is expressed as

$$t = \int_V K(\boldsymbol{r'}, \mathbf{r}, \mathbf{s}, t)\, dV(\boldsymbol{r'}) \tag{2.22}$$

where $K(\boldsymbol{r'}, \mathbf{r}, \mathbf{s}, t)\, dV(\boldsymbol{r'})$, in this definition, shows the time of flight distribution of multiscattered waves from point $\mathbf{s}$ to point $\mathbf{r}$ passing through $\boldsymbol{r'}$.

Three-Dimensional Case

From equation (2.3/2.2), the definition of the sensitivity kernel for a 3D infinite medium has been obtained by Rossetto et al. [78]:

$$K(\boldsymbol{s},\boldsymbol{x},\boldsymbol{r},t) = \frac{1}{4\pi D}\left(\frac{1}{s}+\frac{1}{r}\right) e^{\frac{R^2-(s+r)^2}{4Dt}} \tag{2.23}$$

Due to the sever computational time of the kernel, the equation derivation, by Pacheco and Snieder [67], might become of fundamental importance. Referring to the generic kernel definition of equation 2.15, it starts from the numerator definition:

$$\int_0^t P_{3D}(\boldsymbol{s},\boldsymbol{x_0},u)P_{3D}(\boldsymbol{x_0},\boldsymbol{r},t-u)du \tag{2.24}$$

Knowing that $P_{3D}(\boldsymbol{s},\boldsymbol{x_0},u) = 0$ for $u < 0$ and $P_{3D}(\boldsymbol{x_0},\boldsymbol{r},t-u) = 0$ when $u > t$, the previous convolution becomes:

$$\int_{-\infty}^{\infty} P_{3D}(\boldsymbol{s},\boldsymbol{x_0},u)P_{3D}(\boldsymbol{x_0},\boldsymbol{r},t-u)du \tag{2.25}$$

The convolution can be rewritten, by means of the Laplace transform [1], as

$$\int_0^t F_1(t-r)F_2(r)dr = F_1 * F_2 \Longleftrightarrow f_1(s)f_2(s) \tag{2.26}$$

It is also possible not to consider the absorption parameter; i.e. the term $e^{-\frac{t}{\tau}}$ of equation 2.3 is not present in the kernel evaluation. In addition, the diffusion equation can be rewritten in equation 2.28 in terms of its Laplace transform

$$e^{-k\sqrt{s}}\ (k \geq 0) \Longleftrightarrow \frac{k}{2\sqrt{\pi t^3}}\, e^{-\frac{k^2}{4t}} \tag{2.27}$$

$$\frac{1}{4|\boldsymbol{r_2}-\boldsymbol{r_1}|\pi D}\,\frac{k}{2\sqrt{\pi t^3}}\, e^{-\frac{k^2}{ut}} \tag{2.28}$$

Finally, by substituting the latter relation in equation 2.15, it is possible to analytically obtain the three dimensional kernel definition of equation 2.23 [78].

Usually this formula can only be applied when the boundary conditions are uncomplicated. In fact it '*is generally not applicable under this form* (2.23) *because the transducers are usually located at the surface of the system*' [78].

2.3 Velocity Plot

The final point of the entire process consists in gaining the final complete velocity plots. By means of the *Inversion Technique*, indeed, the observed data ($\epsilon^{observed}$) is correlated to the statistical approach which allow to exploit the *apparent relative velocity variation* with respect to the surrounding area, obtaining a complete and more general *relative velocity change* $\frac{dv}{v}(x, y)$. Although the relative velocity variation is a continuous variable of the medium, it has been considered as a discrete value in the applied study.

2.3.1 Analytical definition

The theoretical field is based on the *diffusing acoustic wave spectroscopy* [67]. The dynamics of the scatterers, or in this case the propagation velocity, is obtained with respect to the fluctuations of the scattered wave field. In particular, a change in the diffuse wave propagation velocity leads to a corresponding phase change which can be used to extract the above-mentioned medium characteristics [67].

An acceptable assumption, already presented some paragraphs before, was to consider the perturbed and unperturbed data to represent the same scattering path. It also takes into account that the perturbed and non-perturbed signals appeared almost the same with a certain amount of delay between them.

It is possible to obtain the *mean length of scattering paths*, being analytically expressed as

$$\langle L(t) \rangle = \int_V \frac{1}{v} K(\boldsymbol{S}, \boldsymbol{R}, \boldsymbol{r'}, t)\, dV(\boldsymbol{r'}) \tag{2.29}$$

where v is the amount of velocity variation present in the specific area, K is the sensitivity kernel and $\boldsymbol{r'}$ refers to the point through which the wave scatters inside the entire medium V.

Applying a perturbation, the phase of the wave changes and, therefore, it is possible to describe the time variation for the specific trajectory T as:

$$\delta_T \equiv \langle \tau_T \rangle = \int_V \frac{\delta_v}{v} K(\boldsymbol{S}, \boldsymbol{R}, \boldsymbol{r'}, t)\, dV(\boldsymbol{r'}) = \frac{\sum_T I_T \tau_T}{\sum_T I_T} \tag{2.30}$$

In equation 2.30, the equivalence between the perturbation time of each infinitesimal volume and the average one results from the integration over the entire medium, where the sensitivity kernel plays the role of the intensity weight $\left(\frac{\sum I_T}{\sum I}\right)$ associated with each specific trajectory T [67].

This can be rewritten as a comparison between the velocity change $\epsilon^{observed}$ and a double integral, because of the 2D study, defined within the velocity variation area. In addition, equation 2.30 becomes

$$\epsilon(x,z,t) = \int_{x=left}^{x=right} \int_{z=lower}^{z=upper} \frac{K(\boldsymbol{S},\boldsymbol{R},\boldsymbol{r'},t)}{t} \frac{dv}{v}\, dz\, dx \tag{2.31}$$

due to the value of the relative velocity change: $\frac{dv}{v} \neq 0$, when $\boldsymbol{r} = \boldsymbol{r'}$, and $\frac{dv}{v} = 0$, whenever $\boldsymbol{r} \neq \boldsymbol{r'}$ [62]. The same equation can be rewritten without the integrals if the considered velocity variation is localised in a point (x_0 and z_0) within volume ΔV (or area ΔS) [63]

$$\epsilon(x_0,z_0,t) = \frac{K(\boldsymbol{S},\boldsymbol{R},x_0,z_0,t)}{t} \frac{dv}{v} \Delta V \tag{2.32}$$

2.3.2 Inversion Technique

As earlier specified, the entire velocity variation derivation can be described by the **forward** problem, in the form of discretized vectors and matrices

$$\mathbf{d} = \mathbf{G}\mathbf{m} \tag{2.33}$$

where $\mathbf{d}$ is the apparent velocity change vector, $\mathbf{G}$ is the matrix connecting the latter vector with $\mathbf{m}$, which contains the real velocity variations. They can be defined as:

$$\boldsymbol{d} = \epsilon_i, i = 1..n \tag{2.34}$$

$$\boldsymbol{m} = \frac{dv}{v}_j, j = 1..k \tag{2.35}$$

$$\boldsymbol{G} = \frac{K_{ij}}{t} \Delta S \tag{2.36}$$

Because of the same geometrical settings in the numerical and the real study, the n and m quantities are equal for both, where n refers to the source-receiver couple and m to the analysed grid point of the medium ($n = 5$ receivers $* 13$ sources $= 65$ and $k = 1001$ width $* 121$ height $= 121121$). ΔS is the area of the grid cell, equal to $100mm^2$, and t is the central time instant of the evaluated sensitivity kernel.

Having n elements and k unknowns defines an ill-posed problem. In order to obtain the relative velocity variation $\frac{dv}{v}$, the application of the *inversion criterion*, introduced by Tarantola and Valette in 1982, was fundamental. Its basic mathematical methodology relies on the *Least Squares Criterion* [89]:

$$\boldsymbol{m} = \boldsymbol{m_0} + \boldsymbol{C_m G^t}(\boldsymbol{G C_m G^t} + \boldsymbol{C_d})^{-1}(\boldsymbol{\epsilon} - \boldsymbol{G m_0}) \tag{2.37}$$

To find the actual velocity variations (**m**) it is necessary to identify a series of statistical factors belonging to equation 2.37. First of all, $\boldsymbol{m_0}$ is the a-priori model for the velocity distribution. Not having any information on the model makes $\boldsymbol{m_0}$ an $n * k$ columns zero-vector.

C_d is the diagonal covariance matrix (n x n) consisting of the variances $\sigma^2_{\mathbf{d}}$ from the obtained data. The standard deviation is defined in equation 2.38

$$\sigma_d = \frac{\sqrt{1 - CC^2}}{2CC} \sqrt{\frac{6\sqrt{\frac{\pi}{2}}}{f_\Delta (2\pi f_c)(t_2)(t_2^3 - t_1^3)}} \tag{2.38}$$

where f_c is the central frequency ($88kHz$), t_1 and t_2 are the begin and end instants of the chosen window, and f_Δ is the frequency bandwidth ($\frac{1}{t_1} - \frac{1}{t_2}$). CC contains the correlation coefficients referred to each of the specific 65 apparent relative velocity variations.

Matrix C_m, on the other hand, includes the non-diagonal covariance matrix of the model **m**, with dimensions k x k:

$$C_m = \left(\sigma_m \frac{L_0}{L}\right)^3 e - \frac{\Delta}{L} \tag{2.39}$$

where Δ represents the distances of each unit cell to the other areas, having, therefore, the same dimensions as C_m, L is the scaling length of every cell size ($10mm$) and L_0 is derived as the best trade-off with respect to σ_m. As specified in the observations of *Wenchuan earthquake* (Obermann et al. 2014) [64], "*the smoothness-data fit of velocity variation model is obtained from the L-curve*". For this study, common values found in literature were applied.

For practical implementation[3] reasons, it results noteworthy to specify the logical procedure followed to define the dimensions of the above-mentioned matrices related to the geometry of the beam. In fact, $\boldsymbol{m}$ has $n*k$ x 1 dimension, where each vector of length

---

[3] Code entirely developed in MATLAB [54] environment.

n showed the values of every row for all the specific k column positions in the matrix grid of the beam, thus k vectors of length n:

$$\begin{bmatrix} 1 \\ 2 \\ . \\ . \\ n \\ . \\ . \\ n * k \end{bmatrix}$$

The corresponding C_m matrix was developed with respect to $\boldsymbol{m}$, therefore, it had several columns for every single grid cell connected to all the other cells. Starting from the top-left cell, C_m is defined moving downwards until the bottom element of the matrix and, then, repeating the process once moved towards the adjacent column to the right. Thus, it resulted in a $n * k$ x $n * k$ matrix:

$$\begin{bmatrix} 1 \\ 2 \\ . \\ . \\ n \\ . \\ . \\ n * k \end{bmatrix} \begin{bmatrix} 1 \\ 2 \\ . \\ . \\ n \\ . \\ . \\ n * k \end{bmatrix} \cdots \begin{bmatrix} 1 \\ 2 \\ . \\ . \\ n \\ . \\ . \\ n * k \end{bmatrix}$$

Quite used is the application of such inversion technique for Coda Wave Decorrelation. The basics are the same but, now, the forward problem refers to new variables:

$$\boldsymbol{d} = DC_i, i = 1..n \tag{2.40}$$

$$\boldsymbol{m} = \sigma_j, j = 1..k \tag{2.41}$$

$$\boldsymbol{G} = \frac{c\,\Delta S\,K_{ij}}{2} \tag{2.42}$$

where DC stands for Decorrelation Coefficient (obtained as $1 - CC_i$), c is the wave velocity of the group, and σ_j contains the unknown *densities of scattering change*. The latter value, which can be related to possible presence of cracks inside the medium, deals with the amount of scattering which has changed from a uniform uncracked statistical distribution. Because of σ factors being necessarily positive, this inversion technique implements also an iterative procedure. After the first iteration, in fact, the positive σ are kept as starting input for the new model, until $\sigma_j > 0$, $\forall j = 1..n$.

3

Numerical Simulation

Having introduced and discussed all the conceptual steps regarding the application of the Coda-Wave Interferometry technique, the present chapter introduces the numerical simulation of concrete[4] and the extraction of a series of synthetic data. So, it was possible to investigate the reliability of such monitoring process. The path to follow is summarised with the steps listed below:

1. `Concrete Simulation`
2. `Diffusivity Question`
3. `Stretching`
4. `Sensitivity Kernel`
5. `Inversion procedure`

At the end of the chapter, the obtained results are discussed achieving a consistent set of information.

---

[4] The simulation advanced in accordance to fundamental scientific papers [67] [78] [62].

3.1 Simulation of Wave Propagation in Concrete

As a very first step, in order to properly develop the numerical study on stress, a reliable simulation of concrete must be accomplished. Among the many possible correct concrete reproductions, the work focused on a numerical approximation able to give appropriate interpretation with respect to the **wave velocity value**. The concrete composition can reach deep levels of specification: from cement paste, sand and gravel to the listing of more complicated secondary phases. In the present case, it required the essential definition of the various scatterers inside the medium, on which, indeed, the scattering criterion of interferometry is based.

The very basic notion of wave propagation through a medium relies on the estimation made on the randomness and inhomogeneity. The choice of such representation is strongly related to the *diffusivity constant*, which, defining the amount of scattering, needs to be somehow represented in the simulation.

3.1.1 The Von Karman Medium

The chosen model, due to the focus on velocity as the key element, was the **Von Karman medium**. Such a medium is identified as one for which '*an ensemble* (of property) *would represent same statistical characteristics*' [79] (e.g. same Auto Correlation Function and Power Spectral Density Function).

Even though widely treated in soil mechanics evaluations, the Von Karman medium is not commonly used to simulate an artificial material such as concrete. All the basic characteristics of the present simulation[5] were compared to specific concrete approximations [103] [104] rather than the classic soil media simulations [49] [67]. First of all, the assumed mean wave velocity as well as its variation showed a different scale of magnitude for concrete, with respect to usual soil values; at the same time, 'unconventional' central frequency of excitation was utilised for the signal emission. Furthermore, output parameters such as diffusivity and absorption time, needed to be properly interpreted and discussed.

As described in "*Seismic Wave Propagation and Scattering in the Heterogeneous Earth*" by Sato et al. [79], the velocity of a Von Karman medium is assumed to be

---

[5] The Von Karman simulation was developed in a Linux environment. Its computation was derived using the code written in FORTRAN by Dr. C. Weemstra

the sum of a constant value and a perturbation at each point $\boldsymbol{x}$:

$$v(\boldsymbol{x}) = v_0 + \delta v(\boldsymbol{x}) = v_0[1 + \xi(\boldsymbol{x})] \tag{3.1}$$

where v_0 is the constant value, and the non-dimensional quantity $\xi(\boldsymbol{x})$ defines the *fractional fluctuation of wave velocity* (also expressed as *f.v.f.*).

Fractional Fluctuation of Wave Velocity

It is by means of the distribution of fractional velocity fluctuation that the randomness property of the entire numerical medium is achieved. In this study, it was chosen that its average, out of an envelope, equals zero ($\langle \xi(x) \rangle = 0$), so that the median of all the velocities would result in $v(x) = v_0$.

For simplicity, the medium randomness magnitude is analytically defined with respect to the Auto Correlation function of $\xi(\boldsymbol{x})$, which is [73]

$$R(x) = \langle \xi(\mathbf{y})\xi(\mathbf{y} + \mathbf{x}) \rangle \tag{3.2}$$

The velocity fluctuation magnitude gets considered as its mean square σ^2, which coincides with $R(0)$. It needs to be specified that literature describes the mean square as 'ϵ'. However, this has no relation, and so, it must not be confused with the ϵ parameter discussed in the following chapters, related to velocity.

Correlation Distance

Another parameter of a Von Karman medium simulation is the *correlation distance* a, which describes the spatial variation of randomness which characterises the element under study when $R << \sigma^2$ for $r >> a$ [79], where r is the lag distance, which coincides with $|\boldsymbol{x}|$ for required randomness isotropy. The velocity and correlation distance of Von Karman properties are usually related as

$$R(a) = \frac{\sigma^2}{e} \equiv \frac{R(0)}{e} \tag{3.3}$$

In order to properly describe the medium, the Power Spectrum Density function (PSDF) can be used by transforming the Auto Correlation function (ACF) from the time to the frequency domain:

$$P(\boldsymbol{m}) = P(m) = \tilde{R}(x) = \int\int\int_{-\infty}^{\infty} R(x)e^{-i\boldsymbol{mx}}\,d\boldsymbol{x} \tag{3.4}$$

where $\mathbf{m}$ is the wave number and $\tilde{R}$ refers to a ACF space Fourier transform. P, in this section, represents the PSDF formulation, therefore, it is independent to the wave intensity analysis, previously discussed.

Random Medium formalisation

Once $P(\boldsymbol{x})$ is defined, it is possible to generate a random medium. In fact, the analytic description of the amplitude spectrum ($\tilde{\xi}(x) = \sqrt{P(\mathbf{m})}$) allows to obtain $\xi(x)$ and, with it, the entire randomness. The random phase spectrum $\Phi(\mathbf{m})$ was chosen between 0 and 2π:

$$\xi(x) = \frac{1}{(2\pi)^3}\int\int\int_{-\infty}^{\infty}\sqrt{P(\boldsymbol{m})e^{i\Phi(\boldsymbol{m})}e^{i\boldsymbol{mx}}\,d\boldsymbol{m}} \tag{3.5}$$

Among the several realisations of random medium which follow the same mathematical background (e.g. Exponential, Gaussian), the Von Karman Auto Correlation function is expressed as [90]

$$R(\boldsymbol{x}) = R(r) = \frac{2^{1-k}}{\Gamma(k)}\frac{r}{a}^{k} K_k\frac{r}{a}\sigma^2 \tag{3.6}$$

where K_k is the modified Bessel function of k-th order and $\Gamma(k)$ the gamma function, for $k = 0 \sim 1$. Sato et al. (2012) [79] provide the 3D PSDF equation, which presents a fundamental property due to its power-law decay behaviour; such nature is driven by the k parameter. The PSDF shows proportionality to $(am)^{-2k-3}$ for $am >> 1$. For the purpose of this study, the 2D PSDF considered was [62]

$$P_{2D}(m) = \frac{4\pi\Gamma(k+1)\sigma^2 a^2}{\Gamma(1 + a^2m^2)^{k+1}} \tag{3.7}$$

where $\boldsymbol{m} = \sqrt{(m_x)^2 + (m_y)^2}$.

3.1.2 Wave Propagation

With the two dimensional finite-difference code `fdelmodc`[6] [94], the study simulated the wave propagation inside the medium for various combinations of sources and receivers.

---

[6] The numerical modelling was performed in a Linux environment

Fulfilling specific stability demands (section 3.2.1) allowed to perform, and extract, a series of synthetic signals.

The numerical model was bounded by free boundaries. The selection considered this as the most reliable and analogous choice with respect to the lab-test case under study (choice also supported in Rossetto et al. - 2011 [78]).

As described later, evaluations were placed on the laboratory test calibration (section 3.1.4), in which were present both P and S-waves, as the medium is visco-**elastic**. The numerical modelling was performed assuming visco-**acoustic** wave distribution; i.e. only P-waves are present. This choice, evidently in disagreement with the laboratory calibration, was mainly driven by computational cost and successive signal evaluation and discussion. A more correct approximation would have resulted in a visco-elastic concrete evaluation. However, the numerical acoustic medium presented a series of features which took into consideration this conceptual difference, establishing a different but still coherent simulation.

As a source signal, it was used a *Ricket wavelet* delayed by $100\mu s$ (as visible in Figure 3.1). The centre frequency was the same as for the laboratory test Acoustic Emitters, i.e. $88kHz$ (chapter 4).

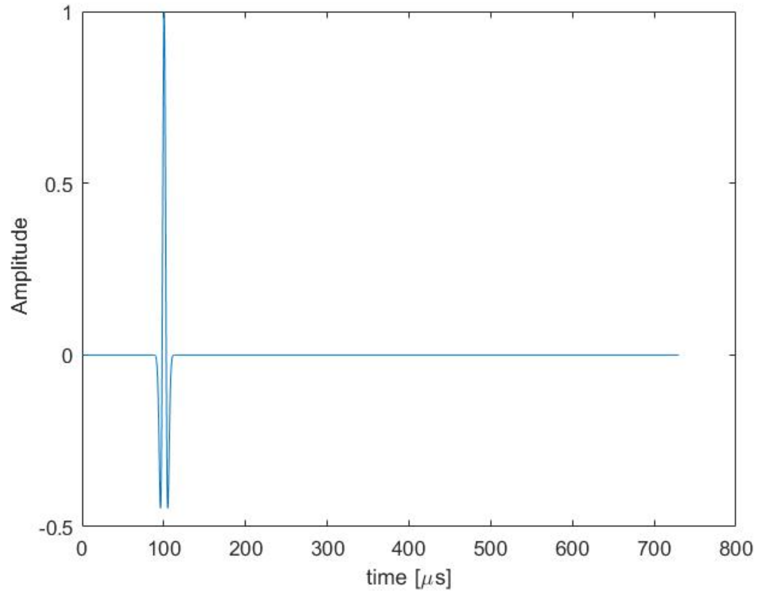

Figure 3.1: Ricket wavelet used as a source function

In order to have a graphical impression of the propagation of the wave, three snapshots have been taken from one of the simulations, developed over the work, see Figure 3.2.

The negative wave front appears to be in white and the positive in black. This example is modelled without dissipation, and so, the medium is purely **acoustic**; thus, the amplitude decay is a result of only the scattering.

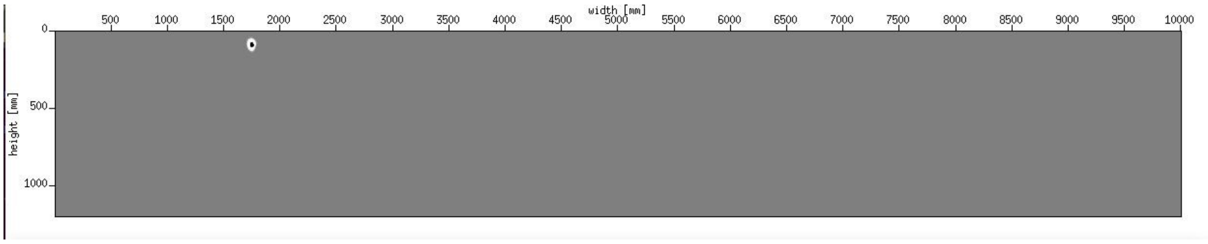

(a) Instant of the impulse emission: $t_{snap} = 0\mu s$

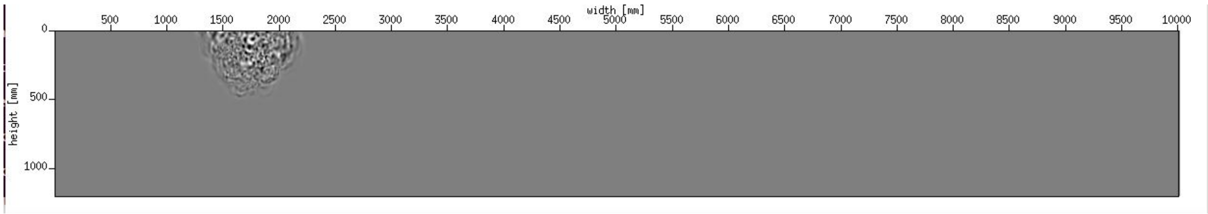

(b) Instant after $t_{snap} = 100\mu s$ from the impulse emission

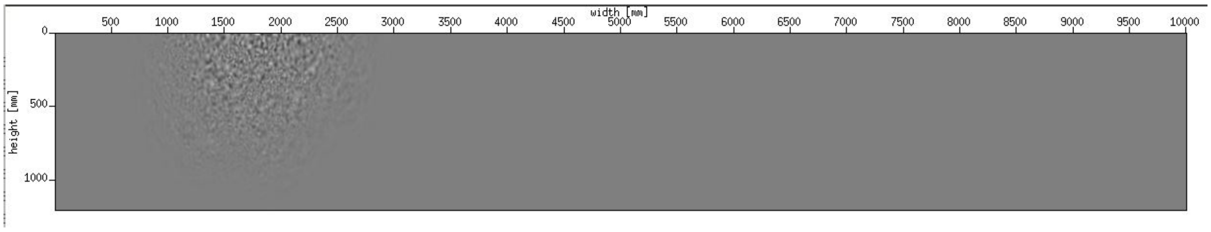

(c) Instant after $t_{snap} = 300\mu s$ from the impulse emission

Figure 3.2: Snapshots at various instants of wave propagation through the medium: **(a)** $0\mu s$, **(b)** $100\mu s$, **(c)** $300\mu s$. Note that these values are counted after the wavelet delay. Source positioned at $x = 1750mm$ and $y = 88mm$ (i.e. Acoustic Emitter 13).

3.1.3 Input Parameters Choice

Now, a proper choice of the parameter describing the Von Karman medium, i.e. velocity distribution σ and correlation distance a are chosen with respect to the numerical simulation of concrete[7].

In practice, this two input parameters give the analytical description of the area of inhomogeneities and the magnitude of variation between two consecutive heterogeneous

---

[7] In this case, best states for the one model which gives the lowest differences regarding wave propagation velocity and scattering, with respect to the real concrete element under parallel study.

elements. Such variation is expressed with respect to an energy loss. For the sake of completeness, it is important to remark that, actually, the mechanism of scattering is not related to the energy dissipation. In fact, the scattering energy does not get lost in the process but simply changes phase with respect to the exciting wave [4].

Figure 3.3 illustrates four different arrangements of σ and correlation length. From this figure, the following observations could be made:

1. As the correlation distance increases, the specific areas of inhomogeneity increase, leading to a different proportion of scattering (dispersion) inside the medium. Therefore, the dispersion magnitude decreases due to fewer and bigger areas of scatterers. It becomes noteworthy the dependency of the dispersion with respect to the specific wavelength of the signal.

2. The fractional velocity fluctuation, when increasing, expresses an higher and more abrupt variation in the velocity of a specific inhomogeneity (whose area is imposed by a) with respect to its neighbour. This leads to a higher fluctuation of velocity throughout the medium and a proportionally higher wave scattering attenuation.

Diffusion constant

The *diffusion constant* D defined as $D = \frac{cl^*}{d}$, is related to the scattering characteristic of the medium, where c is the mean wave propagation velocity in the medium, l^* the transport mean free path and d the number of dimension taken into account during the test [78] [103] [68]. The analytical definition of D is later introduced, in a different way, in section 3.3.2. The mean propagation velocity c consists of a combination of P-wave (v_p) and S-wave (v_s) velocities, generally expressed in literature as [63]

$$\frac{1}{c} = \frac{0.77}{v_s} + \frac{0.23}{v_p} \tag{3.8}$$

In this research, due to the purely acoustic medium setting, the velocity was considered to be uniquely defined by the P-wave (i.e. $c \equiv v_p = 4000 m/s$).

As already mentioned, because the diffusion is linked to the Von Karman main parameters, its definition was sensibly relevant for the identification of the correct numerical simulation. During the project, one of the main question was directed to the definition of a relationship between the diffusion constant and the correlation distance. In order to derive it, two Von Karman media without any internal dissipation were numerically simulated (Figure 3.4).

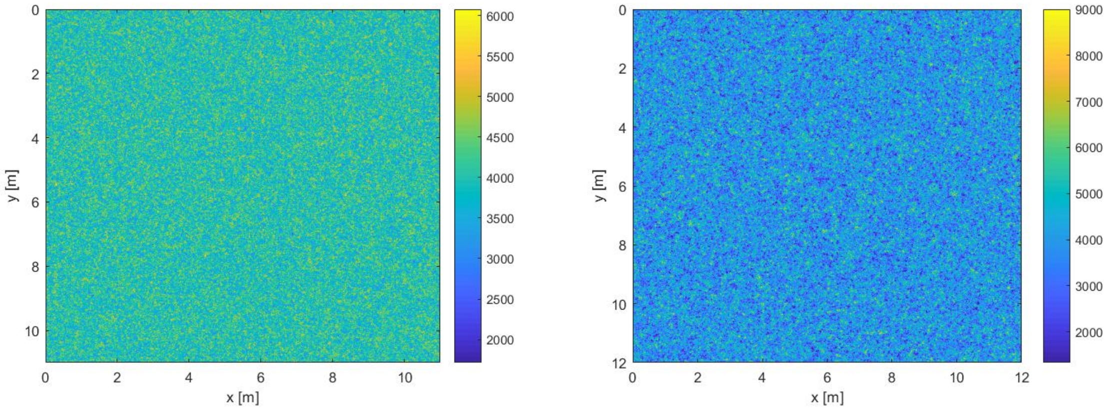

(a) $a = 3cm$ and $\sigma = 10\%$

(b) $a = 3cm$ and $\sigma = 25\%$

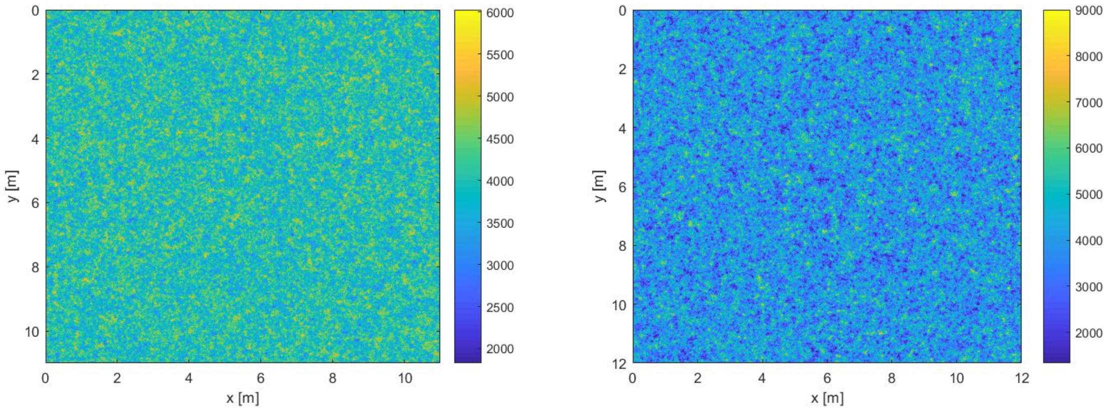

(c) $a = 5cm$ and $\sigma = 10\%$

(d) $a = 5cm$ and $\sigma = 25\%$

Figure 3.3: Four different arrangements of σ and correlation distance

1. A first analysis was performed with respect to a fractional velocity fluctuation of 25%, developed with geometrical settings of a square element $12m$ x $12m$, with source in the middle ($x = 6m$ and $y = 6m$) and purely reflecting edges. To give statistical redundancy, 100 receivers were placed in circle around the source at distance radii of $500mm$, $1000mm$, $1500mm$ and $2000mm$ (Figure 3.4a). The correlation distances considered were $1cm$, $3cm$ and $5cm$.

2. For the second one, the chosen dimensions were $11m$ x $11m$ also with the source in the middle ($x_{source} = 5.5m$ $y_{source} = 5.5m$) as well as purely reflecting boundaries. 100 receivers were placed in circle, around the source, at different radii (e.g. $500mm$, $700mm$ and $1000mm$); shown in Figure 3.4b. This second data set is considered with the fractional fluctuation of wave velocity equal to 10% and the correlation lengths were as in the precedent simulation.

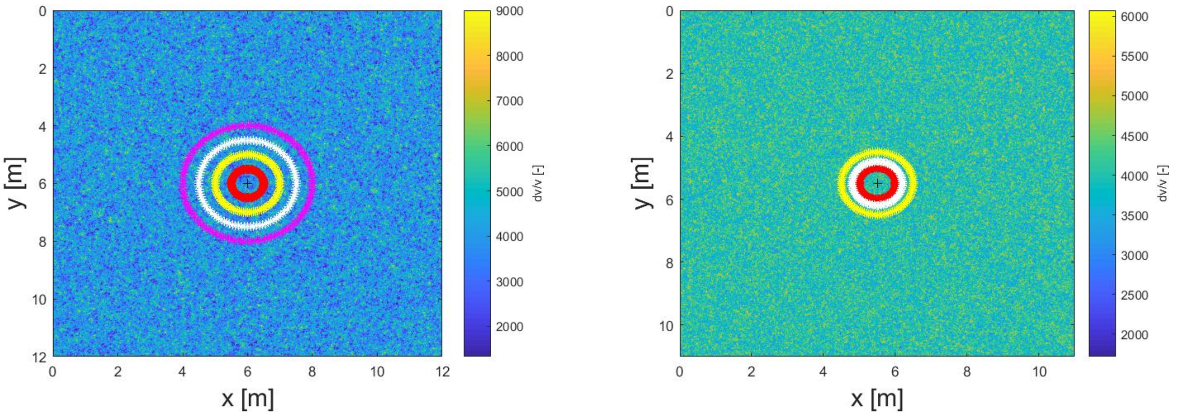

(a) First Source-Receiver scheme: $12m$ x $12m$ **(b)** Second Source-Receiver scheme: $11m$ x $11m$

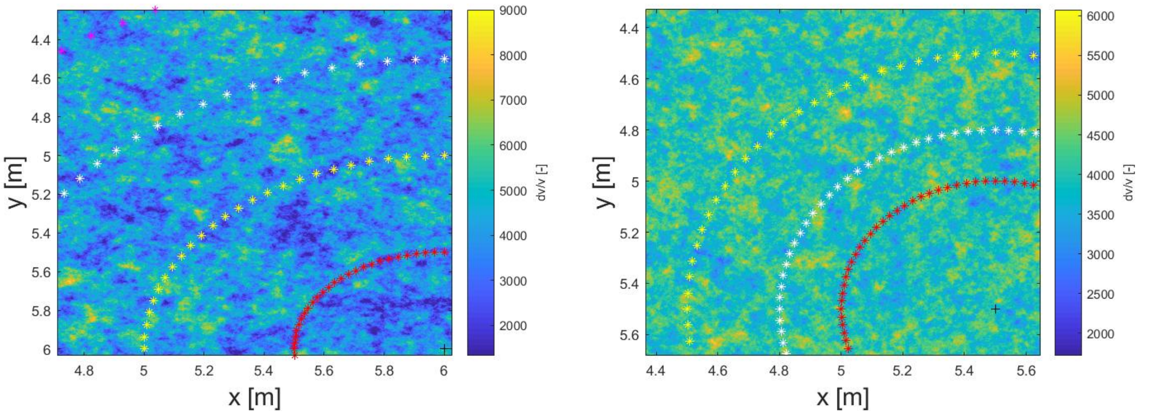

(c) Detail on first scheme **(d)** Detail on second scheme

Figure 3.4: Graphical representation of the two different settings. Example referred to $a = 3cm$, for both arrangements where $*$ represent receivers, and $+$ is the source.

As visible from the zoomed sections of Figures 3.4c and 3.4d, the constant number of receivers for each circle led to a constant spacing angle equal to $\pi/50$. This resulted in a variation of the sensors spacing with respect to every specific radius distance under study. A possible further improvement would consist of an inversely proportional spacing angle with respect to the distance. This approach would have led to the definition of different collection of receiver (i.e. data), for every specific circle. However, also at the maximum source-receiver length, of $2m$ and $1m$, respectively in magenta and yellow colour of Figures 3.4c and 3.4d, the constant distance angle between the receivers was considered to still fulfil the randomness requirement for the data extraction.

The dimensional divergence between the two analyses allowed to study different distances of source-receiver. To avoid any potential mistake, only direct signals from the source were considered, with no influence regarding reflected waves from any boundary disposition. This mainly drove the dimensional issue on how far placing the circle. As an example, the first arrangement had the highest radius at $2m$ due to the maximum distance allowed with respect to the mean velocity of the medium (extracted in the following section). In fact, in $2000\mu s$ the wave starts, gets reflected at the edge and comes back, without influencing the receiver at an available distance of $2m$ from the sensor; i.e. $v\,t = 4000m/s\,2$ x $10^{-3}s = d = 8m$. The same assumption drove the geometrical settings of the second analysis. Clearly, all this observations are approximated due to potential increment or reduction of velocity, for random location and magnitude of the scatterers.

Once the waves propagated, and various signals were obtained (paragraph 3.1.2), the first step consisted in averaging the 100 data to reduce possible local error and give redundancy. Due to computational timing, this was considered as an equivalent solution to the placement of a single receiver for 100 randomly different simulations. Shown in Figures 3.5 and 3.6, the example for $1m$ source-receiver distance for the first and second Von Karman settings.

An additional step, presented by Pacheco and Snieder (2004) [62] and by Obermann et al. (2013) [62] involved a further operation on the averaged data: enveloping the intensities ϕ^2 (where ϕ represents the amplitude of the signal), with respect to a period of windowing T (equation 3.9).

$$I(t) = \langle \phi(\tau)^2 \rangle_{\tau \in [t-T, t+T]} \tag{3.9}$$

Figure 3.7 presents a much smoother curve as well as a lower peak for the enveloped shape rather than the detected signal. In the end, we followed the enveloped path with a moving window of 11 fundamental periods ($11\,\frac{1}{88kHz} = 121\mu s$) overlapped by 50%; because of some small fluctuations of the energy envelope of the waves at nearby times, the window average became a smoothing operator which removed any fluctuating values. In the same Figure, it is shown the influence of σ parameter on wave propagation.

For the first analysis, four different distances implied four distinctive curves and relative envelopes, each with a specific peak. This was due to the lower scattering (no dissipation test) the wave has undergone, encountering a closer receiver rather than a distant one. In Figure 3.8, it is possible to immediately identify the influence of the several radii with respect to the σ parameter, leading to a deeply different curve shape and corresponding envelope.

The main difference is caused by the slower wave front, which requires more time to reach the receiver; being in such severe scattering environment, in fact, it is only at the

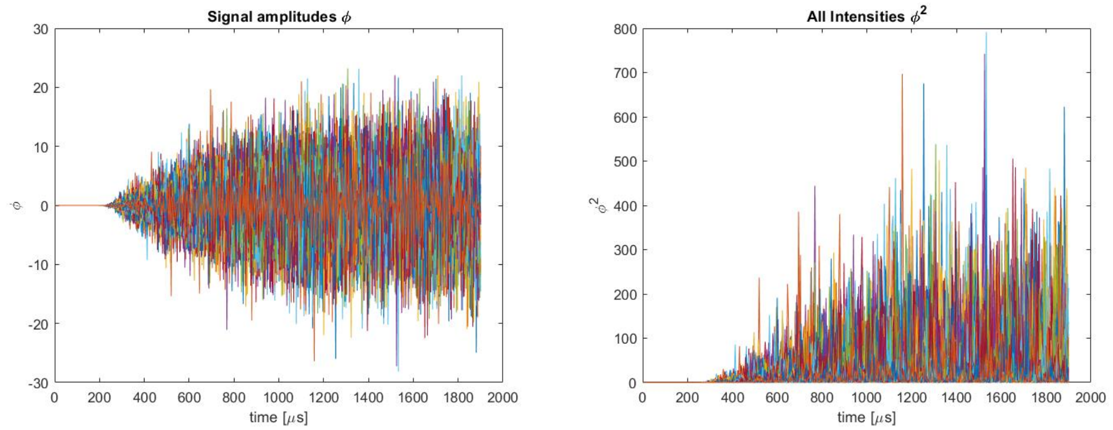

(a) all 100 amplitudes

(b) relative 100 intensities

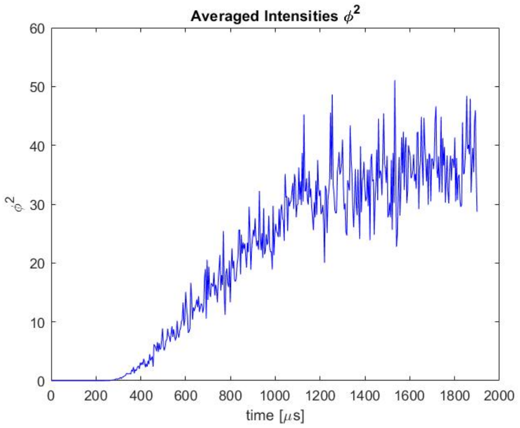

(c) averaged intensity

Figure 3.5: Graphical output of the three followed steps.The current example regards the $12m$ x $12m$ element with $3cm$ as correlation distance.

beginning (increasing) part of the curve.
Then, in the three data sets (corresponding to as many correlation lengths), a loop over the diffusion parameter D was applied to get the specific value which minimised the misfit[8] between the theoretical model and the synthetic data; all accomplished with respect to the four distances of source-receiver. Furthermore, for all the tests, a normalisation factor n was applied to the theoretical model (equation 2.3), to get comparable magnitude between the two curves. Such loop can be mathematically described by the following

---

[8] The fitting procedure is the first of a series of analysis performed on the synthetic and real signals by means of numerical computing environment MATLAB [54]

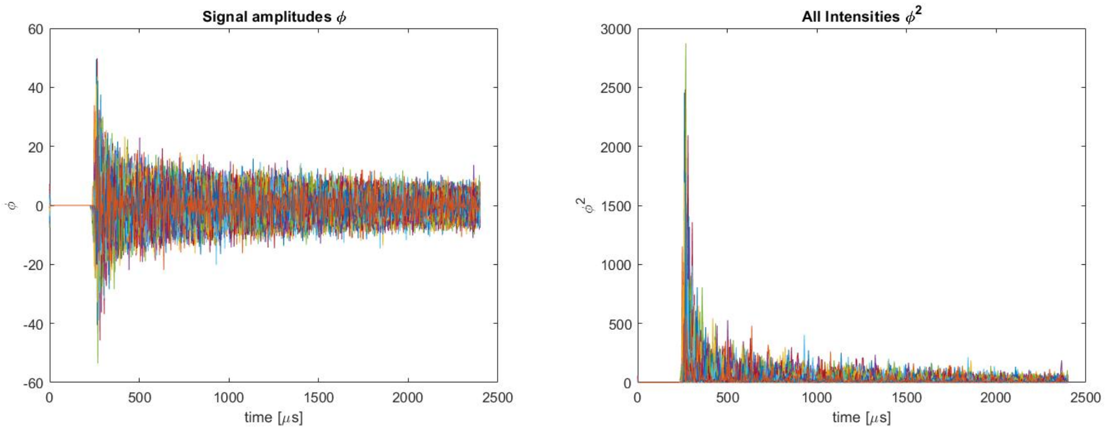

(a) all 100 amplitudes **(b)** relative 100 intensities

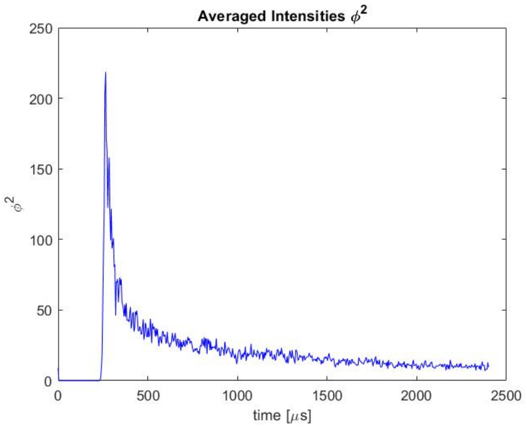

(c) averaged intensity

Figure 3.6: Graphical output of the three followed steps. For the current example, the $11m$ x $11m$ element with a correlation length of $3cm$.

relation

$$\sum_{n}\sum_{D=10}^{10000}\sum_{i=1}^{4}\sum_{t=1}^{2000}|n\,P(\boldsymbol{r},t,D)-Data(\boldsymbol{r},t)| \tag{3.10}$$

where n is the normalisation factor, D is the diffusion constant in $mm^2/\mu s$, i refers to the referred number of circle and t is the time expressed in μs. Figure 3.9 shows some fit for different distances of source-receiver.

The diffusivity factor was extracted from the mean of the four D values, for every distance, each with four different normalisation factors. In order to increase the reliability of this extraction, Figure 3.10 represents the overall misfit error analysis performed for all the $100 * 4 = 400$ signals, with respect to a unique couple of D and n. The analysis were carried for every single configuration of fractional fluctuation of wave velocity and

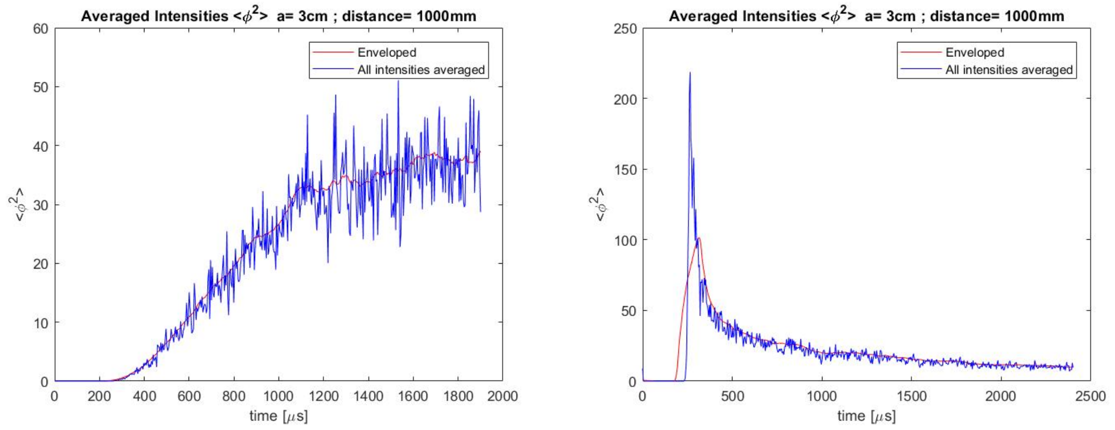

(a) Intensity envelope of a signal in the $12m$ x $12m$ element

(b) Intensity envelope of a signal in the $11m$ x $11m$ element

Figure 3.7: Averaged intensity of 100 receiver signals, at a distance of $1m$ (blue line), with its envelope (in red). The windowing period is $T = 121\mu s$ with an overlap of 50% between each window.

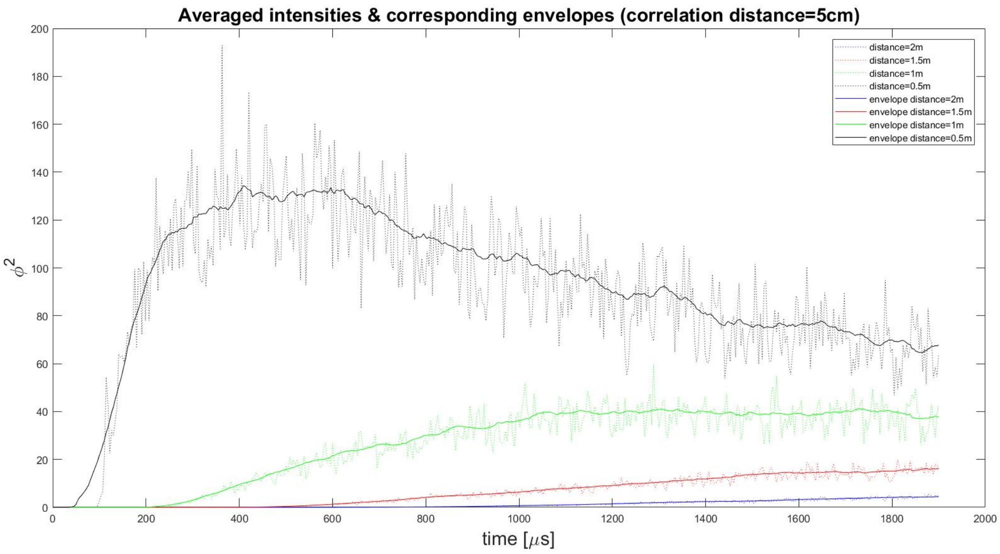

Figure 3.8: 4 intensities and relative envelopes defined for the three radii. In this figure, the $12m$ x $12m$ element, with a correlation length of $5cm$

correlation length, independently.

For what concerns the second Von Karman simulation and the signal influence of various source-receiver distances, Figure 3.11 represents the different received data.

The diffusivity investigation followed an analogous path to the previous one. Once extracted the averaged intensity, this simulation referred to the same loop expressed in equation 3.10. The distinction lied in the $\sum_i$ which, now, refers to just three distance radii for each correlation simulation. Another variation consisted in the normalisation factor n, resulting higher than before, because of the greater amplitudes to be normalised (i.e. due to the lower fractional fluctuation velocity).

Depicted in Figure (3.12) a series of fit for different radii of distance. As stated by the Figures 3.9 and 3.12, all the continuous synthetic red curves are fitted with a good approximation at 1.5 times the peak instant, by the blue dashed lines. This choice was

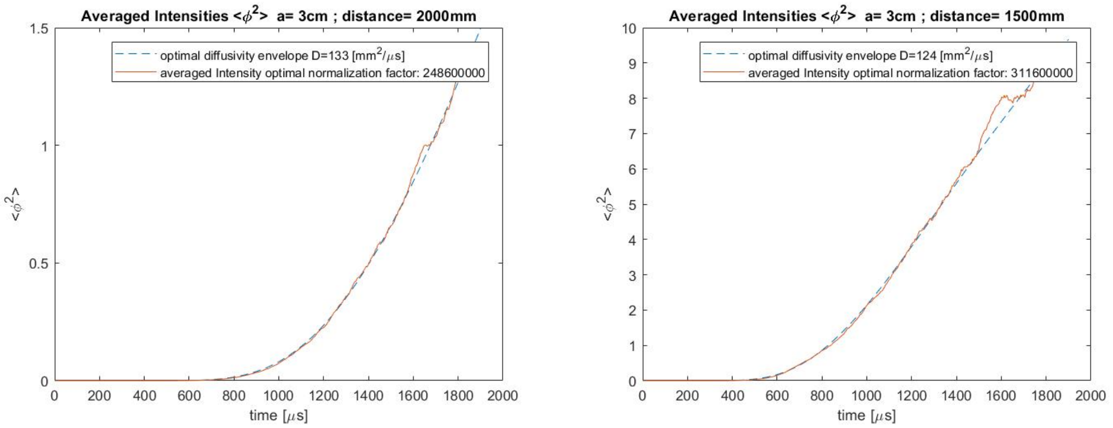

(a) Intensity envelope for $2m$ of source-receiver distance

(b) Intensity envelope for $1.5m$ of source-receiver distance

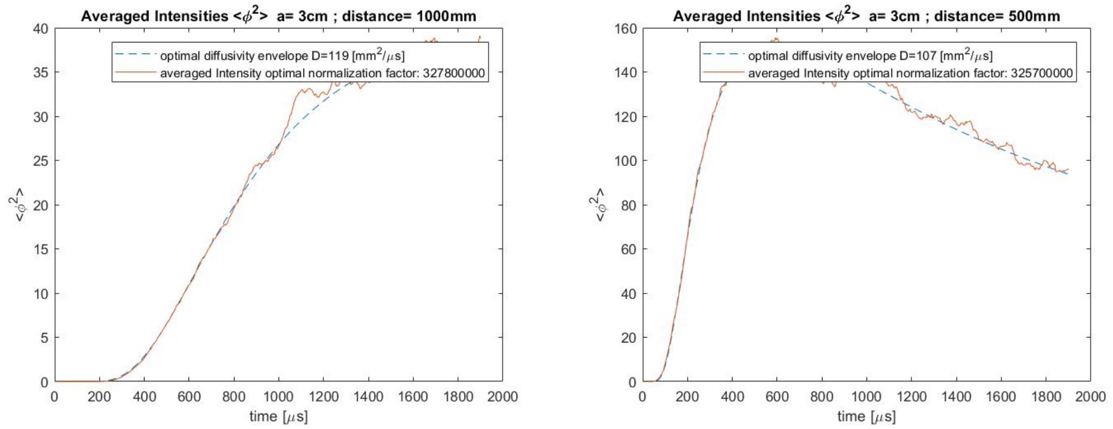

(c) Intensity envelope for $1m$ of source-receiver distance

(d) Intensity envelope for $0.5m$ of source-receiver distance

Figure 3.9: Intensity envelope and relative model as function of diffusion constant value and normalisation coefficient. Data derived from first medium simulation taking into account a correlation distance of $3cm$ and 25% of σ.

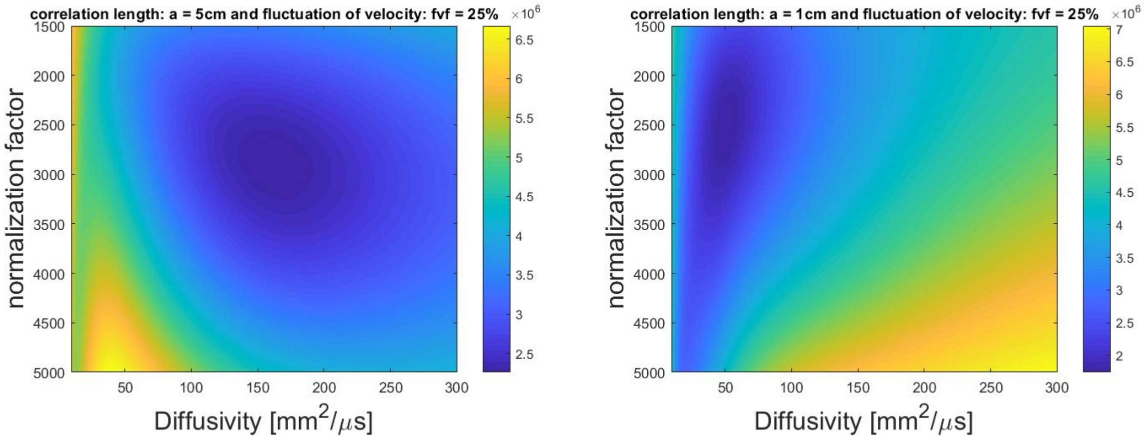

(a) Example for $a = 5cm$ with $\sigma = 25\%$ **(b)** Example for $a = 1cm$ with $\sigma = 25\%$

Figure 3.10: Colorplots of misfit errors between normalisation factor and diffusivity.

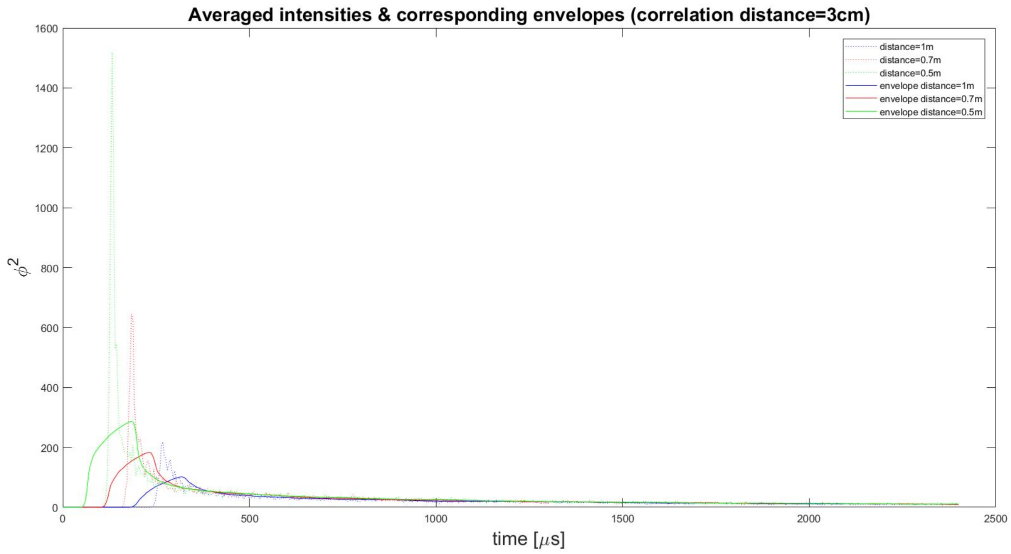

Figure 3.11: Three intensities and relative envelopes defined for the three radii. In this figure, the $11m$ x $11m$ element has a correlation length of $3cm$

driven not to consider any influence from the ballistic part of the wave which had no compelling information, with respect to the research focus.

Analogously to the previous simulation, the final D parameter came out of the three mean values, reciprocal to as many distances, each with three independent n values. To increase reliability, only one D and one n were extracted for all the 300 signals. The final comprehensive error plot is shown in Figure 3.13.

In the end, the main relationship between the diffusion constant and the two main parameters of the Von Karman medium resulted in:

1. As correlation length $a \nearrow$, $D \nearrow$. The higher the a factor, the lower the scattering (i.e. the area of velocity variation decrease) and the diffusion constant rises, resulting in an increase of wave diffusion throughout the medium.

2. As $\sigma \nearrow$, $D \searrow$; in this case, as the fractional fluctuation of wave velocity increases, the scattering increases (i.e. the steeper the velocity change gets for each area) so the diffusion constant decreases, which means that the effective wave diffusion diminishes.

The investigation of the diffusion constant was an important step in the entire research and its proper definition, and derivation, stated a crucial step for every future analysis

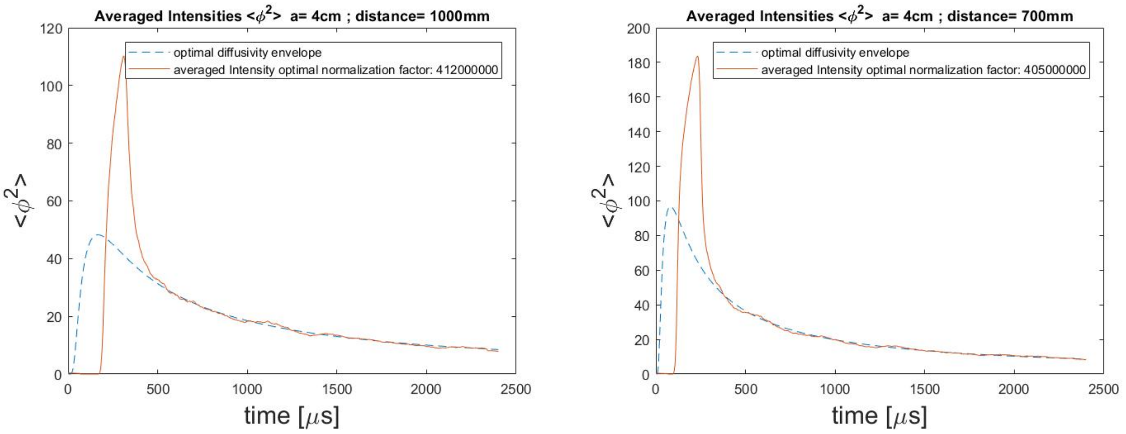

(a) Curve for $1m$ of source-receiver distance. **(b)** Curve for $0.7m$ of source-receiver distance.

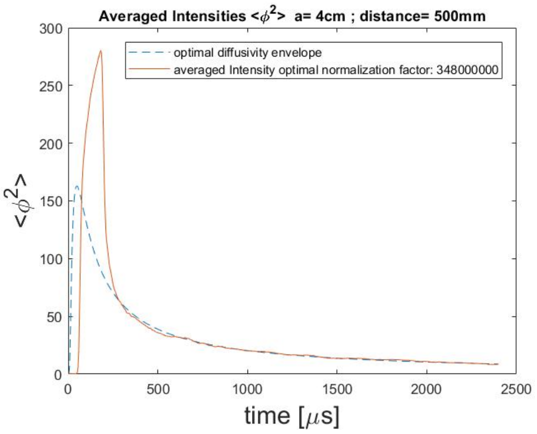

(c) Curve for $0.5m$ of source-receiver distance.

Figure 3.12: Intensity envelopes and relative model as function of the normalisation coefficient. Example selected from second simulation with $a = 5cm$

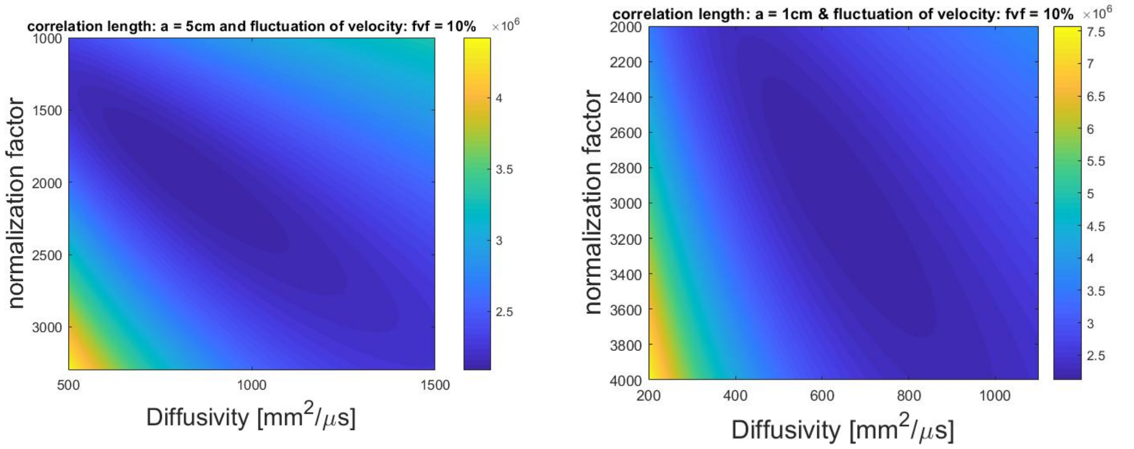

(a) Example for $a = 5cm$ and $\sigma = 10\%$

(b) Example for $a = 1cm$ and $\sigma = 10\%$

Figure 3.13: Colorplots of misfit errors between normalisation factor and diffusivity.

in the field.

It is of interesting horizons the derived graph 3.14, which places in relation the diffusivity constant and the correlation distance, with respect to the specific fractional fluctuation of wave velocity value.

The relationship between the two parameters appears to be in accordance to the previously discussed observations. The shape of the curves, however, does not look similar for both σ values, thus, a unique formulation cannot be entirely extracted. Such arches were fitted with linear curves, shown in the graph 3.14. To increase the accuracy, an essential operation would consist in obtaining as much data as possible. However, every single diffusivity point comes from the mean of a series of interpolation works, made for different distances of source-receiver, with respect to a specific value of correlation length. It would result, therefore, in a severe depriving computational timing.

Absorption parameter

The τ parameter of the diffusion equation (2.3) takes into account the internal dissipation of the wave, whilst propagating through the medium. Such value states a deep importance when it comes to the decay of the exponential curve during the misfit evaluation. In order to properly identify such a parameter, and to give redundancy to the research itself, a series of step were processed.

By means of the two Von Karman media, derived in the earlier evaluation step, the same model was defined with dissipation properties. The subsequent phase consisted in obtaining the specific τ value which gave the best fit (i.e. lowest misfit) with respect

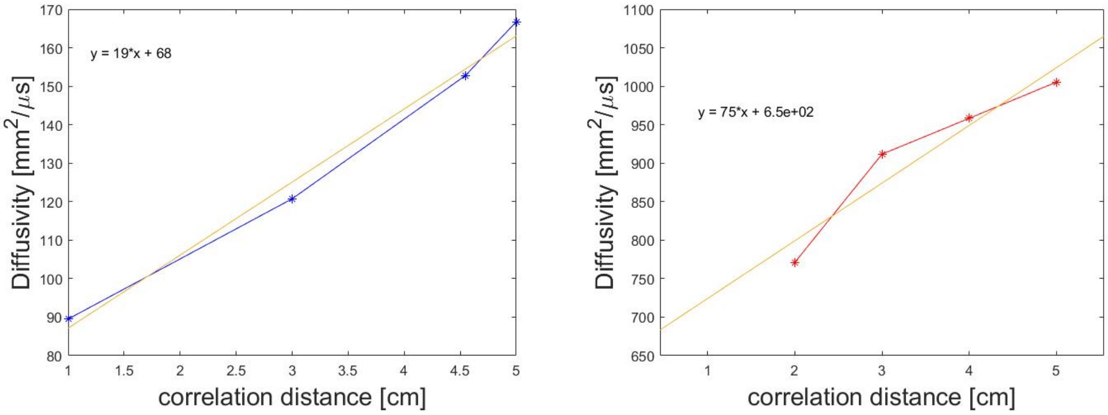

(a) Curve for $\sigma = 25\%$ with linear fit curve.

(b) Curve for $\sigma = 10\%$ with linear fit curve.

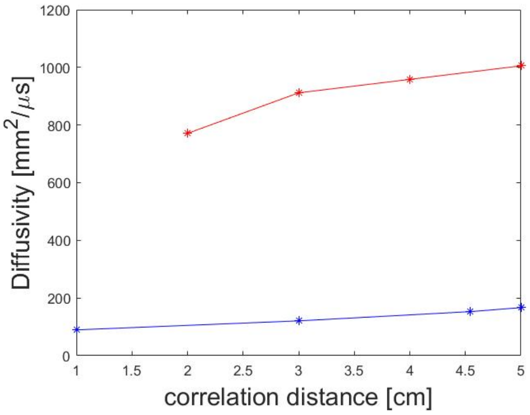

(c) Blue curve for $\sigma = 25\%$ and red curve for $\sigma = 10\%$

Figure 3.14: Relationship between diffusivity constant D and correlation length a

to the already identified and discussed diffusion constant D. The diffusion constant is indeed a unique property of the medium, thus, its value can be considered trustworthy and fixed for all the other tests within the same simulated sets of parameters, leading the research towards a reliable Von Karman numerical simulation.

The following step needed to apply dissipation to the medium and to the wave distribution. Such choice is described in the following paragraph, where the internal dissipation magnitude inside the medium gets introduced in parallel to the parameter 'Q'.

3.1.4 Real Test Calibration

Throughout the research, in order to reach a certain level of consistency, a calibration of synthetic data was needed with paramount importance. The correct input must be

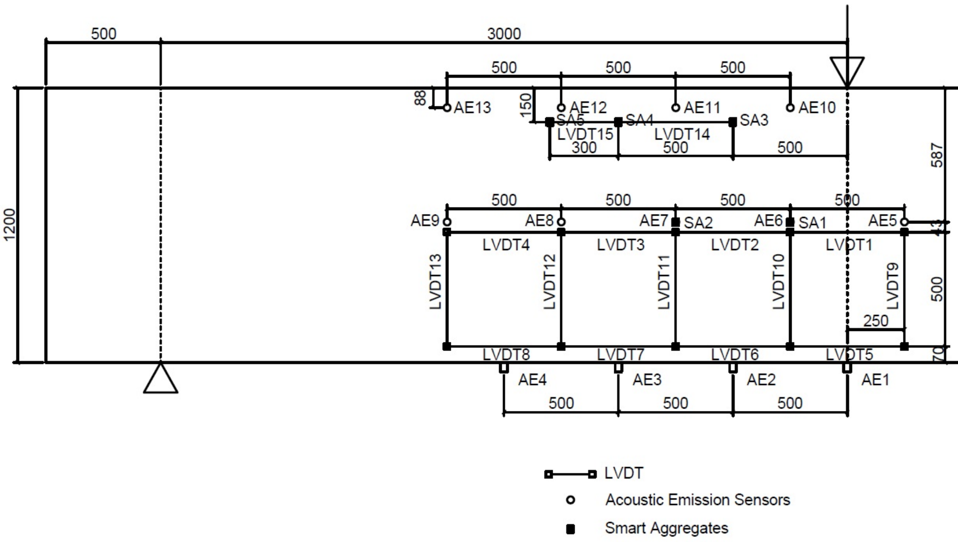

Figure 3.15: Layout of the laboratory beam in bending. Courtesy of F. Zhang.

substantial to provide reliability during the extraction and analysis of the final outputs, proving whether or not this theory can be a strong ally in the Structural Health Monitoring field. To reach so, some data from a real beam[9] were studied. The geometrical set up of such a beam, as well as the sensors locations, was entirely reproduced in the numerical study to give redundancy and, up to some extent, loyalty to reality. The element under analysis was a concrete beam $1.2m$ high and $10m$ wide, which drove the geometric features of the Von Karman simulation for the analogous 2D element.

It was possible, in fact, to investigate both the diffusion and the absorption constants, gaining the lowest misfit between the laboratory data and the mathematical model.

Overall, the study had 13 sources per 5 receivers, resulting in 65 couples of data set, placed accordingly to the scheme of Figure 3.15. The signals from couples AE13-SA1, AE1-SA5, AE4-SA3 and AE10-SA5 (where AE refers to Acoustic Emitter and SA to Smart Aggregate) are shown in Figure 3.16, where the highest possible distance between the sensors assuredly led to a multi-scattering regime. Without any doubts, indeed, at those distances, the scattering mean free path is surpassed [103] [4].

It is clear how these plots show certain attenuation of the wave amplitude. After a

---

[9] Actual wave propagation data were extracted in parallel from a test, performed in Stevin-II laboratory at T.U. Delft, which was focused on the very same research field (i.e. CWI).

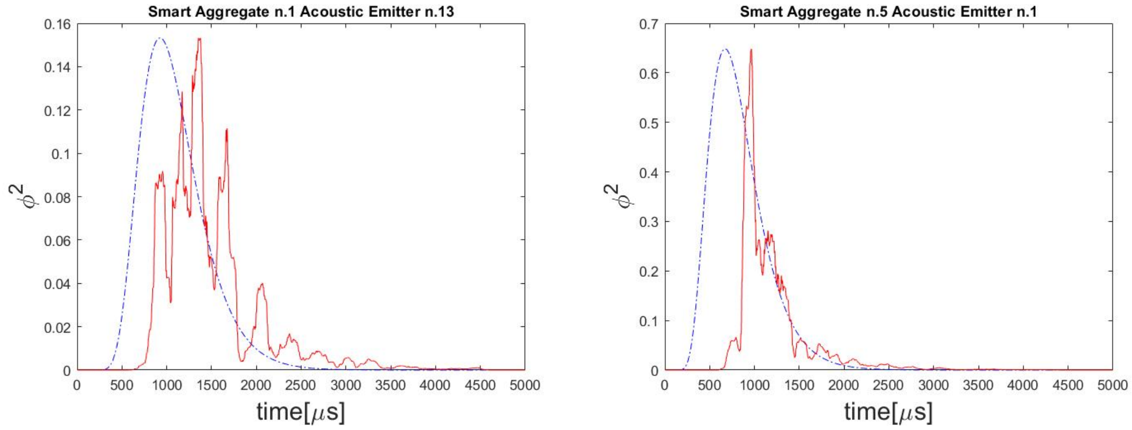

(a) Pair SA1-AE13

(b) Pair SA5-AE1

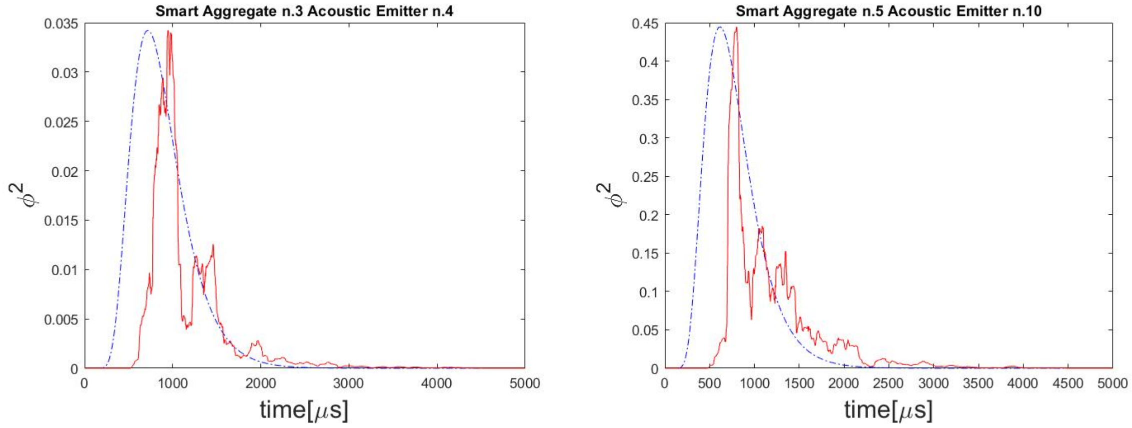

(c) Pair SA3-AE4

(d) Pair SA5-AE10

Figure 3.16: Modelled wave, with respect to τ, D and normalisation factor (blue), and received - filtered - signal (red).

relatively wide plateau at the peak, there is a descendant regime where the combined effect of internal dissipation and scattering leads to the progressive weakening of the signal.

Another fundamental detail regards the nature of each signal, present in the spectrum, and why the real data slightly differed from the synthetic ones. Considering the visco-elastic behavioural approximation of the laboratory test, the wave fields showed P-waves as well as S-waves. Throughout the numerical simulation, instead, the concrete regime was considered as visco-acoustic, thus focused on an investigation of only the P-wave. By means of the Fourier transform, the frequency of the wave is shown for the laboratory data. Clearly, the real signals present a much less precise definition and an higher number of frequencies (i.e. due to the physical limits of practical testing). Moreover, the test performed in lab does not show any simplistic feature with respect, as an example, to the *visco-acoustic* numerical study. Therefore, it is important to specify which type of wave reaches the sensors.

As shown in the Figure 3.17, the Fourier Transform spectrum did not allow to divide the S-waves from the P-waves in the signal. Furthermore, the coda section was characterised by PS-waves and SP-waves, other than purely S-waves and purely P-waves [82]. From Figure 3.17, two different peak areas were observed. One at $88kHz$, which is the actual central frequency of the signal, and a second one in between $10kHz$ - $20kHz$. This additional main frequency might have been generated from an energy redistribution of the signal inside the beam. This part was unwanted, so, to make it closer to the simulation, which does not show any applicability errors of this kind, an high-band-pass filter was employed, with a cut-off frequency of $f_{cutoff} = 50kHz$. This approach led to the new spectrum, consisting of only the actual emitted peak of central frequency, even though devoid of any separation between P and S waves and their interactions (shown as example in Figure 3.18).

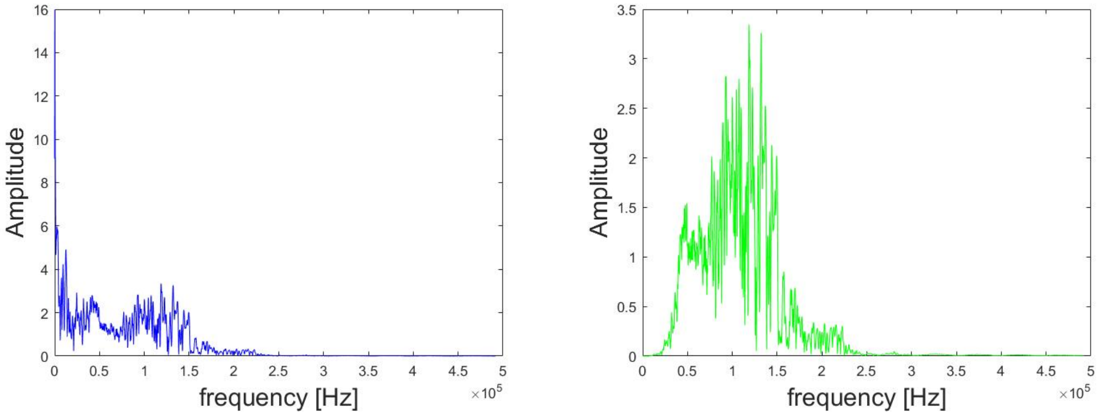

Figure 3.17: Spectrum of real data signal (in blue) and spectrum after filtering (in green). Example for Acoustic Emitter n.4 and Smart Aggregate n.1.

3.1.5 Numerical Formulation of the Medium

Finally, it was possible to enumerate the different parameters defined for the best Von Karman simulation. First of all, the mean velocity magnitude in the medium was appointed to be $4000m/s$, presenting a delay of the early arrival with, almost, same magnitude as the real data. The real test presented a series of imperfections and sensitivity errors, impossible to reproduce in the approximation.

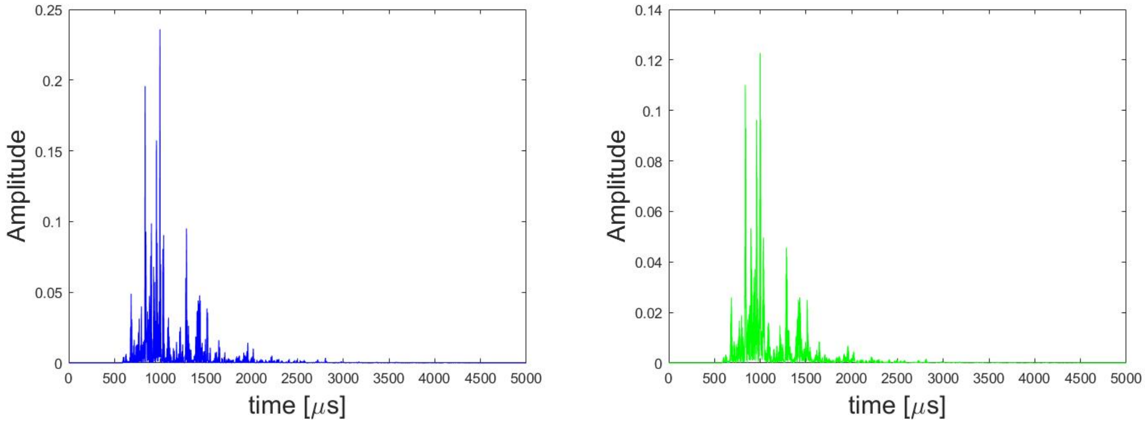

Figure 3.18: Signal before (blue) and after (green) the filtering procedure. Example for Acoustic Emitter n.4 and Smart Aggregate n.1.

In order to have the similar and unique value of diffusion through the medium and, at the same time, equal to the real one, a correlation length of $a = 4.545cm$ was selected. As described in the previous section, this choice found its origins in the inhomogeneity dimensions which triggers the *multi-scattering regime*. Its definition comes, in accordance to literature [62], from which the wavelength dimension times the velocity of wave propagation in the medium defines the correlation length: $a \approx \frac{1}{88kHz} * 4000m/s = 4.5454cm$.

For what concerned the absorption time, this was strongly affected by the selected value of diffusivity. In the end, it was possible to assess that such a parameter was chosen from the theoretical definition found in the literature of geophysics. Described in *Seismic interferometry, intrinsic losses and Q-estimation*, by Draganov et al. [26], in fact, this coefficient is often identified with respect to the square root of the velocity factor in each heterogeneity area. Then, in the following simulation, the internal dissipation shall have, for every correlation area, a unique value of velocity v_i and a specific dissipation factor Q_i, referred to the square root of the velocity field.

Two main procedure for the identification of the value are presented: the first one was numerically implemented, while the second was pursued in the theoretical evaluation.

1. One approach consisted in generating, for every single area of velocity change, inside the medium, a corresponding file which had, within the i-th region, a singular value of dissipation. In geophysics, this is usually obtained as the square root of the velocity: $Q_i = \sqrt{v_i}$.

2. Analogously to the first procedure, a parallel and more simplistic approach consisted in associating with the entire medium the square root of the average velocity: $Q =$

$\sqrt{v_{mean}} = \sqrt{4000} = 63.25$.

Once obtained the synthetic data, the goal was to define the specific τ value which could give the best fit (i.e. lowest misfit) with respect to the already identified and discussed diffusion constant. The dissipation factor, in practice, can be related to the "real" absorption time through

$$\tau = \frac{Q}{f_0 \pi} \tag{3.11}$$

Having specified the theoretical relation, the absorption time resulted in $\tau = \frac{63.2455}{88000\pi} = 2.28769 \text{ x } 10^{-4}s = 228.75\mu s \approx 229\mu s$. With this τ factor, the diffusivity fit was reproduced for different source-receiver pairs. As explained in the next chapter, this value shall be unique for the entire medium, being a property of the material. Nevertheless, every couple showed a different behaviour and, thus, slightly different constants were derived after fitting. This must found its reason in a series of simplistic estimation developed throughout the research and applied to the real data which do not take into account specific conditions. Finally, shown in tables 3.1 (also in tables A.2 and A.1) all the different variations of diffusion constant with respect to the initially chosen source-receiver pairs.

Table 3.1: Obtained diffusivity from laboratory test signals (source Acoustic Emitter n.4) with respect to specified dissipation factors. A series of τ are here represented.

			AE4			
τ	**SA1**	**SA2**	**SA3**	**SA4**	**SA5**	**MEAN**
300	318	187	250	191	144	218
229	211	129	177	130	98	149
200	169	107	146	109	82	123
165	128	85	113	85	64	95
50	21	17	19	18	13	18

The selected parameter comes from the mean value which is $D = 149mm^2/\mu s$. In addition, as the absorption time τ decreases, the D - best fit - value decreases as well. This result gets justified by considering that the actual diffusion/dispersion inside the medium remains the same; i.e. the D factor needs to decrease, so that the theoretical model increases the scattering, balancing the absence of internal absorption.

Analogously to the evaluation developed in the previous section (for normalisation and diffusivity related to correlation length), an error colorplot from the fitting model was obtained, with respect to the two main parameters. Because of the strong dependency between τ and the extracted D, to increase the reliability, only one τ factor and one D value were selected for all the signals (i.e. 65). This allowed to gain a consistent pair of parameters, while proving the previously shown tables. Figure 3.19 presents the proportional, almost quadratic, dependency in the model between the two constants.

Defining a lower threshold for the absorption time agrees with the theoretical background. Indeed, a too small τ would generate a non physical magnitude of internal dissipation within concrete, which would define a too high relative D (i.e. as previously mentioned, the model describes a balance between τ and the diffusivity). So, an horizontal line of $\tau = 229\mu s$, chosen in accordance to the earlier discussion [26], was considered as lower threshold. The D factor could be over the entire line within the region of lowest error, namely from $150mm^2/\mu s$ to $700mm^2/\mu s$ (Figure 3.20). However, choosing a unique value of D for all the 65 signals led the diffusivity definition to $150mm/\mu s$.

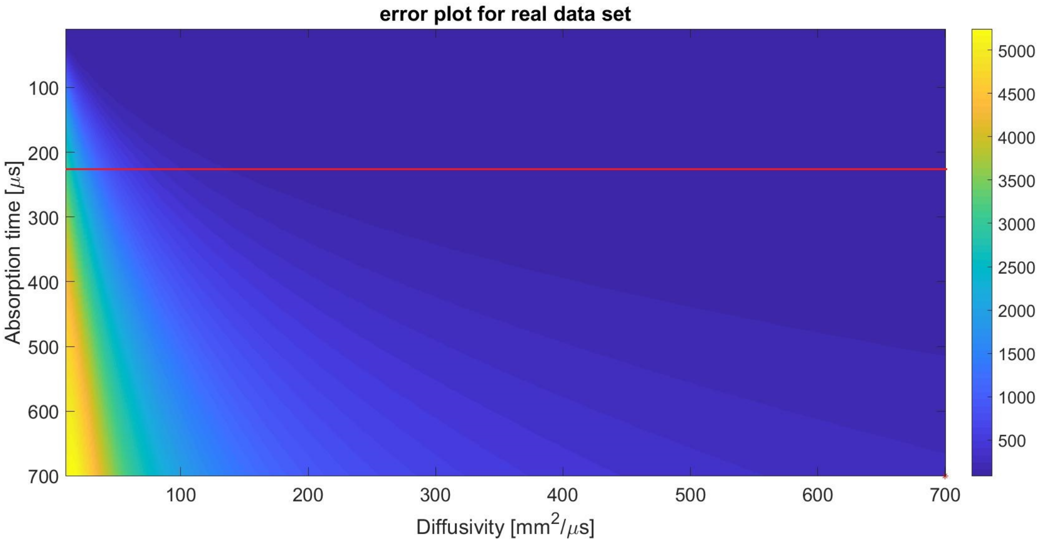

Figure 3.19: Real test calibration: colorplot of the misfit error between τ and D parameters. In red the lower threshold of $\tau = 229\mu s$.

Referring to graph 3.14 (developed for simulated data), the Von Karman medium which reached a $\sigma = 25\%$, with the previously discussed correlation distance of $a = 4.5454cm$, resulted in having a synthetic diffusivity value of $152mm^2/\mu s$, which approximately matched the real one.

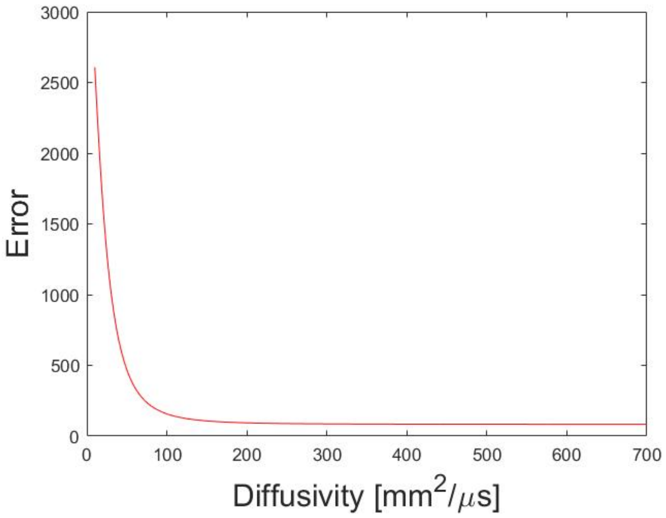

Figure 3.20: Real test calibration: error values, along the D red-line of Figure 3.19, for a fixed $\tau = 229\mu s$.

3.2 Stretching

A further step in the Interferometry process, focused on the stretching procedure. As introduced in the theoretical CWI chapter, the *stretching technique* consists of a process which allows the extraction of the relative variation of velocity suffered by a medium, with respect to two different data sets. Where one refers to the unperturbed while the other one shows the signal perturbed by a velocity variation. This operation relies on the basic concept that, whenever a wave is shortened or elongated, the consequently perturbed signal almost keeps the same shape, but translated forwards or backwards of a specific[10] value dv/v.

3.2.1 Area Settings

The main focus of the numerical stretching was placed on the Von Karman simulation main parameter to undergo some variation. It is the velocity, indeed, which reflects stress changes with respect to the acoustoelastic theory [2]. The work was structured to synthetically apply a velocity change to the medium, and to successively process the CWI, in order to investigate the technique capability to identify the area and to determine up to what extent its relative dv/v magnitude is. Thus, the numerical definition of the perturbed medium covered an important step of this study. If the area under relative

---

[10] The stretching evaluation was implemented by a MATLAB function defined by Dr. A. Obermann.

velocity change is in between the connection line (i.e. in the middle of source-receiver line) the shift is observed by the ballistic and the coda wave. When these are, instead, outside of the line, the stretch gets detected only by the late arrivals.

We developed a series of attempts characterised by different arrangements to give redundancy to the calculation. Some investigation were carried out considering various velocity changes within an area of $10mm^2$, some other were conducted with respect to larger portions (i.e. $500mm^2$) each as well with distinct variation amplitudes.

Due to the limits of the wave propagation[6] numerical simulation (section 3.1.2), lower and upper velocity boundaries were selected according to equations 3.12 and 3.13. The maximum velocity to be reached in the medium is set to $9000m/s$; this choice comes from a stability point of view. With a time step of $\Delta t = 7.1x10^{-7}s$ and a central frequency of $88kHz$, the maximum velocity follows the approximation:

$$\Delta t < \frac{0.606\Delta h}{c_{max}} \tag{3.12}$$

where Δh is the discretization step, and c_{max} is the highest possible velocity. The constant 0.606 comes from the 4th order spatial derivative (i.e. *Courant number*) [94] [17]. The minimum velocity, instead, comes from a wavefield dispersion concept: avoiding a strong dispersion of 2D wave, the minimum velocity is found equal to $1350m/s$.

$$\Delta_h < \frac{c_{min}}{5f_{max}} \tag{3.13}$$

where f_{max} represents the maximum frequency ($f_{max} \equiv f_{central}$ for an impulse), c_{min} is the lowest possible velocity and the constant value 5 comes from the “5 points per wavelength” rule of thumb.

Velocity Variation

For the synthetic definition of perturbed medium, we initially questioned how to exactly modify the velocity field in the beam. Due to the randomness property of Von Karman medium, applying the variation could result in two main approaches:

1. Alter the velocity field by adding or reducing a constant value. This way, the entire modified section would present a reduction/increase of velocity independent of whether the value would be higher or lower than the mean one.
2. Place the velocity variation by means of a percentage within the area. The section would suffer an overall change in the aforesaid field.

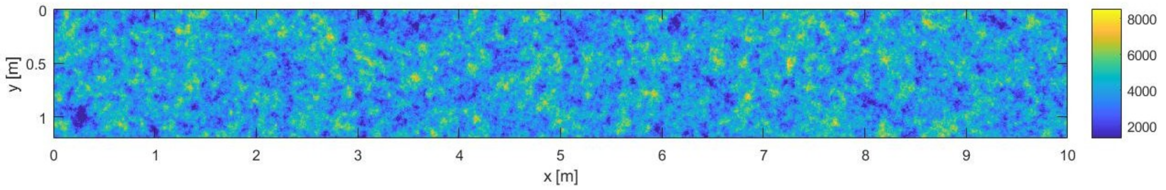

(a) Unperturbed beam

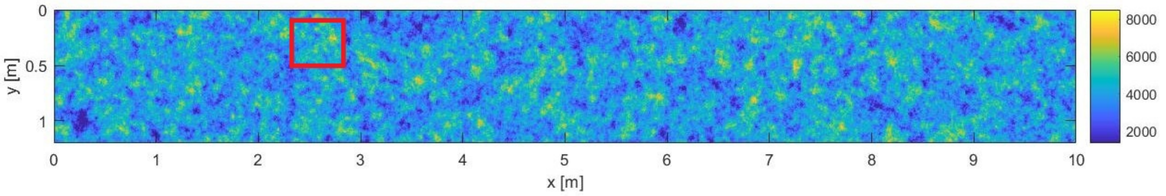

(b) Perturbed beam with $\Delta v = -100 m/s$ over an area of $500 mm^2$.

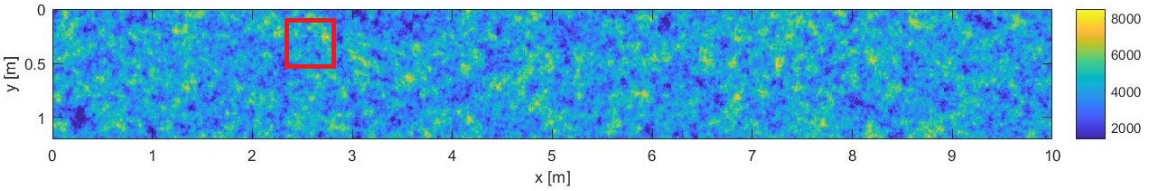

(c) Perturbed beam with $\Delta v = -1000 m/s$ over an area of $500 mm^2$.

Figure 3.21: Graphical representation of the simulated beams with respect to velocity field

This step was carried out with respect to both methodologies. However, only the first one gave reliable and consistent outcomes; therefore, it is the only one presented. The whole analysis focused on a $\frac{dv}{v}$ variation area of $500 mm^2$, centred in $x = 2600 mm$ and $y = 300 mm$ with velocity variation of $\Delta v = -150 m/s$ and $\Delta v = -1000 m/s$. The two analyses, in the stretching approach, presented different variation of the extracted velocity magnitudes. Because of the strong difference in the Δv amplitude, which, in the first case, gave rise to a modest slowing down of the wave while, in the second, generated an inconsistent different signal. Here, the Figure 3.21 of the unperturbed data with the corresponding perturbed one, for both configurations.

Another analysis was implemented with respect to a change area of $10 mm^2$. The study considered two Δv of $-150 m/s$ and $-1000 m/s$, respectively. With this small area outside any source-receiver line, no first arrivals were strongly influenced. On the other hand, the coda showed some changes, especially when the direct connection line got closer to influenced the area. The second velocity change, instead, did not show a shortening in the signal but a more severe variation. Therefore, this data set was produced but not

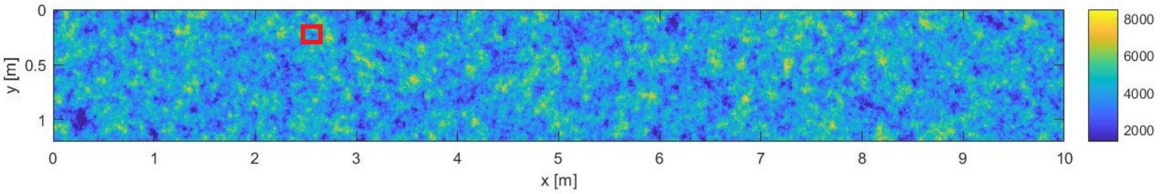

(a) Perturbed beam with $\Delta v = -150 m/s$ over an area of $10 mm^2$.

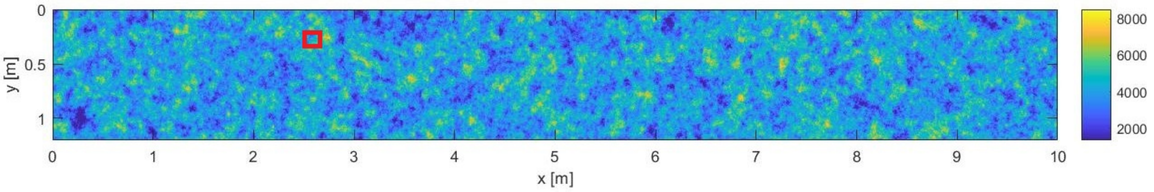

(b) Perturbed beam with $\Delta v = -1000 m/s$ over an area of $10 mm^2$.

Figure 3.22: Graphical representation of the simulated beams with respect to velocity field

discussed in detail in the coming sections.

Following the same scheme, a $\Delta v = +100 m/s$ within an area of $10 mm^2$ was implemented. Because of the faster signal, this composition led the perturbed wave to be ahead of the unperturbed. So, the stretching (compression) parameter resulted of opposite sign with respect to the previous slowing arrangements. Another elongated set of data was developed considering an area of $500 mm^2$, this time, increasing the relative velocity of $\Delta v = +3000 m/s$. Unfortunately, this resulted in an unstable wavefield propagation after reaching the area. Thus, due to the realisation limits of the simulation 3.2.1 [94], this analysis was not carried further. Both simulation are represented in Figure 3.23. Finally, a last set of data was studied. For what concerned the geometric disposition of velocity change, the entire $10000 mm$ x $1200 mm$ was considered. The variation was set to get a shortened signal at the bottom and a longer one at the top of the numerical beam, as shown in Figure 3.24. This arrangement was developed to have a study closer to the later discussed laboratory beam test in bending [36]. The velocity variation resulted in the well known compression area in the upper part and tension area in the lower part of the beam, considering the neutral axis to be in the middle. The characteristic of such a velocity change regarded a $\Delta v = +200 m/s$, at the top first layer, and $\Delta v = -200 m/s$, in the bottom last layer; for each of the 1200 millimetres of depth, there was a linear change of the velocity, resulting in a $\delta v = 0.33 m/s$ between two consecutive layers, each with a $1 mm$ depth. The Von Karman result is shown in Figure 3.24, although, computational requirements - dispersion related - did not allow the research to proceed in this direction.

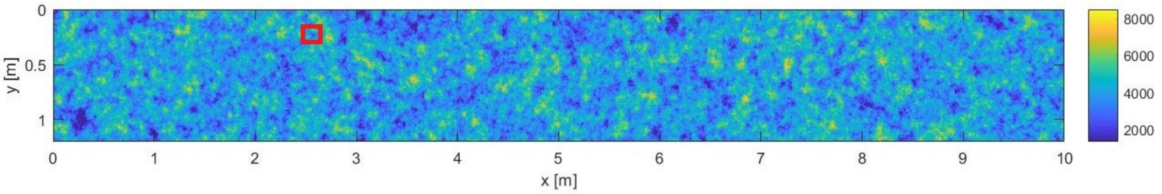

(a) Perturbed beam with $\Delta v = -100m/s$ within an area of $10mm^2$.

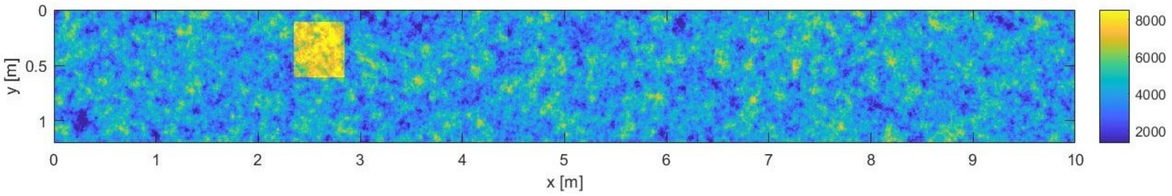

(b) Beam with a perturbed area of $500mm^2$ where $\Delta v = +3000m/s$.

Figure 3.23: Graphical representation of the simulated beams with respect to velocity field

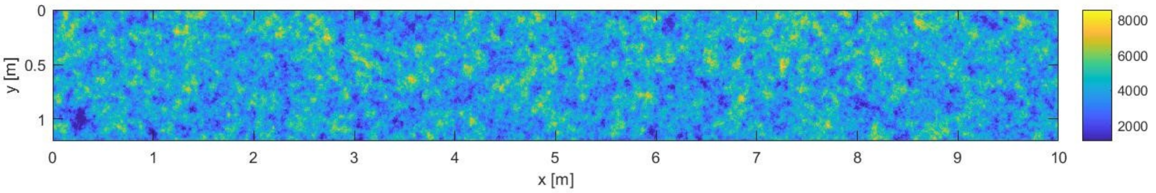

Figure 3.24: Beam entirely perturbed. From top layer, with $\Delta v = +200m/s$, to bottom one, characterised by $\Delta v = -200m/s$.

Time Window

An essential part of the stretching extraction path regards the time window selection. Several examples of window with respect to the dominant period were investigated: $t_{window} \approx 1.5T_{dominant} \div 11T_{dominant}$. In this study, $T_{dominant}$ equals $\frac{1}{88kHz} = 11\mu s$. Thus, a series of tests for two widths of $16\mu s$ and $121\mu s$, over the coda section, were performed. For completeness, two other analyses regarding as many time windows, of $\approx 400\mu s$ and $\approx 50\mu s$ length, were also considered. However, as later discussed, these led to not consistent output, thus, no further discussed. Considering the decay of amplitude and the absence of strong peaks, the starting time of coda wave was fixed at $\approx 1500\mu s$, not to consider any first-arrival wave. Hence, from that time instant on, a series of stretching tests were performed.

In order to understand which time opening would give the highest overall cross-correlation factor and to gain some redundancy, starting from $1587\mu s$ to $2484\mu s$, 57 windows were studied; each moving towards the end with a time step of $t_{step} = \frac{2500}{630}\,4 \approx 16\mu s$, with evaluation widths of $\approx 30\,\frac{2500}{630} \approx 120\mu s$ and $\approx 4\,\frac{2500}{630} = 16\mu s$. This way it was possible to extract 57 values, for each specific pair of source receiver, with respect to each velocity variation area set up.

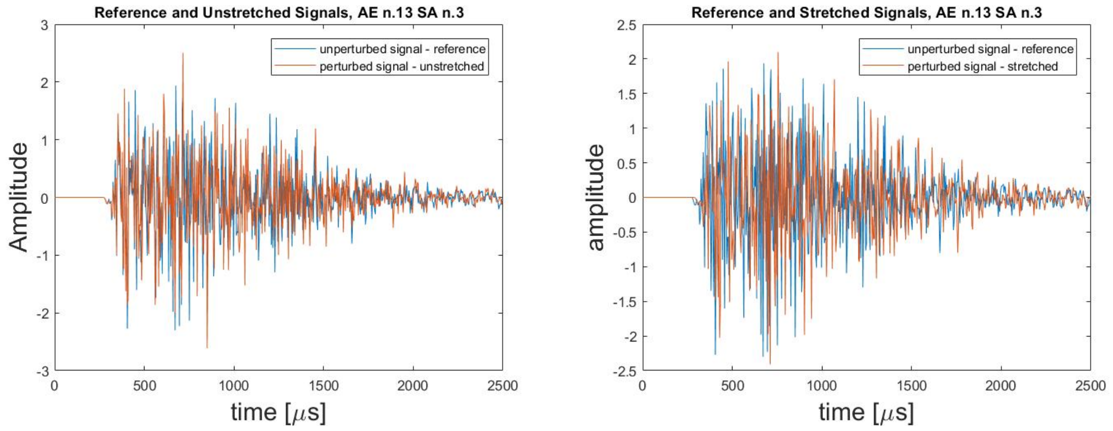

Figure 3.25: Perturbed and unperturbed signals, stretched and non-stretched with highlighted different windows. For pair AE13-SA3.

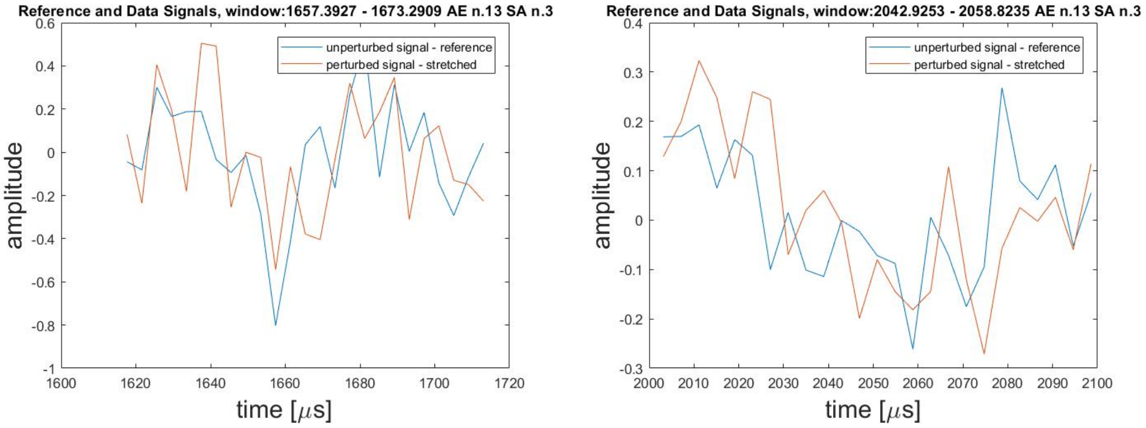

Figure 3.26: Zoomed window of analysis for $\Delta t = 1659\mu s - 1675\mu s$ (left) and for $\Delta t = 2042\mu s - 2058\mu s$ (right), perturbed/stretched and unperturbed (pair AE13-SA3).

Described in the following section, the Kernel changes as a function of the central time chosen in this step. Therefore, the study had the potentiality to study all 57 different Sensitivity values (i.e. Kernels - from section 3.3) which would have resulted, in combination to the corresponding 57 extracted ϵ factors, in a unique and redundant final dv/v parameter for each specific couple of source-receiver. In the end, due to computational timing and practical feasibility, only a few windows were taken into account (although this approach gets issued at the chapter end). In the previous Figures (3.25 and 3.26), the behaviour and the stretching amplitude of ϵ is affected by the chosen time window as well as by the setting of the velocity variation.

From the several ϵ that can maximise the correlation coefficient, values from -1 to +1, with a step size of 1x10^{-5}, were considered. Among the overall stretching parameters, some of them resulted to be equal to 0. This resulted from the computational limit: the request of a parameter, so small, to be lower than the step, thus gaining $\epsilon = 0$. From the theoretical discussion of section 2.2.3, only a parameter different than zero must be considered. For this reason, the time steps of $t_{central} = 1667\mu s$, $t_{central} = 2064\mu s$ and $t_{central} = 2381\mu s$ were taken as the main ones with a time window of $16\mu s$ and $120\mu s$, as well as an additional window, in $t_{central} = 2063\mu s$, either $16\mu s$ and $793\mu s$ wide.

For the present research, the main goal aimed at entirely identifying a correct stress distribution inside the medium under study, therefore, no synthetic analysis considering the Decorrelation Coefficient shall be discussed further. Moreover, the nature of the numerical simulation places the presence of openings and micro-cracks in front of very delicate choices, which does not necessarily fit with the one developed in the current study. Nevertheless, it is important to recognise how powerful such hypothesis can be and, if properly used in combination with the **CWI**, how it might be able to take the Structural Health Monitoring possibilities to an even higher level.

Stretching Parameters extracted

For what concerns the output, usually, the observed velocity variation factor is referred to as ϵ^{obs} and is defined as the "*apparent* relative velocity change" [70]. In similar analysis (*Lapse-time-dependent coda-wave depth sensitivity to local velocity perturbations in 3-D heterogeneous elastic media* by Obermann et al. [63]) the observed data are function of the depth and so, are divided into surface and body waves sensitivity. This definition, leads to the identification of a partition ratio α able to distinguish the time the wave has spent in each state during propagation.

In the present case, instead, there was no need to extract such specific combination, between body and surface waves, because of the simplistic assumption related to numerically propagate exclusively body waves, without any surface ones; moreover, among body-waves, only Primary ones were considered. This led ϵ^{obs} to become the main and only value to be considered during the *inversion technique*.

As possible to see from the tables presented in appendix A, all the ϵ values extracted

Table 3.2: Stretching parameters and Correlation Coefficients for a time window centred in $t_{central} = 1667\mu s$ with length $16\mu s$. The chosen colours correspond to: green, when $CC > 80\%$; yellow, when $50\% < CC < 80\%$ and red, if $CC < 50\%$.

	Window = $1559\mu s$ - $1675\mu s$									
	Epsilon					**Correlation**				
	SA1	**SA2**	**SA3**	**SA4**	**SA5**	**SA1**	**SA2**	**SA3**	**SA4**	**SA5**
AE1	-2,70E-03	8,00E-03	-9,00E-04	1,00E-04	-6,30E-03	0,892559	0,915061	0,854807	0,996579	0,712257
AE2	-3,55E-03	-4,20E-03	-5,50E-04	-5,55E-03	-6,55E-03	0,921464	0,830828	0,981819	0,989782	0,79028
AE3	8,10E-03	-4,00E-04	1,00E-04	-3,00E-04	-3,50E-03	0,95741	0,874804	0,738653	0,977755	0,790295
AE4	-9,00E-04	6,50E-04	-9,15E-03	4,65E-03	-1,30E-03	0,84145	0,841145	0,914296	0,703538	0,987515
AE5	-6,45E-03	-9,00E-04	4,55E-03	-6,50E-04	-1,30E-03	0,89193	0,869643	0,914786	0,86069	0,997342
AE6	7,70E-03	3,00E-04	1,00E-02	5,10E-03	-5,95E-03	0,922471	0,954112	0,850072	0,861755	0,833228
AE7	-1,85E-03	-3,80E-03	-7,70E-03	3,00E-04	-5,60E-03	0,799	0,81953	0,712205	0,954102	0,874405
AE8	1,00E-03	-1,00E-02	-9,50E-04	-5,70E-03	-1,55E-03	0,845457	0,871767	0,809108	0,924605	0,999256
AE9	-5,50E-03	4,00E-03	-5,45E-03	4,15E-03	6,10E-03	0,919386	0,752225	0,643964	0,909422	0,856204
AE10	-1,50E-03	-6,15E-03	7,15E-03	-4,80E-03	-7,50E-04	0,694648	0,474594	0,933326	0,783912	0,818378
AE11	-8,50E-03	6,40E-03	-9,40E-03	-4,70E-03	9,55E-03	0,799446	0,781738	0,634742	0,93756	0,987954
AE12	5,20E-03	5,35E-03	-1,50E-04	-3,80E-03	-1,00E-02	0,816363	0,993284	0,790802	0,663485	0,696894
AE13	-1,05E-03	6,20E-03	-5,90E-03	-8,00E-04	3,40E-03	0,848649	0,937314	0,990426	0,860603	0,986068

for longer windows provided quite low correlation coefficients. That is the main reason why the research moved its focus towards smaller time windows, with considerably higher interrelationship factors.

Table 3.2, depicts the stretching parameter and corresponding correlation coefficients (by use of a colour map), for every source-receiver couple, with respect to the previously mentioned $t_{central} = 1667\mu s$ window. For completeness, tables A.3, A.4 and A.5 are reported for $t_{central} = 2050\mu s$, $t_{central} = 2381\mu s$ and $t_{central} = 2063\mu s$ in appendix A.

Figures[11] 3.27 and 3.28 graphically represent all the extracted ϵ values with respect to every pair of source-receiver with the highlighted area of synthetic velocity variation. In red positive ϵ, representing areas under compression, and in blue negative values for tension zones. However, it became complex to directly interpret such images. In fact, at this point of the research, although of fundamental importance, the obtained values were not accurate for defining the areas through which the wave scattered, while detecting the perturbation. The next section (3.3) describes the practical application of this expansion.

---

[11] Graphic description derived from MATLAB code written by F. Zhang.

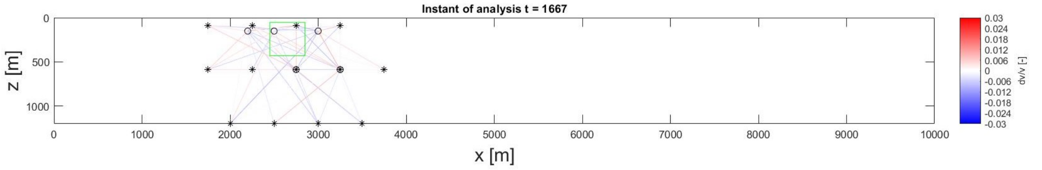

(a) Detail for $t_{central} = 1667 \mu s$.

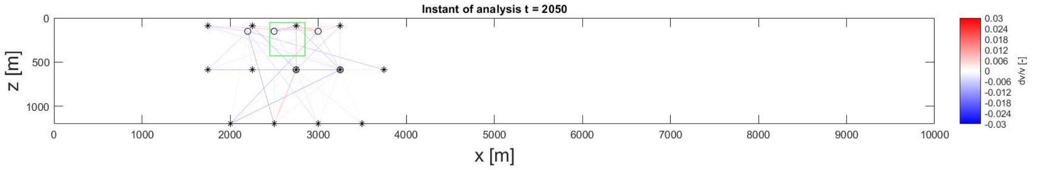

(b) Detail for $t_{central} = 2050 \mu s$.

Figure 3.27: All the ϵ values in the specific connection line between sources AE, presented as $*$, and receivers SA, shown as o.

3.3 Sensitivity Kernel

As above-mentioned, the formulation of the sensitivity kernel plays an essential role in the inversion of the observed arrival-time changes. Contrary to time-of-flight, changes in the coda can be attributed to velocity changes at specific locations in the medium, with respect to a specific possibility; i.e. the probability of a change, related to specific source-receiver couple, is proportionally higher to the proximity of the area to the couple. Consequently, associated with a specific set of source-receiver pair, the velocity variation obtains the most probable spatial distribution of dv/v in the medium. This spatial assessment of velocity changes needs to be converted into a spatial distribution of stress changes, which is the final objective of this study.

3.3.1 Numerical Simulation of the Kernel

In this section, we compare the theoretical sensitivity kernels (expression 2.19) to numerically computed sensitivity kernels. The latter can be defined from the numerical simulations, performed by means of the fdelmodc code. Figure 3.29 presents the intensity of the wavefield, at $t = 1667 \mu s$.

Figure 3.30 presents the intensity as a function of x (at $y = 0.613m$) and y (at $x = 3.400m$); the considered cross-sections are not positioned at the source location, highlighting, therefore, the correlation between source and another generic position. Despite some fluctuations, the intensity peaks appeared at the x and y source location,

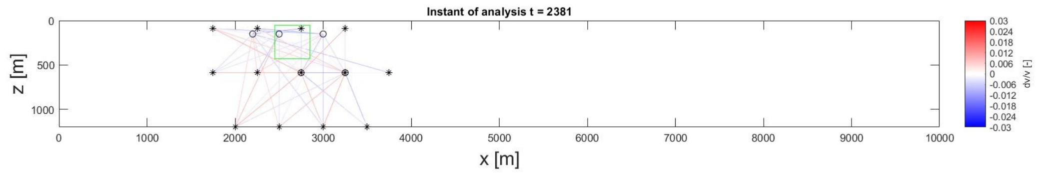

(a) Detail for $t_{central} = 2381\mu s$.

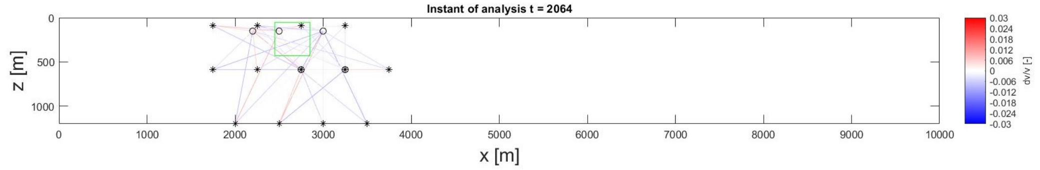

(b) Detail for $t_{central} = 2064\mu s$.

Figure 3.28: All the ϵ values in the specific connection line between sources AE, presented as $*$, and receivers SA, shown as o.

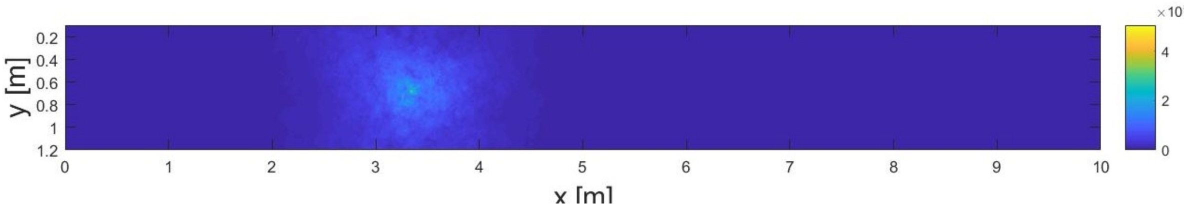

Figure 3.29: Intensity at time instant $t = 1667\mu s$. This example was derived with Smart Aggregate n.6 as only source.

respectively.

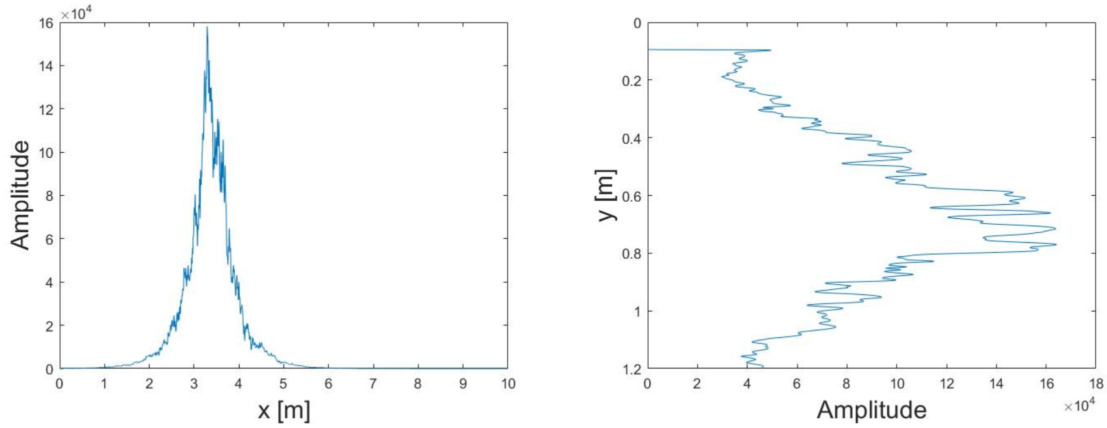

Figure 3.30: Horizontal (top) and vertical (bottom) energy lines of a receiver placed at $x = 3400mm$ and $y = 613mm$.

In order to compute the numerical sensitivity kernel, the same procedure was applied for a source placed in the same position as Acoustic Emitter n. 13 (Figure 3.31). Convolving the two intensities, shown in Figures 3.29 and 3.31, according to equations 2.15 and 2.23, and dividing by the source-receiver intensity at time t (see equations 2.15 and 2.23), we obtained the synthetic kernel depicted in Figure 3.32.

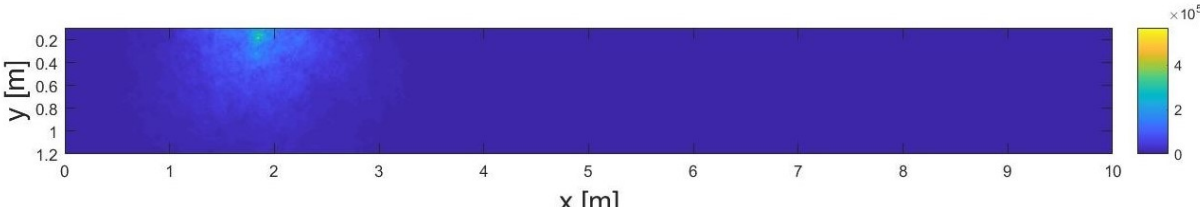

Figure 3.31: Numerical simulation of energy spreading at time instant $t = 1667\mu s$. Acoustic Emitter n.13 as source.

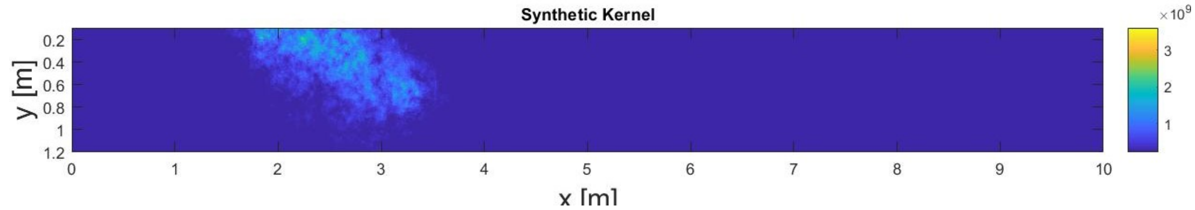

Figure 3.32: Numerical simulation of energy spreading from Acoustic Emitter n.13 to receiver Smart Aggregate n.1 at time instant $t = 1667\mu s$.

For the sake of completeness, we computed the theoretical kernels using both the 2D solutions to the time-dependent Boltzmann equation (i.e. radiative transfer and diffusion equation). These kernels are presented in Figure 3.33**a** and 3.33**b**, respectively.

The two approximations[12] presented a similar distribution of probability with the simulated one, provided that the energy distribution can be considered in an analogous perspective. At the same time, however, such an allocation shows the limits of the diffusion approximation with respect to the more accurate radiative transfer kernel. The first one has a quite low overall magnitude with a strong peak at the position of the sensors, while the second kernel shows higher amplitude in a wider area.

Although the kernel, computed using the solution to the radiative transfer equation, appeared to be more appropriate, we continued to use also kernel definitions from diffusion intensity.

---

[12] Derived from a variation of MATLAB code by Dr. T. Planès and Dr. A. Obermann

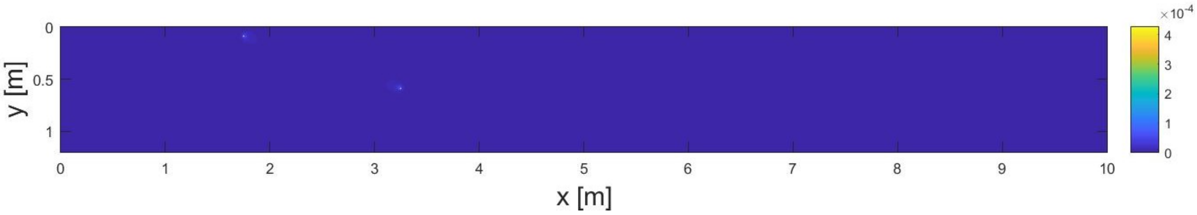

(a) Graphical representation of sensitivity kernel at time instant $t = 1667\mu s$ by means of equation 2.3.

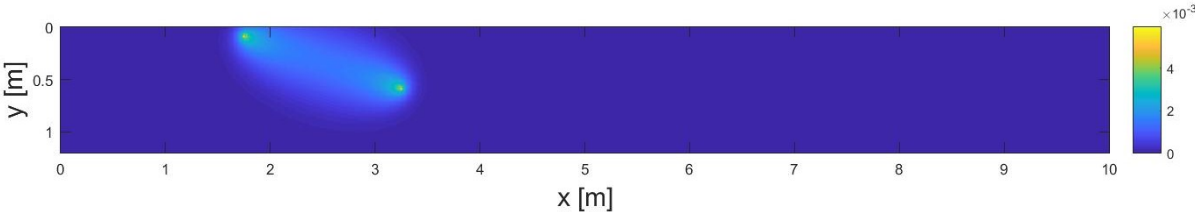

(b) Graphical representation of sensitivity kernel at time instant $t = 1667\mu s$ by means of equation 2.2.

3.3.2 Extracted Kernels

Among the various combinations of source-receiver pair (13 sources $* 5$ receivers $=$ 65 pairs), some were considered with great interest. To analytically define the kernel, the time interval to consider, between $t = 0$ and $t = t'$, was chosen with respect to the various windows, selected in the stretching chapter. Theoretically, all of this different sensitivity kernel formulations (i.e. function of distinct time intervals), combined with relative stretching parameters, would result in a unique velocity variation map of dv/v. Mesh plots of Figure 3.34 (and A.6, A.7) are just some of the ones obtained for each pair and windows under analysis.

At the beginning of the used code [62] [49], the diffusivity constant was extracted with respect to the following mathematical definition[13]

$$D = vl/2 \tag{3.14}$$

where v is the mean velocity inside the medium ($v = 4000m/s$) and l represents the scattering mean free path. Sometimes, in the literature this l factor gets specified rather than the diffusivity; actually, because of relation 3.14, this procedural difference is unim-

---

[13] A more comprehensive relation between D and l is given by Turner and Anugonda [95] with respect to the ratios of transport mean free path and of wave speed in the averaged element. However, adhering to literature, this variation was discarded in favour of the here mentioned equation 3.14 for a '*two-phase material*'.

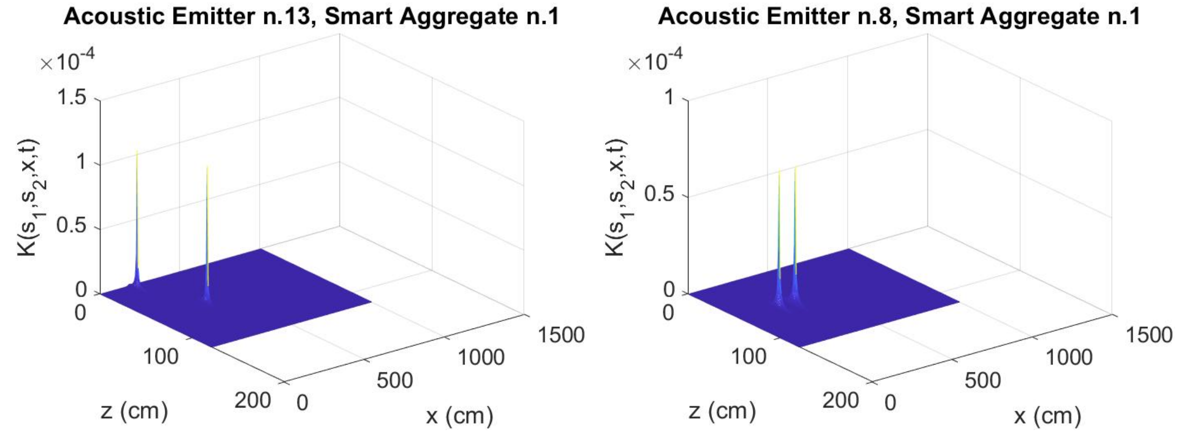

(a) pair: AE13-SA1 **(b)** pair: AE8-SA1

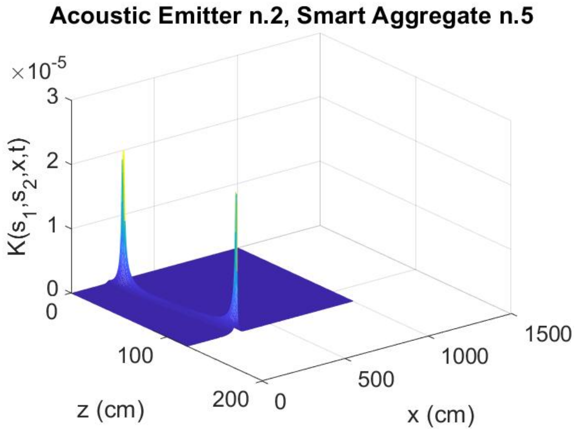

(c) pair: AE2-SA5

Figure 3.34: Three different pair combinations of sensitivity kernel for $t_{central} = 2050\mu s$.

portant.

The extensive inspection of the diffusivity, performed in paragraph 3.1.3, was based on the transport mean free path. Substantial is the reasoning, present in "*Depth sensitivity of seismic coda waves to velocity perturbations in an elastic heterogeneous medium*" [62], where the **scattering** mean free path is distinguished from the **transport** mean free path: l is "*the typical length scale after which a beam with a given propagation direction has been significantly attenuated by scattering*" [62]; while l^* represents "*the distance after which the 'memory' of the initial direction of the beam is lost*" [62]. Their relation is presented by equation 3.15 with respect to the scattering angle Θ.

$$l = l^*(1 - \langle cos(\Theta) \rangle) \tag{3.15}$$

where $\langle cos(\Theta)\rangle$ represents the cosine *directional average* [79] [66]. However, in the present case, l coincides with l^*, because scattering can be considered **isotropic** (i.e. "*inhomoegeneities scatter equal amounts of energy in all directions*" [62])

3.4 Simulation Output: Velocity Plot

The final step consisted in the application of the inversion procedure, to define the graphical velocity distribution, with respect to the several pairs of source-receiver for all 65 sensors. The entire 2D medium was studied, although only the area in between the sensors was reliable for the extraction of velocity changes; the areal extension gets further discussed at the end of Appendix A. In order to give an impression of what the simulation is expected to be, Figure 3.35 represents the one velocity map likely to appear.

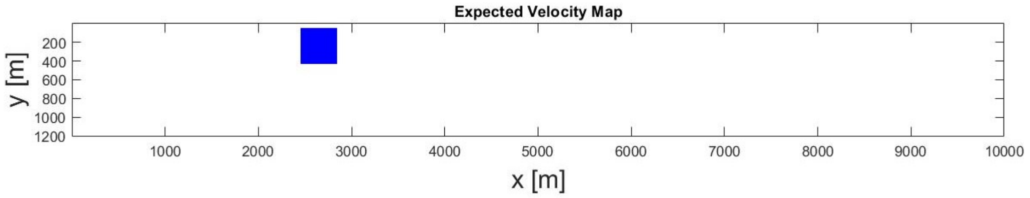

Figure 3.35: Expected Velocity Map (the variation amplitude shall not be considered).

Figure 3.36 presents the final output of what can be obtained from the CWI methodology. This process allows to exploit the information, gained in the stretching step, in order to get a more coherent set of information. This concept comes from the notion at the base of the relationship between the apparent relative velocity change and the sensitivity kernel. For every specific instant of analysis, theoretically, the same map should be gained.

Even though the images do not show perfect velocity variation fields, they provide continuous graphs to the stretching plots of Figures 3.27 and 3.28. Accordingly to the graphical representation of the stretching parameters, the red-blue colormap stated the areas in compression and in tension: red zones represented the part where velocity increases, while blue areas showed the decrease of velocity (i.e. the one numerically applied and investigated throughout the research).

Velocity maps of Figure 3.37, obtained from the radiative transfer definition of Intensity, have higher values of sensitivity kernel, which influenced the stretching parameters expansion over the medium. However, it can be stated that Figure 3.37 is almost equivalent to Figure 3.36: the information extracted using the CWI procedure presented a

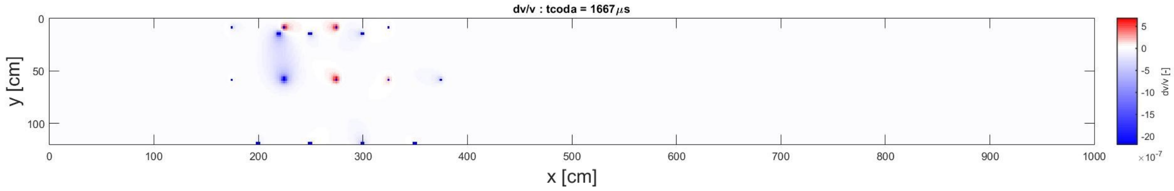

(a) Velocity plot for $t_{central} = 1667\mu s$.

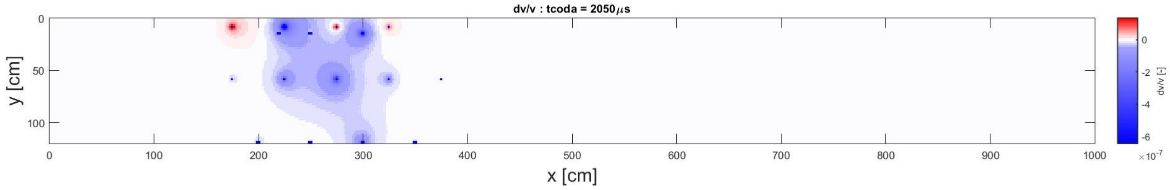

(b) Velocity plot for $t_{central} = 2050\mu s$.

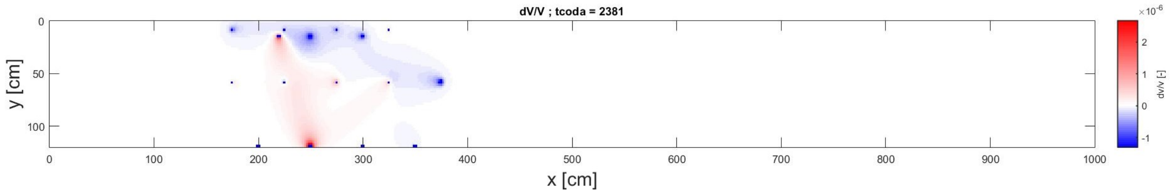

(c) Velocity plot for $t_{central} = 2381\mu s$.

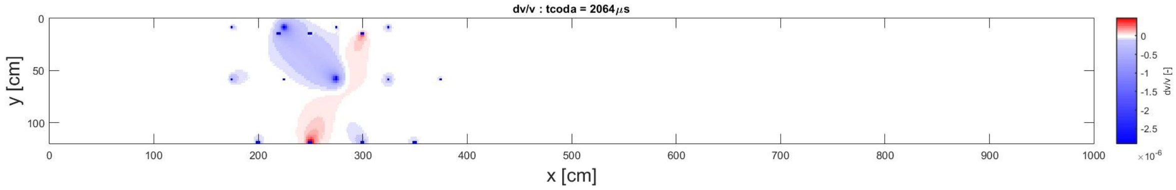

(d) Velocity plot for $t_{central} = 2064\mu s$.

Figure 3.36: Four different combinations of velocity maps, where the kernel has been obtained from the diffusion solution of equation 2.3

relatively analogous data, nevertheless, further investigation on this differences shall be questioned.

Velocity plot 3.36b, related to the diffusive formulation of the sensitivity kernel, showed an incoherent expansion derived from an unreliable stretching phase. For what concerned the radiative transfer definition of the kernel, instead, the same incorrect stretching parameters got correctly weighted out. Figure 3.37b, in fact, presented only negative values, detecting the applied synthetic decrease of velocity change. To explain this, it should be specified that the stretching step is independent from the kernel computation; therefore, once obtained the wrong apparent velocity changes ϵ, both versions of the sensitivity kernel had to deal with this mistake. However, the different nature of the kernels, derived from the two distinct 2D solutions of the Boltzmann equation,

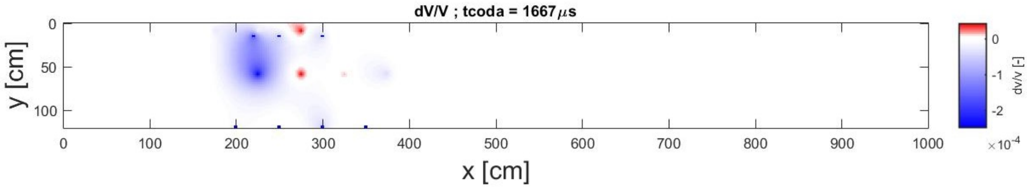

(a) Velocity plot for $t_{central} = 1667\mu s$.

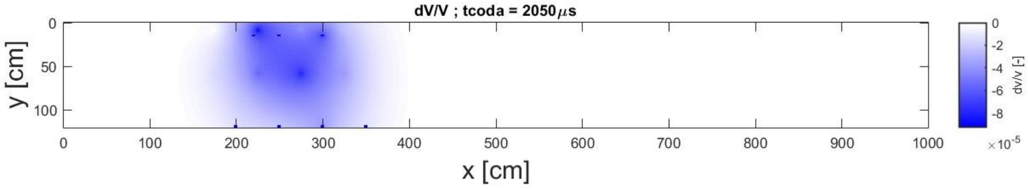

(b) Velocity plot for $t_{central} = 2050\mu s$.

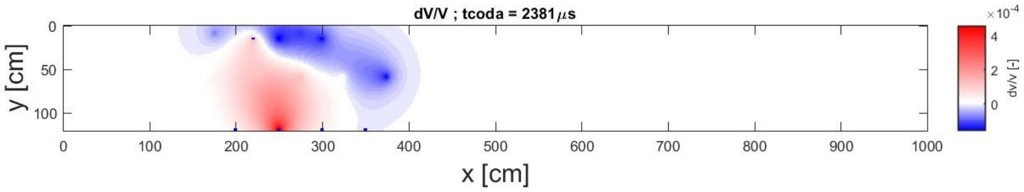

(c) Velocity plot for $t_{central} = 2381\mu s$.

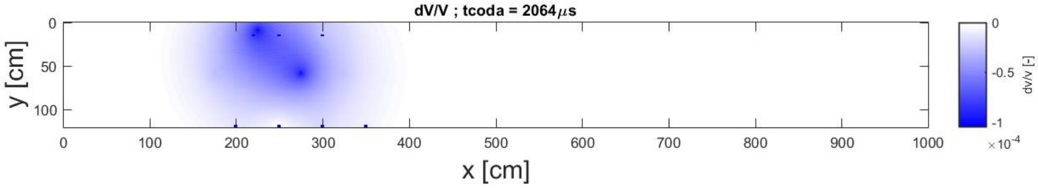

(d) Velocity plot for $t_{central} = 2064\mu s$.

Figure 3.37: Four different combinations of velocity maps obtained with respect to the radiative transfer definition of intensity from equation 2.2

determined a diverse stress map.

3.4.1 Discussion

Between the obtained outcomes and the starting simulated configuration, it was possible to underline some extent of sensibility and reliability regarding the CWI technique. With respect to Figure 3.21b, which indicates the actual perturbed medium, maps in Figures 3.36 and 3.37 are capable of identifying an analogous variation.

Except for Figure 3.36c, which presented a substantial incoherence with the numerically applied change of velocity, all the other field reproductions resulted in more reliable analyses. The reason of such a discrepancy might lie in the small time interval of study.

The short width of the window was considered as a result to the high corresponding correlation coefficient, which is the practical reliability index of the extracted ϵ. Although related to high CC, the apparent relative velocity changes were inconsistent to the expected output, detecting an increase of velocity (red fields in Figures) rather than the virtual applied decrease. This behaviour might be caused by the possible variations, observed from the signal, caused by the particular scatterer influence in the specific window under study.

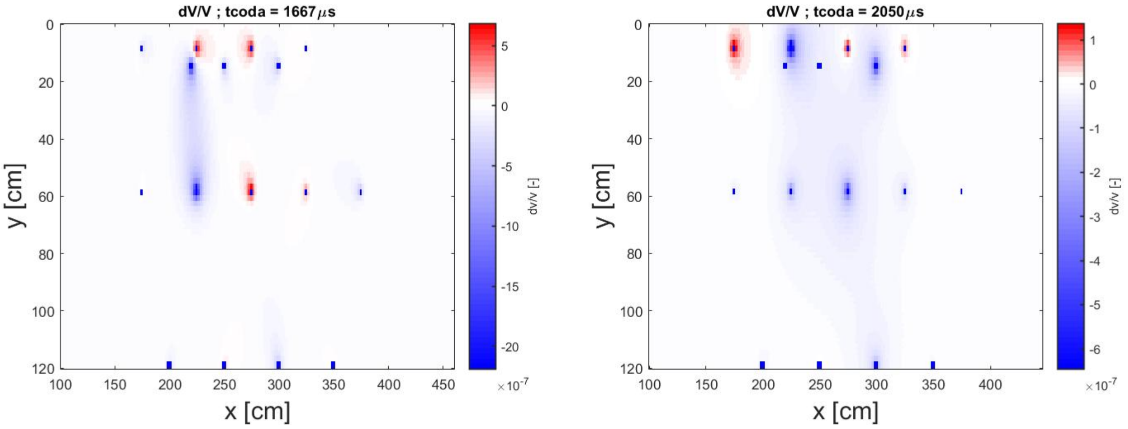

(a) Zoomed velocity field at $t_{central} = 1667\mu s$ **(b)** Zoomed velocity field at $t_{central} = 2050\mu s$

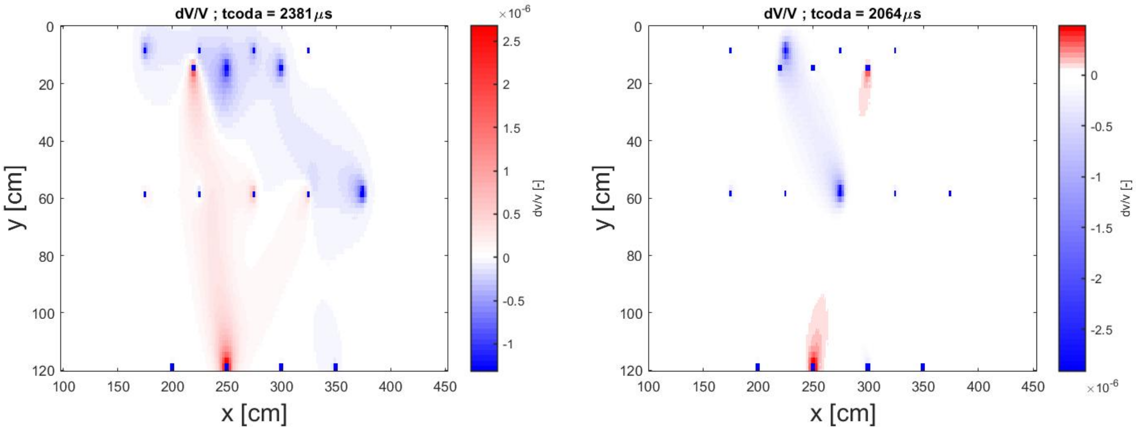

(c) Zoomed velocity field at $t_{central} = 2381\mu s$ **(d)** Zoomed velocity field at $t_{central} = 2064\mu s$

Figure 3.38: Detail on figure 3.36 sensors area where synthetic velocity change are

This methodology presents great improvement lines; nevertheless, Figures 3.36a, 3.36b, and 3.36d (detailed in Figure 3.38) highlighted an overall coherent detection of velocity, related to the virtually applied change. The magnitude was approximately constant for all the three applications; these plots presented a velocity variation in the range of ≈ 5 x 10^{-7} - ≈ 15 x 10^{-7}, so, it was not possible to extract an absolute observation from this magnitude. Knowing that a virtual change of $\Delta v = -150m/s$ was applied, we did not place sufficient resources to calibrate the test magnitude. The various Figures of this section displayed non defined numbers at the positions of the sensors. This was due to the numerical implementation limits which underlined, according to equation 2.32, an high kernel value at the denominator, causing an infinite[14] velocity variation.

Another inconsistency was located nearby the sensors position, where incongruous velocity increments were obtained as well. Such a biased evaluation was generated by some apparent velocity changes which, for the specific window, were not characterised by the best reliability index (i.e. correlation coefficient sufficiently high); then, because of the proximity to the sensor location, its overall weight increased during the inversion procedure, causing a substantial mistake in the output.

Because of unidentified errors of this type, the best approach, perhaps, may consist in applying the CWI for an extensive number of windows, all over the signal. The main role would still be driven by coda-waves, therefore the time windows selection should start after the peak. This would lead to the definition of several set, each of 65 apparent relative velocity changes. From these ϵ, a unique reliable mean should also be averaged, to be combined with a specific sensitivity kernel. Such an approach, however, may present substantial thoughts and evaluation issues concerning the correct definition of the kernel central time.

Stating a starting point for future works, the application of the above-mentioned path was advanced. The work regarded the definition of 57 ϵ_i for as many time windows. These temporal sections were $16\mu s$ wide, to keep a reliable correlation coefficient, advancing from $1587\mu s$ towards $2484\mu s$, with a time step of $16\mu s$. The graphical depiction of the apparent relative velocity variation factors is presented in Figure 3.39.

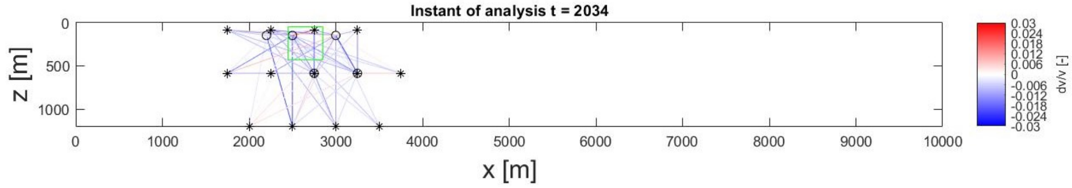

Figure 3.39: Stretched parameters at $t = 2035\mu s$

For what concerned the chosen sensitivity kernel, the undertaken choice issued the average probability. However, the computational limits led to assume the equivalence between the averaged kernel, from all 57 windows, with a single sensitivity kernel, defined

---

[14] the Matlab derivation generated a Not-a-Number value, showed in blue dots inside the beam

for the mean central time: $t_{central} = 2035\mu s$. Figure 3.40 presented the obtained velocity field of the beam, where the identification of the synthetic stressed area resulted coherent with the expected change.

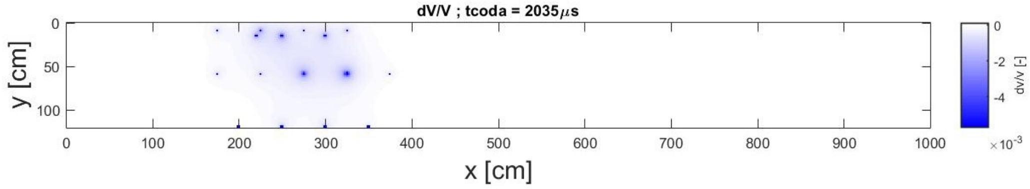

(a) Map gained from diffusive sensitivity kernel

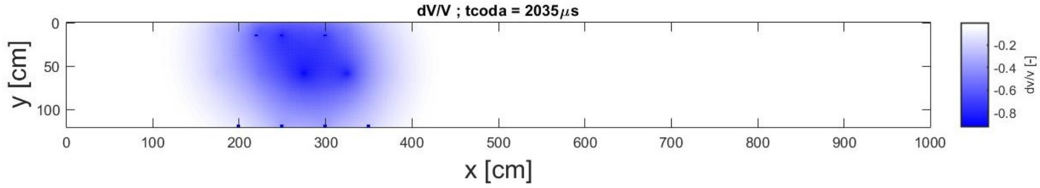

(b) Map gained from radiative sensitivity kernel

Figure 3.40: Velocity plots gained from averaged apparent relative velocity change ϵ, for $t_{central} = 2035\mu s$

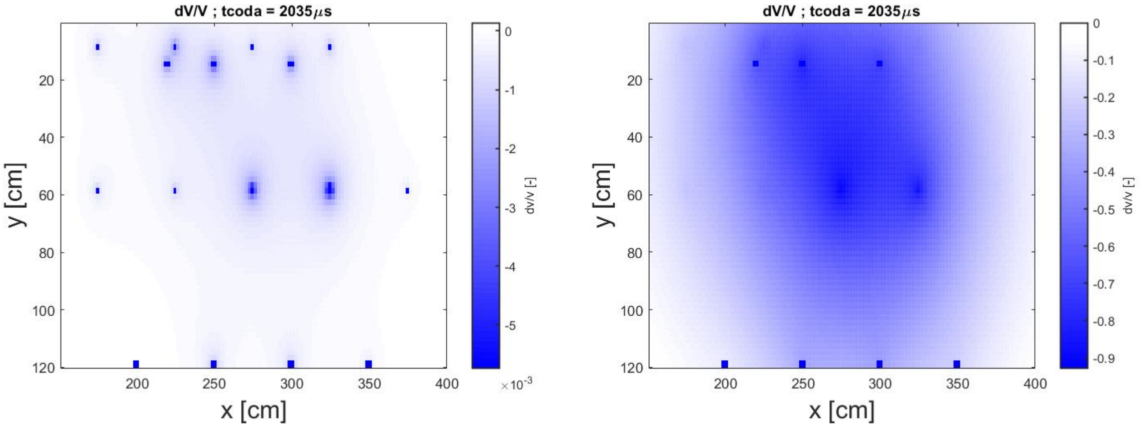

(a) Zoom of diffusive kernel analysis, figure 3.40a **(b)** Zoom of diffusive kernel analysis, figure 3.40b

Figure 3.41: Zoomed influence section from figure 3.40

Obviously, this choice was simply driven by an assumption regarding the central time of the kernel and the width of the time windows. Its proper guessing shall become fundamental with a view to next studies, aiming at gaining better explanations on either the sensitivity areas and the resulted amplitudes.

4

Laboratory Application

Once the premises and reasonings regarding Coda Wave Interferometry have been proved, according to the numerical simulation, the following step followed the extraction of useful practical information for a real test application[15]. The main goal of chapter 3, in fact, aimed at gaining some awareness on how this technique can be used for structural monitoring purposes, within a simulated error-less study environment. The following section presents the CWI application for a new data set.

The signals under consideration refer to a $1.2m$ high x $10m$ long x $0.3m$ wide concrete beam in bending, tested in controlled laboratory conditions at Delft University of Technology (already presented in section 3.1.4). The main difference with the precedent analysis resulted in a new arrangement of velocity variation. Actually, for the simulated study, the apparent change of wave speed was chosen as an area, with given values. Now, instead, the beam is loaded under specific steps and conditions, resulting in a different set up and consecutive expected outcomes inspection. Analogously to the synthetic application, the investigation focused on the detection of velocity changes, being related to the stress-state (i.e. *acoustoelastic effect*).

---

[15] The real test application has been developed in an analogous manner to what found in the literature [8] [48] [85].

Test Loading Scheme

The test was planned to investigate the beam in bending, according to different loading arrangements. The element was tested with respect to five load levels applied to the beam mid-span, and, for each one, three different load cycles were applied: firstly, a step by step loading of $10kN$ with consequent unloading condition; after that, an impulse-like followed by a final sustained loading application. The five levels were in between $100kN$ and $300kN$, with a constant loading step of $50kN$ in between [43].

For what concerned the CWI application, the perturbed data to be analysed belonged to the second load cycle (i.e. loading scheme of $150kN$). The driving reason was centred in obtaining an important applied load arrangement, while avoiding any possible cracking phenomenon inside the medium. The unloaded signals were, obviously, extracted before the application of any loading arrangement.

Practical Implementation

The geometry configurations and all various beam settings were identical to the synthetic ones (disclosed in Figure 3.15). The sources consisted of 13 *Acoustic Emitters* (**AE**), capable of sending a perturbing wave impulse of $f_{central} = 88kHz$. The 5 *Smart Aggregates* [101], instead, covered the role of both the sources as well as the receivers.

The Smart Aggregates (**SA**), employed for this analysis, consisted of a cylindrical element with diameter of $25mm$ and height of $20mm$, made out of two thick layers of marble and a piezoelectric sheet in between; however, different configurations have been developed for other analysis (Figure 4.1) [27] [43] [85]. The basic idea features the SA to be embedded within the concrete element during the initial casting procedure. For this laboratory application, only a few were actually embedded in concrete while an important number were simply gel-attached to the surface [43].

This premises highlight how the CWI technique can be easily exploited by means of Smart Aggregates in practical situations (section 1.3). Furthermore, in addition to the fact that an embedded sensors disposition might lead to better data gaining, it would also present a limited application to only new structures; nonetheless, it allows proper signal evaluation also when gel-attached at the surface. Therefore, it proves the methodology to have reliability and adaptability for existent elements as well.

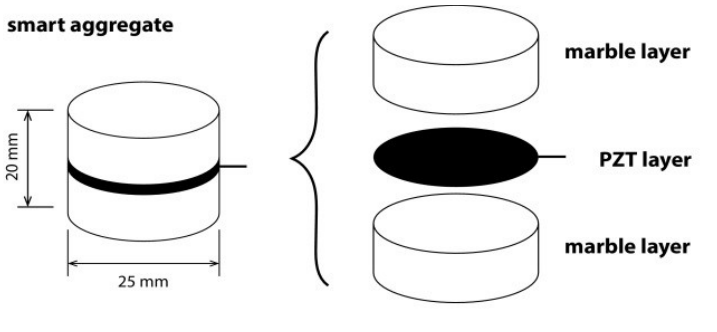

(a) Smart Aggregate composition layout used for the real test application [43].

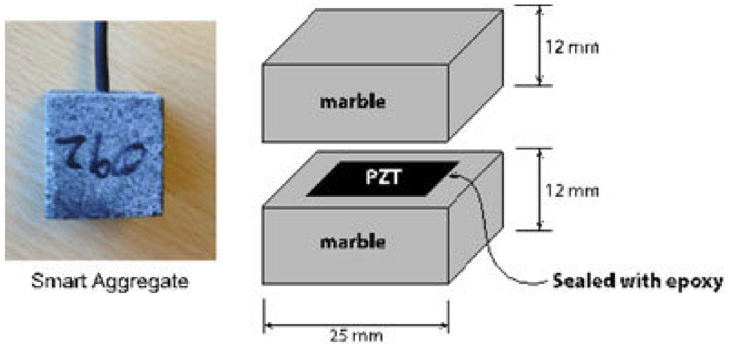

(b) Smart Aggregate image (left) and its schematic composition (right) [27].

Figure 4.1: Two Smart Aggregate representations

4.1 Working Arrangement

The followed workflow proceeded in parallel to the one previously implemented (chapter 3). Starting from the above mentioned lab-data set, the extraction of diffusivity constant, absorption time, and wave propagation velocity was avoided because already defined. The numerical simulation of concrete and relative properties were actually driven by the real signals themselves, as specified in paragraph 3.1.4.

This CWI working arrangement started from the stretching phase which characterises ultimately and uniquely the element with respect to its loaded, perturbed data. The same sensitivity kernel evaluation, instead, was entirely reused. In fact, the identical geometry configuration of the test allowed to keep the antecedent evaluated probabilities (i.e. Kernels) for this new section of the research, although, they referred to different central instants of the window.

Finally, the inversion technique (of section 2.3.2) was thoroughly adopted in order to extract a more complete map of velocity variation, to be related, in a final moment, to the state of stress of the studied element.

4.1.1 Stretching

The lab-application began with the stretching procedure. The windows to be analysed consisted in four $t_{central}$ instants, wide $120\mu s$, $1914\mu s$, and $16\mu s$. Analogously to the reasoning of section 3.2, the first two lengths of time analysis did not extract consistent stretching ϵ values (reported for completeness in Appendix B), so their analysis were not developed into further steps: the correlation coefficients did not surpass a minimum threshold to be considered coherent. Therefore, only the shorter windows of $16\mu s$ are here reported, for the four central instants of study: $3060\mu s$, $3500\mu s$, $4060\mu s$ and $3957\mu s$.

Time Window

Because the real signal was defined up to $4.915ms$ (Figure 4.2), it was possible to extract more arrangements than the previous synthetic time windows. In fact, other than the four above-mentioned windows, 212 time sections were studied, with $16\mu s$ of width and central times in between $1507\mu s$ and $4899\mu s$, each with a spacing of $16\mu s$ with respect to their neighbour. These led to the definition of 212 apparent relative velocity changes; one for every pair of source-receiver. These data might have been used in correlation with as many sensitivity kernels, to gain a unique and redundant $\frac{dv}{v}$ factor for each cell composing the beam grid. However, numerical implementation limits forced the study to narrow the complete analysis to precise time windows.

Figure 4.2 represents both the perturbed and non-perturbed signal, before and after the stretching application. Figures 4.3 and 4.4, instead, show a detail on the specific windows of study.

Stretching Parameters extracted

The discussion on the 212 windows gets developed at the end of the chapter. The following digression refers to the four selected windows of analysis, which are reported in table 4.1, for $t_{central} = 3060\mu s$. Tables B.5, B.6 and B.7, referred to the other three windows, are reported in Appendix B. Analogously to the synthetic step, this choice was mainly driven by the implementation time on a side, as well as the presence of parameters equal to zero. The stretching factors varied in between -1 and $+1$, with a step size of $1 * 10^{-4}$. Apparently, some data were so similar, that they defined a stretching factor smaller than

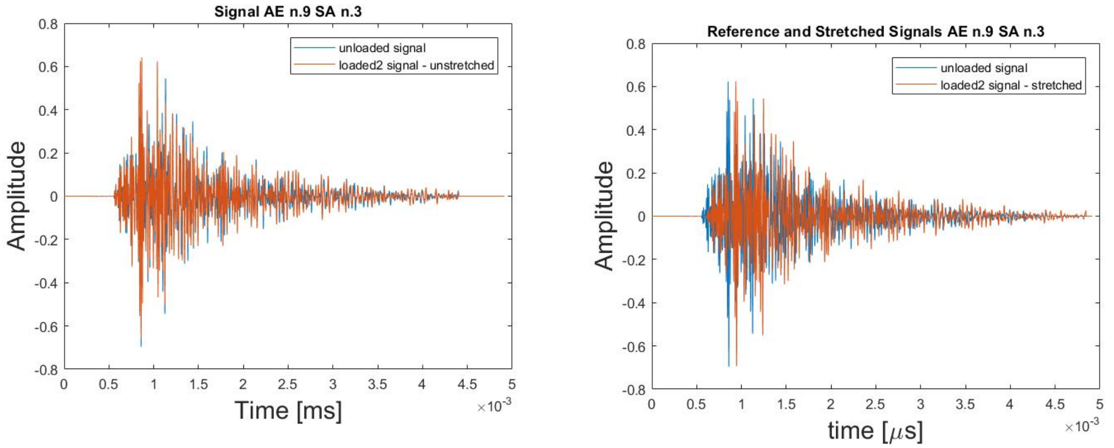

(a) Reference and non-stretched perturbed signals.

(b) Reference and stretched perturbed signals.

Figure 4.2: Configuration regarding Acoustic Emitter n.9 - Smart Aggregate n.3

the step magnitude, resulting in $\epsilon = 0$. The numbers presented for tables (4.1, B.5, B.6 and B.7) showed exclusively extracted data for $t_{central} = 3060\mu s$, $t_{central} = 3500\mu s$, $t_{central} = 4060\mu s$ and $t_{central} = 3957\mu s$ as central window time, each with length of $16\mu s$.

Table 4.1: Stretching parameters and Correlation Coefficients for real data set with central time of the window $3060\mu s$, $16\mu s$ wide (colour settings analogous to table 3.2).

	Window = $3052\mu s$ - $3068\mu s$									
	Epsilon					**Correlation**				
	SA1	**SA2**	**SA3**	**SA4**	**SA5**	**SA1**	**SA2**	**SA3**	**SA4**	**SA5**
AE1	-1,60E-03	7,60E-03	-1,50E-03	-3,20E-03	-9,40E-03	9,93E-01	9,98E-01	9,97E-01	9,96E-01	9,94E-01
AE2	-6,60E-03	-8,20E-03	8,90E-03	-5,40E-03	5,10E-03	9,91E-01	9,97E-01	9,93E-01	7,19E-01	9,94E-01
AE3	9,10E-03	-3,00E-04	-1,10E-03	6,30E-03	-1,10E-03	9,99E-01	9,93E-01	9,14E-01	9,89E-01	9,91E-01
AE4	-2,00E-04	-1,70E-03	-1,10E-03	-9,40E-03	8,10E-03	9,80E-01	9,85E-01	1,00E+00	9,75E-01	9,94E-01
AE5	7,90E-03	-7,10E-03	-8,20E-03	-1,00E-02	-1,00E-03	9,92E-01	9,95E-01	9,99E-01	9,72E-01	9,58E-01
AE6	1,00E-02	4,70E-03	-1,00E-02	-7,00E-04	-8,10E-03	8,14E-01	9,68E-01	9,58E-01	9,85E-01	9,75E-01
AE7	-1,10E-03	-8,90E-03	1,40E-03	0,00E+00	-1,20E-03	4,12E-01	9,96E-01	9,63E-01	9,90E-01	9,98E-01
AE8	5,80E-03	9,10E-03	-5,00E-04	-3,00E-04	7,00E-03	9,96E-01	9,93E-01	9,90E-01	9,95E-01	9,95E-01
AE9	-1,30E-03	3,60E-03	5,00E-04	-1,00E-02	5,00E-04	9,95E-01	9,17E-01	9,65E-01	9,04E-01	9,93E-01
AE10	-9,00E-04	8,00E-04	-8,80E-03	-8,00E-03	-3,00E-04	9,84E-01	9,55E-01	9,73E-01	9,89E-01	9,90E-01
AE11	8,30E-03	8,50E-03	-3,80E-03	2,00E-03	1,70E-03	9,96E-01	9,88E-01	9,41E-01	9,61E-01	7,09E-01
AE12	-4,00E-03	-5,00E-04	-7,70E-03	-1,40E-03	6,00E-04	9,94E-01	9,93E-01	9,85E-01	9,99E-01	9,64E-01
AE13	1,00E-04	-9,80E-03	5,40E-03	-1,00E-03	5,50E-03	9,96E-01	9,90E-01	7,52E-01	9,97E-01	9,84E-01

Making a stop here would permit to describe the velocity variation in the connection line of SA-AE, as represented in Figures 4.5 and 4.6. Although this step already stresses useful information on the velocity variation, the research was driven by the compelling

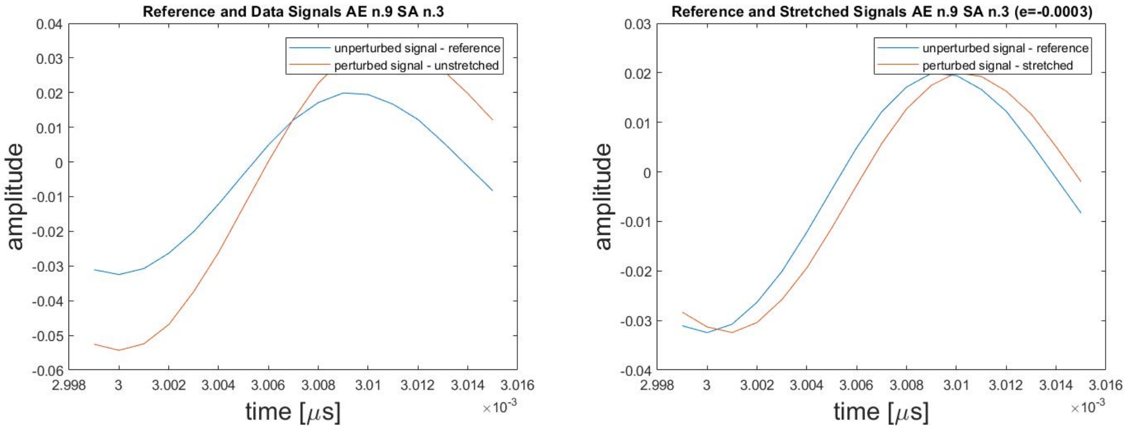

(a) Detail on the reference and non-stretched perturbed signals.

(b) Detail on the reference and stretched perturbed signals.

Figure 4.3: Analysis window of $t_{central} = 3000\mu s$ for pair Acoustic Emitter n.9 - Smart Aggregate n.3

opportunity of fully exploiting the CWI technique, in order to get a continuous and reliable stress map.

When comparing the 4.5 and 4.6 plots with Figure 4.7, a severe difference in the obtained stretching factors is visible. The reason of such variation is based on the part of the signal to be stretched. Indeed, Figure 4.7 considered the ballistic wave analysis at $t_{central} = 1500\mu s$, defining an immediate understanding of the graphical distribution of the ϵ parameters. On the contrary, Figures 4.5 and 4.6 presented a rather non intuitive plot. The coda parts of the signal had scattered and detected over a bigger area than the direct first arrival. Therefore, the graphical definition of ϵ resulted in a plot more difficult to interpret, with respect to the one in Figure 4.7, which presented positive stretching factors at the top and negative values at the bottom of the beam (i.e. respectively compression and tension, in accordance to the *acoustoelastic effect*).

4.1.2 Sensitivity Kernel

Connecting the strongly scattered stretched values with their actual scattering path was undertaken by the kernel definition. This is required to employ the basic statistical concept of wave propagation, from one point to another, during the inversion procedure. For the sensitivity kernel, the analogous geometries of the synthetic analysis gave the opportunity to use the same coding set up. The main difference was related to the central time to be considered. Different signals refer to different time windows, which, in

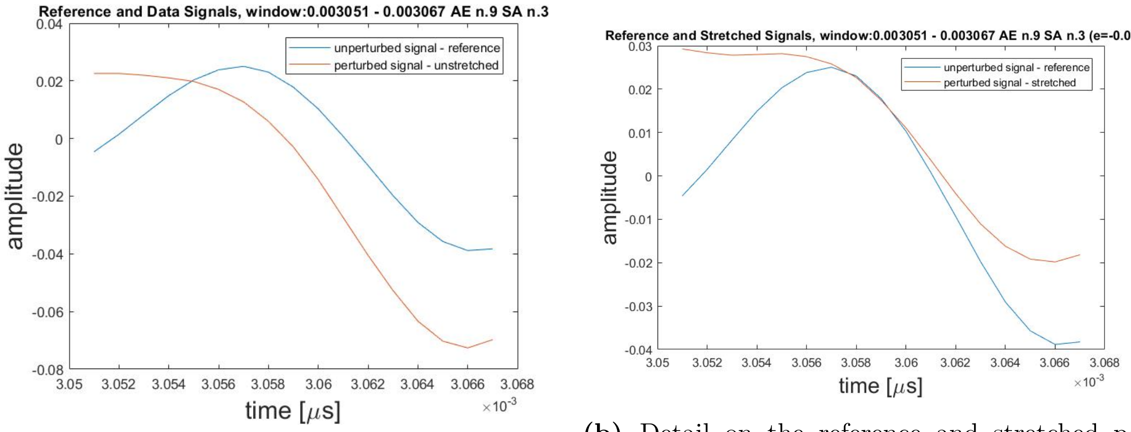

(a) Detail on the reference and non-stretched perturbed signals.

(b) Detail on the reference and stretched perturbed signals.

Figure 4.4: Analysis window of $t_{central} = 3060\mu s$ for pair Acoustic Emitter n.9 - Smart Aggregate n.3

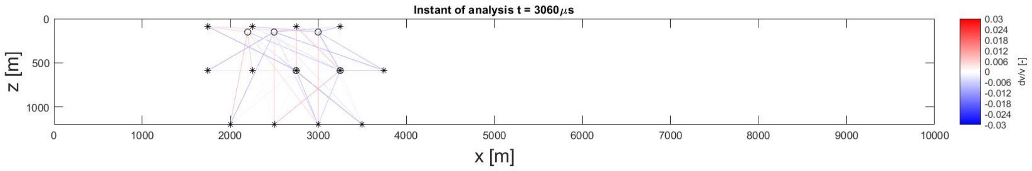

(a) Detail for $t_{central} = 3060\mu s$.

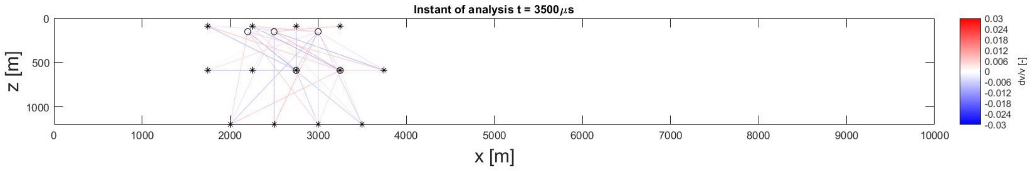

(b) Detail for $t_{central} = 3500\mu s$.

Figure 4.5: All the ϵ values in the specific connection line between sources AE, presented as $*$, and receivers SA, shown as o.

turn, are based on distinct $t_{central}$. Thus, distinct kernels were obtained according to the diffusivity approximation as well as the radiative transfer solution. The choice, analogous for the stretching parameters, consisted in selecting time instants of $t_{central} = 3060$, $t_{central} = 3500$, $t_{central} = 4060$, and $t_{central} = 3957$.

Among the several obtained figures for every source-receiver pair, a collection is exposed (in Figures 4.8, 4.9, B.5 and B.6), with respect to the different central times of study. Accordingly to the probability concept, previously discussed, the magnitude of

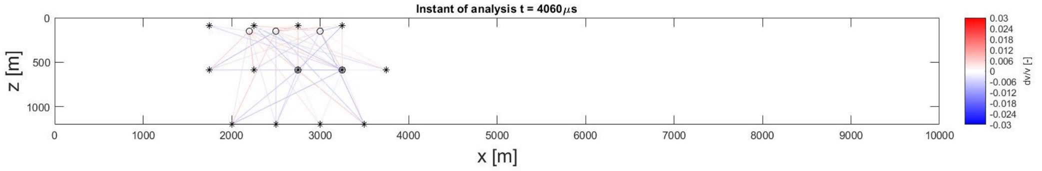

(a) Detail for $t_{central} = 4060\mu s$.

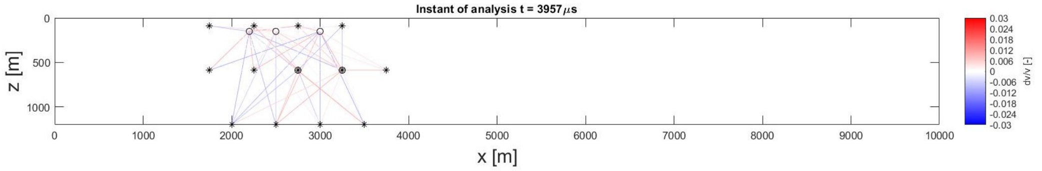

(b) Detail for $t_{central} = 3957\mu s$.

Figure 4.6: All the ϵ values in the specific connection line between sources AE, presented as $*$, and receivers SA, shown as o.

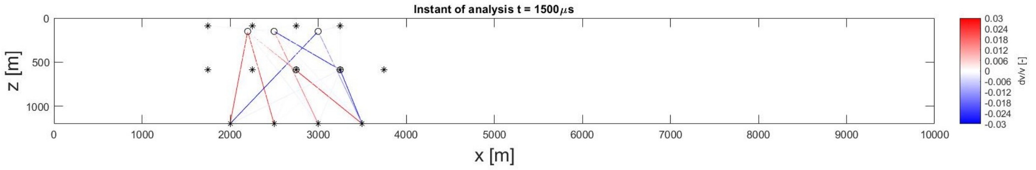

Figure 4.7: Graphical arrangement of ϵ values between SA and AE for $t_{central} = 1500\mu s$, with absence of horizontal stretching between sensors.

the kernel increases linearly with $t_{central}$.

4.2 Laboratory Test Output: Velocity Plot

Combining the obtained 65 apparent velocity variation values, with the kernel, made possible to derive the velocity plots of the real concrete beam in bending, under a load arrangement of $150kN$. The discretization frame of the beam was obtained with a grid of $10mm$ size in height as well as in width: 121121 cells of $1cm^2$ each, in an analogous manner to the one presented in the synthetic analysis. Although only a portion of grid cells were investigated, this configuration led to an ill-posed problem which was determined by means of the *Inversion technique* (chapter 2.3.2). Following the solution of equation 2.37, the obtained $\boldsymbol{m}$ vector is reported for every different time moments. According to the theoretical concept, all the obtained velocity plots should describe the very same situation resulting in a list of equivalent images.

Figure 4.10 show the derived velocity plots (i.e. equivalent to the stress distribution)

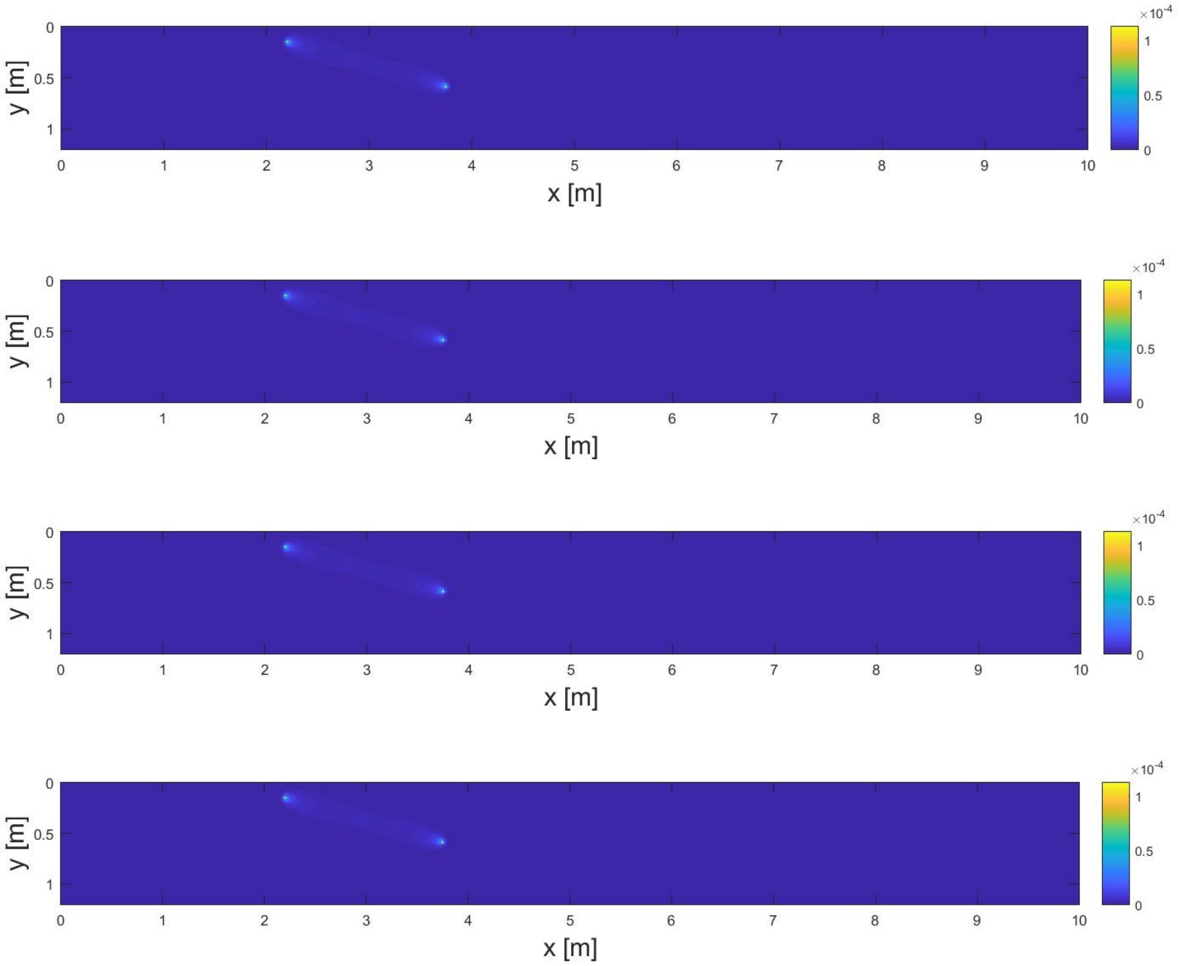

Figure 4.8: Surface representations of four kernels, for pair Acoustic Emitter n.5 - Smart Aggregate n.5. The different time instants are: $t_{central} = 3060\mu s$; $t_{central} = 3500\mu s$; $t_{central} = 4060\mu s$; and $t_{central} = 3957\mu s$

present inside the beam, at $150kN$ application. The Figures are directly related to the stretching parameters earlier presented in Figures 4.5 and 4.6. The red-blue colorbar allows to interpret areas in compression (i.e. increase of velocity) as well as in tension (i.e. velocity drop). Likewise the simulation outcomes, the coherent colour set gives continuity to the values presented in the stretching section 4.1.1.

Furthermore, to proceed in a comparable direction to the synthetic analysis, we defined also the four velocity plots obtained in accordance to the radiative transfer intensity formulation. Figure 4.11 shows the various final outcomes with respect to the more correct kernel expression; however, although characterised by a better velocity distribution, the various cells show comparable maps with the ones presented in Figure 4.10. Obtaining a

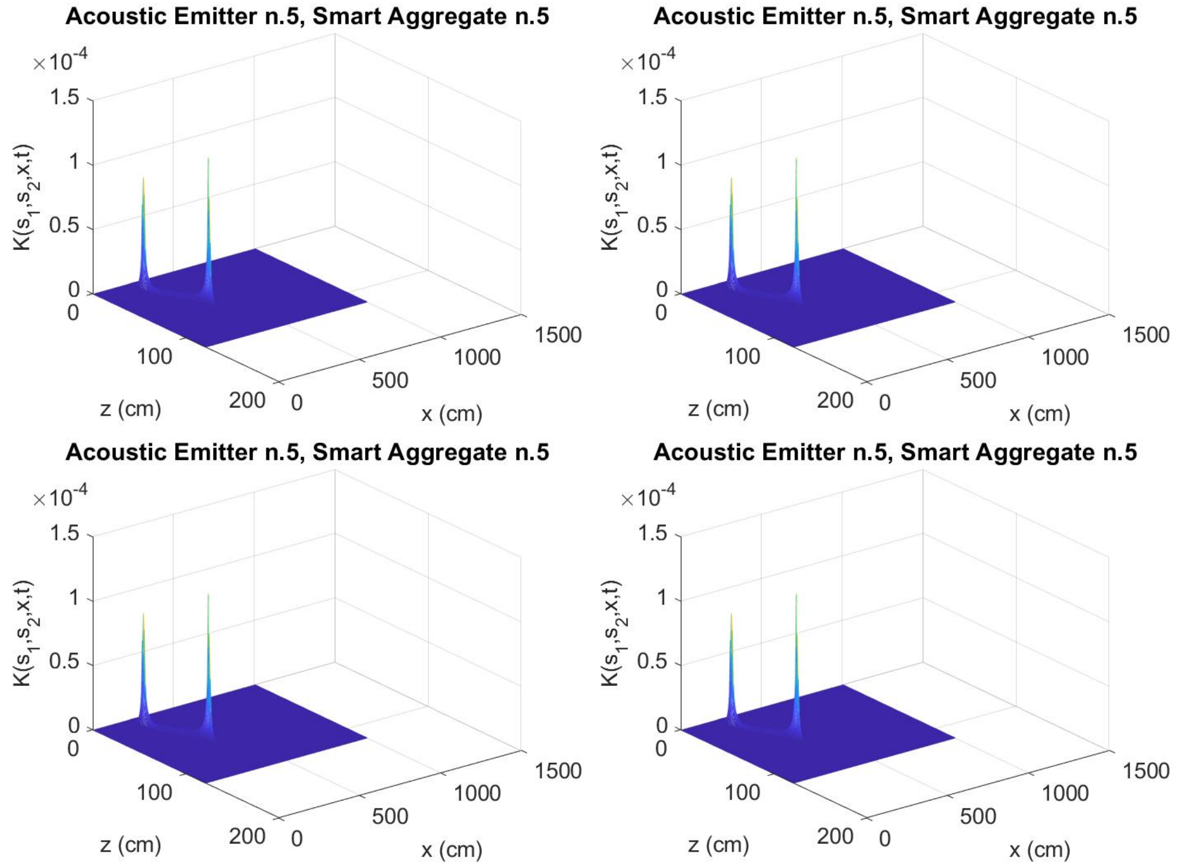

Figure 4.9: Mesh representations for pair Acoustic Emitter n.5 - Smart Aggregate n.5, of the kernels in Figure 4.8. The various time instants are: $t_{central} = 3060\mu s$ (top-left); $t_{central} = 3500\mu s$ (top-right); $t_{central} = 4060\mu s$ (bottom-left); and $t_{central} = 3957\mu s$ (bottom-right)

better understanding of the magnitude and the edge zones differences, between the two kernel formulations, nonetheless, remains a fundamental focus for future researches.

4.2.1 Discussion

It is not straightforward to state whether or not the precedent images are correct. It was possible to assume the stress distribution inside the medium, due to the controlled environment of the test. It consisted of a compression part on the top, thus increase of velocity (in red), and a tension part at the bottom, equivalent to a velocity drop (blue). The details of Figure 4.12 allow to further inspect the output coherence with the theoretical definition. The obtained plots 4.10b and 4.10c resulted to be, to some extent, in accordance with the predicted theoretical stress distribution, involving a beam in bending [36]. However, erroneous distributions were still present in all the four graphs.

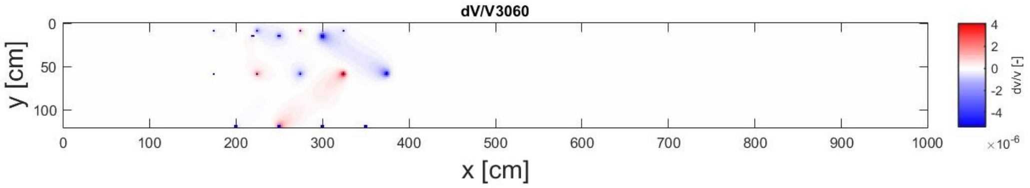

(a) Velocity plot for $t_{central} = 3060\mu s$.

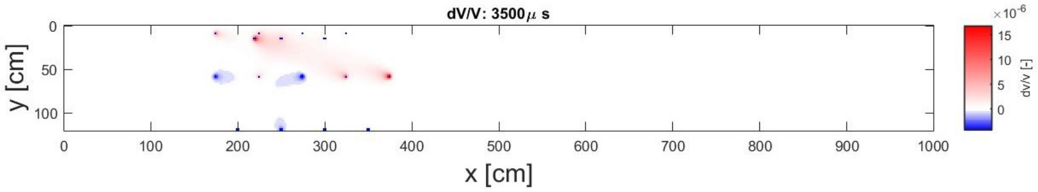

(b) Velocity plot for $t_{central} = 3500\mu s$.

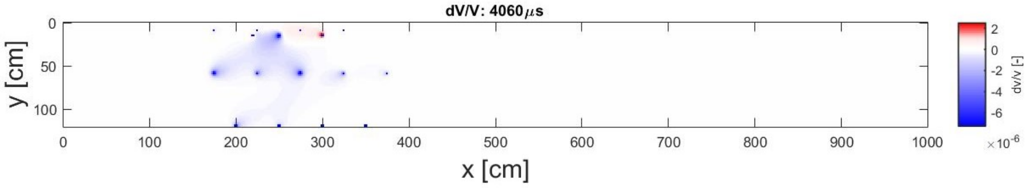

(c) Velocity plot for $t_{central} = 4060\mu s$.

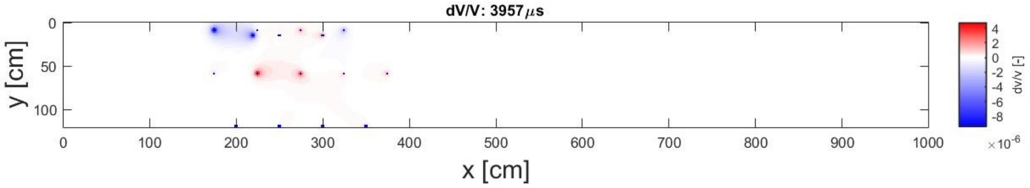

(d) Velocity plot for $t_{central} = 3957\mu s$.

Figure 4.10: Four different combinations of velocity maps gained from kernel diffusion approximation.

Plot 4.10b expressed similarity to the expected/predicted stress map, while Figure 4.10c, with a similar propagation of velocity variation (i.e. increase of velocity on top and decrease on the bottom), had a red-blue edge zone positioned at lower depth. It almost described the neutral axis as lifted up towards the top section. Nevertheless, at $4060\mu s$, and under a $150kN$ load, such a variation is not conceptually justified. This incoherence may have been generated by the stretching time window of analysis. The resulted outputs showed some details and unknowns which need to be further investigated, in order to expand the knowledge on this system, and so, to fully comprehend the methodology.

Figures 4.10a and 4.10d, on the other hand, presented an analogous stress map to

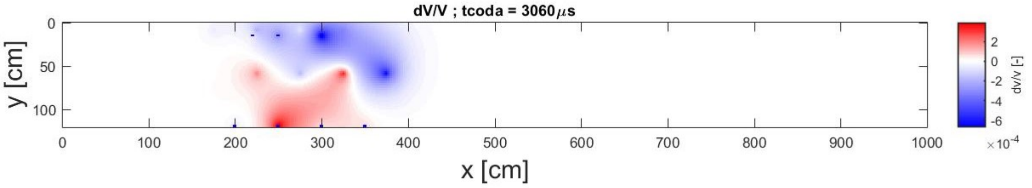

(a) Velocity plot for $t_{central} = 3060\mu s$.

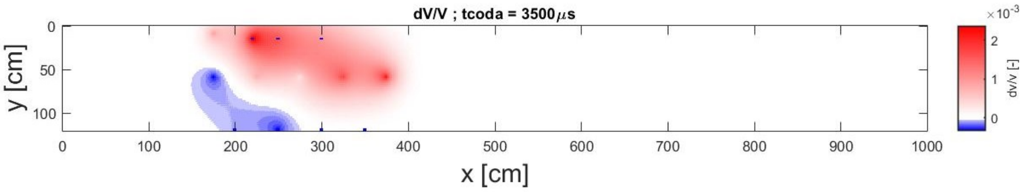

(b) Velocity plot for $t_{central} = 3500\mu s$.

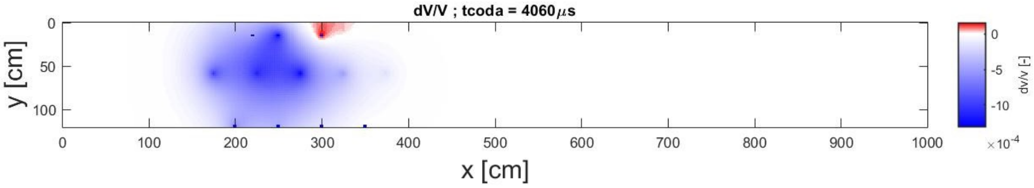

(c) Velocity plot for $t_{central} = 4060\mu s$.

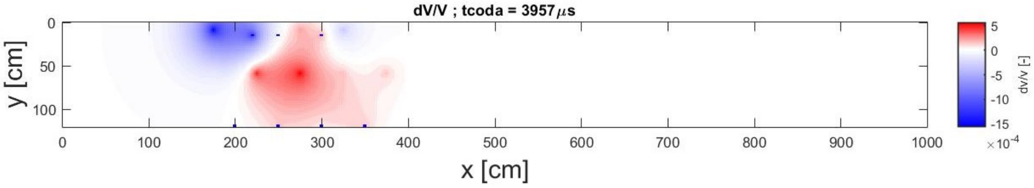

(d) Velocity plot for $t_{central} = 3957\mu s$.

Figure 4.11: Four different combinations of velocity maps obtained with respect to the radiative transfer definition.

the previous two, with opposed values of stretching (i.e. blue at the top and red at the bottom). Noteworthy, how the magnitude of the stress-state, inside the medium, appears to show similarity to the ones displayed in Figures 4.10b and 4.10c. This might be justified by the proximity of $t_{central}$, related to the kernel derivation, which presented a certain significance in the velocity definition.

Moreover, the magnitudes, showed in the colorplots vary in between 1 x 10^{-5} and -1 x 10^{-5}. When the velocity variation was detected, the magnitude of the inspected dv/v value was in accordance ($\approx \pm 5$ x 10^{-6}) with the various plots. Further tests, in parallel to the bending procedure, need to be developed, to provide a reliable calibration for the stress variation measure.

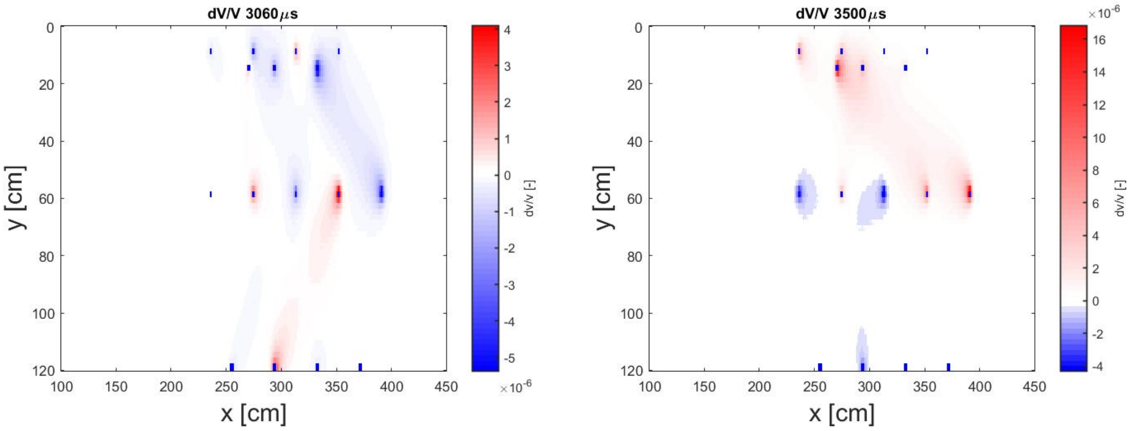

(a) Detail of velocity plot on sensors area for $t_{central} = 3060\mu s$

(b) Detail of velocity plot on sensors area for $t_{central} = 3500\mu s$

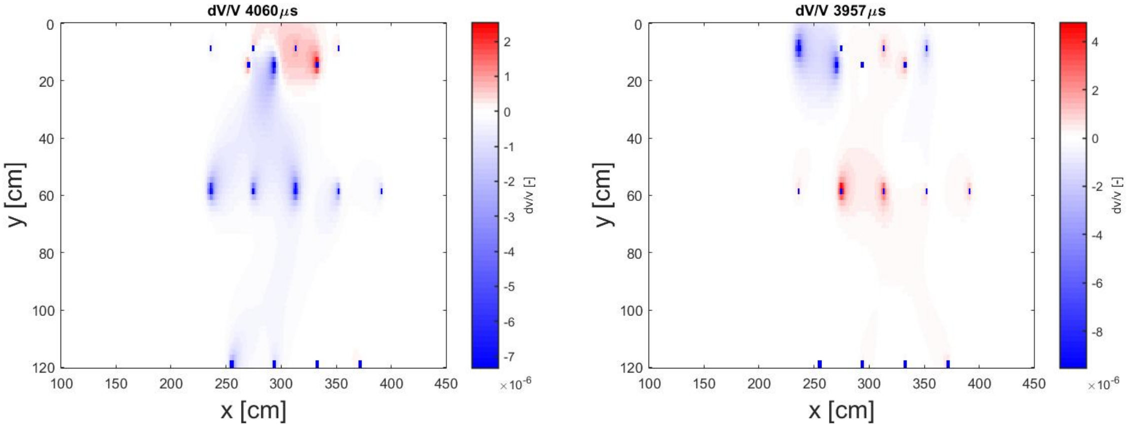

(c) Detail of velocity plot on sensors area for $t_{central} = 4060\mu s$

(d) Detail of velocity plot on sensors area for $t_{central} = 3957\mu s$

Figure 4.12: Proper detail on the area where sensors and the synthetic velocity changes have been applied

Analogously to what suggested in the synthetic analysis, future studies shall take a unique, redundant stretching ϵ related to several time windows, avoiding any possible momentous error led by incorrect window definition. To do so, it becomes essential to further investigate, both conceptually and experimentally, the needed central time of the sensitivity kernel. As for Figure 3.40, the entire path was repeated for a parallel hypothesis, providing a guidance to future research developments. By means of the above-mentioned 212 apparent velocity variations, for time windows in between $1507\mu s$ and $4899\mu s$ of $16\mu s$ width, a redundant unique ϵ parameter was averaged over; Figure 4.13 depicts the apparent velocity change plot.

For what concerned the sensitivity kernel, the assumption adopted $3203\mu s$ as central

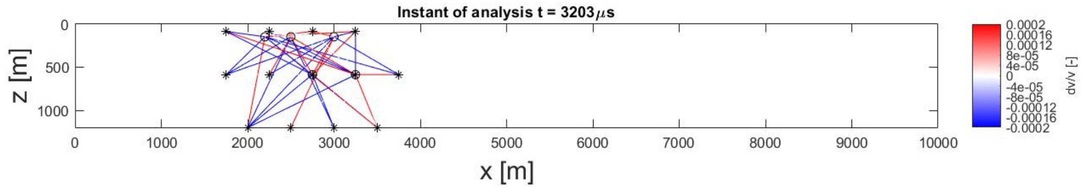

Figure 4.13: Stretched parameters at $t = 3203\mu s$, characterised by low magnitude.

instant of study. This time was obtained by considering the mean instant of the window. Figure 4.14 presents the two different plots, each in relation to both kernel definitions, while Figure 4.15, allows to better identify the analysed sector.

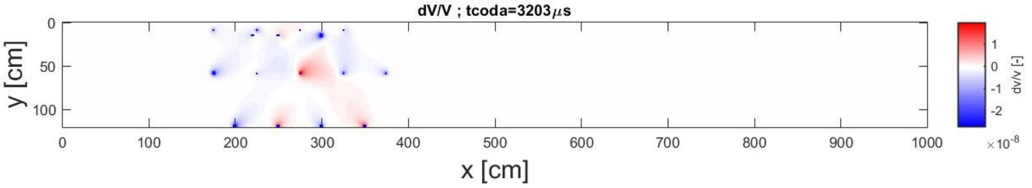

(a) Map gained from diffusive Intensity

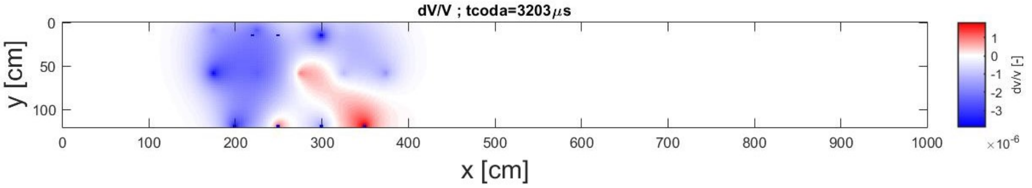

(b) Map gained from radiative transfer Intensity

Figure 4.14: Velocity plots gained from averaged apparent relative velocity change ϵ, for $t_{central} = 3203\mu s$

In the end, differently from Figure 3.40, the overall averaged velocity map (4.14) led to an improper, theoretically non-coherent, stress distribution. The error might be overtaken by changing the window width or by further issuing the $t_{central}$ for the kernel.

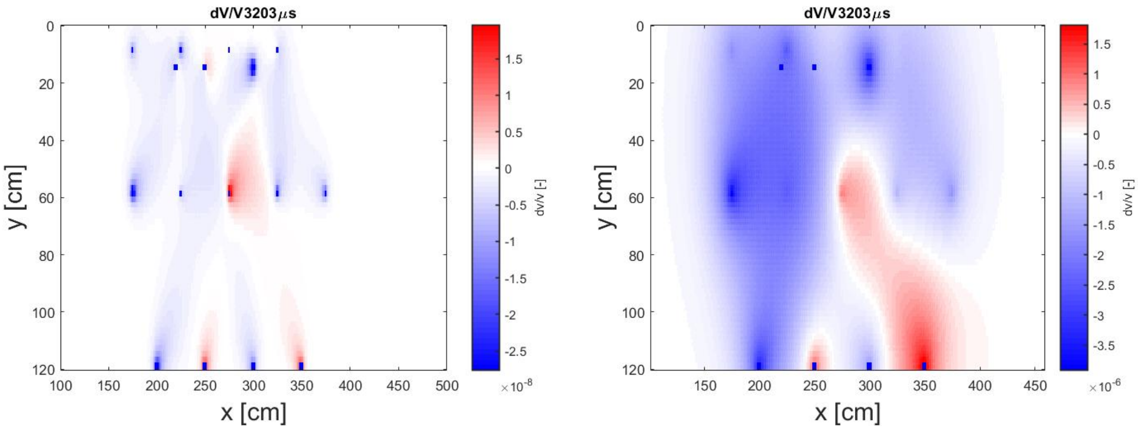

(a) Zoom of diffusive kernel analysis, Figure 4.14a **(b)** Zoom of diffusive kernel analysis, Figure 4.14b

Figure 4.15: Zoomed influence section from Figure 4.14

Conclusion

The present work aimed at investigating the reliability of Coda-Wave Interferometry as a monitoring technique. Thus, limits and potentialities were particularly under focus during the thesis' progress. At the same time, additional findings, oriented towards parallel environments of study, were obtained. The gained information, regarding the application of this technology, led to the definition of a series of parameters essential for further developments and for a better understanding of the CWI application.

Diffusion Study

Starting from the diffusivity parameter, its identification was widely discussed in this study due to the key role played over the entire CWI application.

Initially, the numerical study proposed to extract the D factor from the virtual signals: by means of the diffusion approximation model, the synthetic non-damped output was fitted. This process allowed to obtain a fundamental relationship between the diffusion property of the medium and its numerical statement, which, in this case, was simulated according to the Von Karman approximation. Two curves, different in shape, for $\sigma = 25\%$ and $\sigma = 10\%$ were assessed. As discussed in the dedicated section, both curves presented a proportional increase between diffusivity and correlation distance. When the area of the scatterer increases, it is agreeable to assume that the diffusion rises as well. This gets consistent when considering the extreme case of a medium, with infinite inhomoegenity area and no dissipation, which has an infinite diffusion of the wave: the signal does not get scattered at all and it keeps on uniformly propagating through the element. However, the two curves presented dissimilar shapes. Due to different scattering magnitude, a curve with fractional fluctuation of wave velocity of 10% showed higher values and a less severe growth than the curve with $\sigma = 25\%$. The reason of such behavioural difference can be found in the scattering properties regarding distinct wave field diffusion; the signal shape, is deeply affected by the scattering magnitude, which is reflected on D by the fitting model. Nevertheless, with just four values each, it is not consistent, yet, to state any assumptions from these curve.

Future works shall place a substantial focus on finalising the D-σ-a relationship (i.e. Diffusivity - Fractional Velocity Fluctuation - Correlation Distance). This can be improved, by applying the synthetic process, involving analyses of numerous correlation lengths; at the same time, various factors of fractional fluctuation velocity shall be tested, in order to acquire the complete association between the diffusion behaviour and the numerical statement of a Von Karman medium.

Regarding the diffusion study, a second fundamental reasoning was based on defining the appropriate calibration of numerical parameters, which, in this research, were driven by the real test signal evaluation. Using the laboratory beam under investigation, we acquired the diffusivity parameter for the specific concrete type and, in consequence of this, we adapted the synthetic evaluation to the real value (by means of the D-τ-ξ-a relation). Another challenging problem to address, consisted in splitting the decay section of the signal, within the fitting procedure. Both the scattering and the internal dissipation caused the decrements in the curve, therefore, the understanding of the physical diffusivity magnitude, with respect to the actual absorption time, presented some conceptual complexities. However, thanks to geophysics observation, it was possible to determine the absorption factor in advance and to obtain a coherent scattering parameter for concrete. Furthermore, the model presented a dependent τ - D combination: as the absorption parameter decreased, the diffusivity followed the same path (see tables and the colorplot depicted in its specific section).

Pointing towards this direction, future works should be focusing on further developing the theoretical definition of absorption time, while defining the proper model relation between this parameter and the diffusivity value. Improving this step would have the potentiality of numerically describing the structure, which could be used as additional starting point for practical application. Moreover, the definition of standardised properties, regarding the signal diffusion in concrete, might drive the ultrasonic-wave application towards materials science: signals can be characterised by the medium, thus, if properly processed, they can also provide reliable information on concrete ageing.

Some investigation need to be consider the practical sensor implementation and its emitted signal. As an example, in fact, the Fourier spectra showed a significant amount of energy, propagated through the medium, with different characteristics than the imposed one. This forced the research to apply an additional filtering step. Supplementary studies on the energy phase variation in practice need to be broaden, so that we can exhaustively explore the wave propagation theory, in order to exploit, as much as possible, the CWI application.

Sensitivity Kernel Extraction

Another investigated topic was based on the numerical extraction of the sensitivity kernel and on questioning its two model definition; (i.e. kernel derived from the diffusion approximation of intensity and from the radiative transfer solution). In this study, the main assumption regarded the interpretation of the energy propagation as resembling the wavefront distribution. Thus, during the work, we estimated the synthetic extraction of the wave probability scattering from $\mathbf{S}$ to $\mathbf{R}$, while passing through $\mathbf{x}$.

The shown maps specified how the kernel associated to the radiative transfer intensity presented different sensitivity areas, with respect to the diffusion approximation. The latter, indeed, depicted smaller values outside the ellipse which surrounds the two sensors. The radiative distribution, instead, appeared to have higher probability values and to be more defined over the entire ellipsoidal area of interest. Such a difference was also revealed by the magnitude variation; however, it was not consistent to state which one was characterised by a more coherent magnitude (i.e. which one presented the most expected wave probability distribution). It was not possible to compare the amplitude of numerical kernel values with the diffusion and radiative transfer ones. The synthetic sensitivity was obtained by developing an energy assumption, which drove the wave-field propagation; thus, to compare the order of magnitude, between the two theoretical models and the simulated one, would have been characterised by conceptual incoherence.

Further evaluations on this subject need to be developed in order to properly identify the correctness degree of the two 2D Boltzmann solutions. While expanding this analysis, the synthetic formulae, implemented in the energy propagation code, would require precise questioning; therefore, the study should not be performed in an absolute point of view, but rather, on a relative scale. If properly calibrated, it should be possible to compare the various magnitudes of probability and to state to what extent the diffusion approximation can give reliable output, with respect to the radiative solution of the Boltzmann equation.

Velocity Plots

Finally, the thesis needs to deal with some consideration on the velocity maps. The work investigation on the Interferometry technique, in fact, aimed at extracting the velocity plots to be subsequently related to the stress distribution inside a medium. By means of a synthetic and a real procedure, it was possible to fully develop such a path, oriented towards the acquisition of velocity field plots. The research tried to implement the computational analyses, where an intuitive, still reliable, coding process plays one of the most essential step to achieve, for actual CWI spreading.

First of all, the synthetic study had the role of giving the research the amount of correctness and sensitivity, the methodology is characterised by. This was due to the initially applied virtual change of velocity which drove the entire investigation.

The obtained numerical maps showed coherent variation values, with respect to the expected velocity distribution; the only fluctuations were located at the sensors position. The high value of diffusion kernel misled the apparent velocity variation expansion throughout the medium (i.e. $\epsilon_{i,j} \rightarrow \frac{dv}{v}(x, y)$). On the other side, the map, gained from the radiative transfer solution, presented a more logical definition of velocity. Moreover, the variations were different for each chosen window: substantial was the influence dictated by the central instant as well as the time width of study. Finally, although a small time window allowed a reliable and meaningful ϵ factor, at the same time, such width fell into momentary stretching errors inside the signal.

In order to counteract these mistakes, the research started and pursued a particular assumption. This led to the acquisition of several apparent relative velocity changes, regarding as many windows, and to extract a unique mean from them. This delicate step, then, consisted in identifying the correct sensitivity kernel to fit the averaged data: which $t_{central}$ the kernel definition is based on. The study followed the simplistic selection of central time, as the mean instant over the entire coda temporal-section, hypothesised to be analogous to averaging all the kernel matrices. In the end, the obtained plot showed reliable and expected features. However, the assumption on the sensitivity kernel, and the various window settings, should be further inspected; so that we could fully exploit the technique, while gaining the exact calibration on the $\frac{dv}{v}$ magnitude with respect to the actual - synthetically applied - velocity change. Expanding the simulation for different wave-types propagation would state a crucial step in the numerical CWI evaluation, which has been proved to be definitively connected to the procedural interpretation. By adding the S-waves to the, already presented, P-wave distribution would generate a substantial improvement in the methodological simulated operation.

Secondly, the laboratory-test velocity evaluation was conducted. Differently from the synthetic one, this step did not give reliable outcomes. In addition, although the same averaged apparent relative velocity variation path was applied, it kept on producing incorrect maps. Eventually, the practical CWI implementation led to a series of more complex and counter-intuitive errors, with respect to the simulated procedure, caused by several unknown factors. Such improper velocity field representation might find its reasons in the step of data gaining and filtering. However, the research extension did not pursue this error interpretation.

Additional researches, based on real test studies, need to be developed in order to correctly state the amplitude of eventual relative velocity changes regarding the actual state of stress inside the studied element. In this domain, future researches might need to investigate the signal differences, between external gel-application and embedded treatment of smart aggregates. It is safe to assume that the latter will present a much better signal definition; however, the first ones will ultimately state the practicability of this monitoring technique to already-existing structural applications. Another specification could be based on a more accurate application of load levels; by means of which, it should be possible to properly study the stress-state evolution inside an element.

Another delicate topic focused on the map extension capability. In fact, for economical and industrial sustainability in practical applications, it becomes essential to properly state the spacing between each sensor. This way, it should be possible to avoid any misplacing of smart aggregates, saving money, and, at the same time, to obtain the optimal distance so that they are capable of detecting any possible change in the stress field. To numerically state this extension, an additional synthetic test was performed: presented at the end of Appendix A, such a study involved a beam with the usual geometry settings, characterised by a different imposed velocity arrangement. The synthetically applied change consisted of a 'line' $10m$ long and $5cm$ thick, with an applied velocity variation of $\Delta v = -150m/s$. Once defined, the CWI technique (see chapter 3) was applied, but the obtained map resulted non coherent for both the kernel variations. The reason of such an incorrect evaluation might be based on the complex issue concerning the investigated time window. Further examination on gaining the sensitivity extension, that the studied methodology can reach, would result crucial for a feasible spreading of the methodology in a more practical optics.

Furthermore, the thesis horizons shall be broadened towards reinforced concrete structural elements. Hence, to gain correct interpretation of steel-concrete interaction would permit in-field applications to be investigated and, in parallel, real-time studies to be developed. By means of these studies and continuous optimisation works, this technique might result to actually be at the forefront of the monitoring area as a reliable and coherent methodology. It should not be inappropriate to think that a large scale application, perhaps regarding the great majority of infrastructures, could become an essential asset for future maintenance operations. As specified in section 1.3, a proper CWI implementation may have the potentiality to become the actual main safety action of the health-monitoring sector. Next studies should also be focused on real-time data interpretation, with corresponding prediction-based evaluations, to initiate a brand new preservation and enhancement system. At the same time, the possibility of assessing the stress-state of generic structural elements would determine a great advantage. As an example, after extreme events, the visual structural-health inspections could ultimately be replaced by a more redundant and unequivocal numerical analysis.

In this work, we found, discussed, and solved, multiple issues. However, several questions still remain unanswered. This final chapter had the role of highlighting the obtained results while underlining the present limits of CWI. At the same time, suggestions and ideas for improvement have been herein presented. In order to enhance the comprehension of this technique, the idea of performing and processing a number of additional tests may become crucial for the success of structural-health monitoring by Coda-Wave Interferometry: this way, it will be possible to gain a better understanding on the algorithm and get a better physical explanation of the results.

Appendices

A

Synthetic Analysis

A.1 Diffusivity and Absorption Time

In this appendix, the two further examples of error colorplot, for the Diffusivity evaluation, are firstly presented. Figures 3.10 and 3.13, indeed, show the very analogous images depicted by Figures A.1 and A.2, now with respect to correlation length of $3cm$ and $4cm$ for the two ϵ values.

For completeness, tables A.1 and A.2 are here reported, for the selected source-receiver pairs, in the evaluation of the relationship between the absorption time and the diffusivity constant.

The variation of τ led to a change in the diffusivity. This is explained by the fitting characteristic of the model: being both exponentially elevated, negatively, (e^{-X}) generates a strong influence between the two factors during the constants extraction.

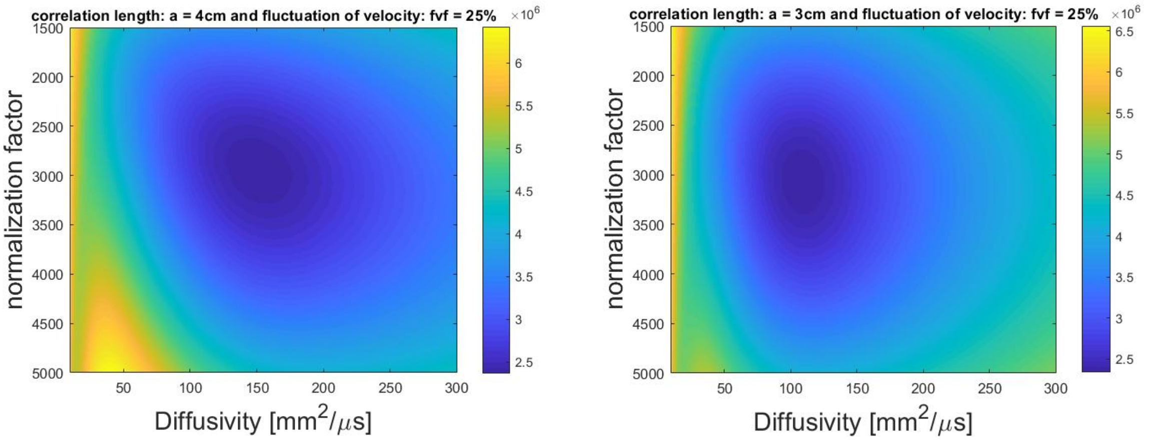

(a) Example for $a = 4cm$ and $\epsilon = 25\%$ **(b)** Example for $a = 3cm$ and $\epsilon = 25\%$

Figure A.1: Colorplots of misfit errors between normalisation factor and diffusivity.

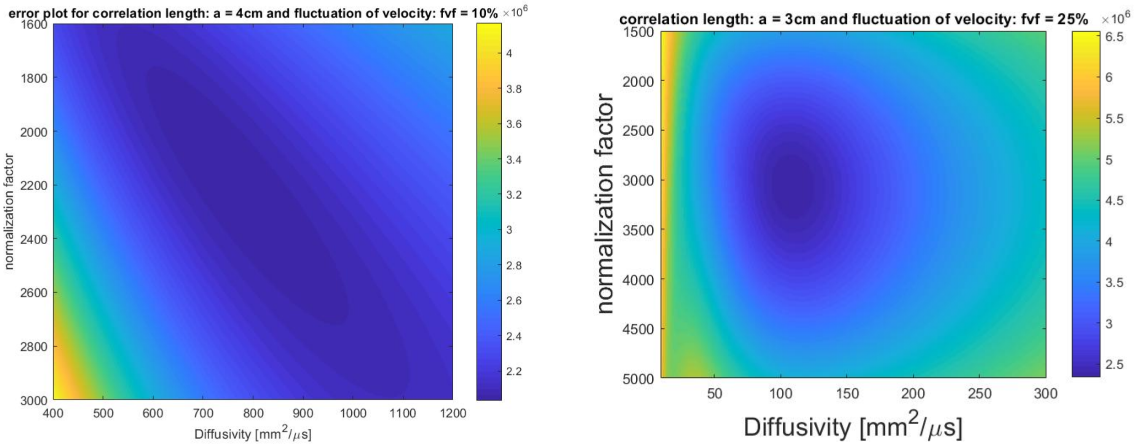

(a) Example for $a = 4cm$ and f.v.f. of 10% **(b)** Example for $a = 3cm$ and f.v.f. of 10%

Figure A.2: Colorplots of misfit errors between normalisation factor and diffusivity.

A.2 Stretching

A.2.1 Parameters and Coefficients

The three tables A.3, A.4 and A.5 describe, for the three relative windows, the stretching ϵ parameters, with respect to their correlation coefficients.

Tables A.6, A.7, A.8, and A.9 depict the stretching factors and corresponding correlation coefficients, for every source-receiver couple, with respect to the previously discussed four different windows of $t_{central} = 1667\mu s$, $t_{central} = 2050\mu s$, $t_{central} = 2381\mu s$ and

Table A.1: Obtained diffusivity from real test signals (source AE13) with respect to specified dissipation factors. All evaluated τ are here represented.

			AE13			
τ	**SA1**	**SA2**	**SA3**	**SA4**	**SA5**	**MEAN**
300	187	162	197	187	137	174
229	133	115	145	131	87	122
200	82	99	125	110	71	97
162	60	77	98	86	56	75
50	18	22	24	19	11	19

Table A.2: Obtained diffusivity from real test signals (source AE1) with respect to specified dissipation factors. A series of τ are here represented.

			AE1			
τ	**SA1**	**SA2**	**SA3**	**SA4**	**SA5**	**MEAN**
300	114	258	235	402	421	286
229	70	160	148	237	264	176
200	57	127	120	187	211	140
168	44	92	90	139	160	105
50	9	18	17	24	28	19

$t_{central} = 2063\mu s$; these four instants will lead a consistent kernel evaluation in a second phase. The rows in such tables are 14 rather than 13, because of an additional data set gained out of the emission of all sources at the same instants (referred to as **All AE**).

Moreover, in table A.9, a much wider window ($\Delta t = 793\mu s$), with central time as $t_{central} = 2050\mu s$, is shown and analysed to increase the reliability of the other windows.

A.2.2 Windows of Study

For the same stretching windows, the signals are shown, before and after stretching, in Figures A.3, A.4 and A.5.

A.3 Sensitivity Kernel

The kernel evaluation regarding different time instants of $t_{central} = 1667\mu s$ and $t_{central} = 2381\mu s$, for various source-receiver pairs, in Figures A.6 and A.7

Table A.3: Stretching parameters and Correlation Coefficients for a time window centred in $t_{central} = 2050\mu s$ with length $16\mu s$ (colour settings analogous to table 3.2).

	Window =2042μs - 2058μs									
	Epsilon					**Correlation**				
	SA1	**SA2**	**SA3**	**SA4**	**SA5**	**SA1**	**SA2**	**SA3**	**SA4**	**SA5**
AE1	-1,30E-03	-5,00E-04	0,00E+00	-3,00E-04	2,95E-03	0,987316	0,94967	0,728846	0,941848	0,898695
AE2	-1,95E-03	-3,10E-03	-9,50E-04	-3,00E-04	-4,10E-03	0,919136	0,99724	0,952415	0,825684	0,947536
AE3	2,50E-03	8,50E-03	-8,00E-04	-2,10E-03	-8,90E-03	0,986989	0,907354	0,979729	0,951617	0,902515
AE4	-8,50E-03	-1,45E-03	-7,30E-03	-1,50E-04	-1,70E-03	0,946871	0,882499	0,756244	0,967548	0,742875
AE5	1,00E-02	2,75E-03	5,50E-04	3,00E-04	-7,15E-03	0,548158	0,982436	0,917512	0,973753	0,9594
AE6	-3,20E-03	-3,25E-03	-4,75E-03	-5,50E-04	-1,85E-03	0,946031	0,578228	0,824931	0,98011	0,984599
AE7	3,55E-03	-3,80E-03	2,75E-03	-3,25E-03	-9,00E-04	0,909861	0,935021	0,884719	0,578296	0,948714
AE8	-5,90E-03	-4,10E-03	-1,00E-04	-1,35E-03	-2,25E-03	0,953399	0,995516	0,87991	0,899867	0,746112
AE9	-1,00E-02	-9,05E-03	-2,25E-03	-3,00E-04	-3,95E-03	0,70426	0,796605	0,9131	0,882541	0,921189
AE10	3,30E-03	-4,80E-03	-4,30E-03	5,35E-03	3,10E-03	0,948725	0,679129	0,819912	0,979673	0,956515
AE11	-5,95E-03	7,90E-03	9,45E-03	-1,00E-02	2,70E-03	0,949066	0,844771	0,978872	0,874194	0,994595
AE12	-1,65E-03	-7,35E-03	-4,20E-03	-2,20E-03	1,20E-03	0,667236	0,389864	0,998894	0,495605	0,979897
AE13	-3,55E-03	-1,25E-03	5,80E-03	1,05E-03	-6,10E-03	0,797379	0,991433	0,994336	0,786949	0,892023

Table A.4: Stretching parameters and Correlation Coefficients for a time window centred in $t_{central} = 2381\mu s$ with length $16\mu s$ (colour settings analogous to table 3.2).

	Window = 2373μs - 2389μs									
	Epsilon					**Correlation**				
	SA1	**SA2**	**SA3**	**SA4**	**SA5**	**SA1**	**SA2**	**SA3**	**SA4**	**SA5**
AE1	-9,15E-03	-1,00E-02	6,00E-04	-8,00E-04	-3,15E-03	0,865795	0,773333	0,876889	0,980304	0,966448
AE2	1,00E-02	9,00E-03	-6,35E-03	-6,00E-04	-6,10E-03	0,93938	0,946555	0,922454	0,97601	0,880063
AE3	8,60E-03	-1,65E-03	-2,40E-03	-4,25E-03	5,25E-03	0,995385	0,800175	0,973877	0,946771	0,999176
AE4	-4,65E-03	9,50E-03	-2,80E-03	8,95E-03	5,70E-03	0,975342	0,969733	0,956938	0,899574	0,662193
AE5	-8,95E-03	-2,00E-03	-4,00E-04	3,00E-04	-7,80E-03	0,965277	0,653972	0,96821	0,99531	0,996525
AE6	-2,85E-03	2,40E-03	-4,80E-03	-1,25E-03	-3,35E-03	0,9883	0,77893	0,988798	0,866978	0,84776
AE7	-1,00E-02	-1,75E-03	-7,45E-03	2,40E-03	-2,10E-03	0,860135	0,961616	0,968914	0,779424	0,982119
AE8	2,10E-03	8,20E-03	6,15E-03	-8,55E-03	5,50E-03	0,907904	0,930134	0,993304	0,994905	0,919818
AE9	-1,00E-02	8,85E-03	-3,80E-03	-4,00E-03	-4,85E-03	0,825334	0,98662	0,975618	0,972343	0,831571
AE10	3,90E-03	9,50E-03	5,00E-05	5,00E-04	-5,00E-05	0,805229	0,95432	0,979475	0,979307	0,993505
AE11	-1,90E-03	-4,60E-03	-9,00E-04	-3,80E-03	-9,55E-03	0,867481	0,788369	0,945314	0,91383	0,980928
AE12	7,50E-03	-1,85E-03	-1,00E-02	-2,75E-03	-1,00E-02	0,92441	0,715427	0,943679	0,921589	0,827587
AE13	6,40E-03	9,35E-03	-7,40E-03	-2,15E-03	-2,45E-03	0,983	0,979344	0,994867	0,763796	0,994421

A.4 Additional Study

In order to increase the reliability of the simulation, and to extract useful information about the proper spacing between each sensor, a synthetic element was additionally studied. This investigation was structured in analogous manner to the one processed in chap-

Table A.5: Stretching parameters and Correlation Coefficients for a time window centred in $t_{central} = 2064\mu s$ with length $16\mu s$ (colour settings analogous to table 3.2).

	Window $=2055\mu s$ - $2071\mu s$									
	Epsilon					**Correlation**				
	SA1	**SA2**	**SA3**	**SA4**	**SA5**	**SA1**	**SA2**	**SA3**	**SA4**	**SA5**
AE1	-1,55E-03	-8,00E-04	-1,00E-02	1,00E-04	-6,00E-03	0,952808	0,978893	0,936971	0,853225	0,746882
AE2	2,00E-04	-7,10E-03	-1,90E-03	-4,50E-04	-8,50E-04	0,76898	0,899472	0,913528	0,95371	0,998558
AE3	-9,70E-03	7,85E-03	9,10E-03	1,05E-03	-9,00E-04	0,949982	0,689122	0,993274	0,964154	0,763344
AE4	5,00E-04	1,40E-03	-6,40E-03	9,65E-03	-8,65E-03	0,860124	0,946534	0,941808	0,804639	0,969204
AE5	-1,95E-03	6,05E-03	-4,85E-03	5,00E-04	-5,20E-03	0,945593	0,878406	0,870429	0,654372	0,92768
AE6	-3,25E-03	3,65E-03	2,80E-03	-1,05E-03	3,80E-03	0,904791	0,681498	0,959103	0,85901	0,529653
AE7	1,00E-02	-3,20E-03	-1,00E-02	3,65E-03	9,05E-03	0,581001	0,890738	0,907222	0,681577	0,954162
AE8	8,20E-03	-9,50E-03	-5,00E-03	-1,60E-03	5,90E-03	0,901623	0,882574	0,895049	0,956507	0,94102
AE9	2,65E-03	-8,05E-03	-8,65E-03	-7,50E-04	-4,20E-03	0,896665	0,946035	0,974962	0,932192	0,812579
AE10	-3,15E-03	-3,80E-03	-7,00E-04	-9,50E-04	2,40E-03	0,970016	0,84195	0,985239	0,961605	0,888188
AE11	-4,40E-03	-9,00E-04	-4,70E-03	5,85E-03	3,65E-03	0,918788	0,905127	0,802209	0,621036	0,863676
AE12	-1,75E-03	-4,05E-03	-6,95E-03	-8,80E-03	-8,45E-03	0,923587	0,998813	0,908677	0,813738	0,870276
AE13	-2,50E-04	-7,25E-03	-1,45E-03	7,65E-03	4,85E-03	0,843411	0,980769	0,838429	0,961286	0,750973

Table A.6: Stretching parameters and Correlation Coefficients for a time window centred in $t_{central} = 1667\mu s$ with length $120\mu s$. In green colour the correlation values above 70%, in yellow the ones with a $cc = 50\% < CC < 70\%$, and in red coefficients characterised by correlation below 50%.

	Window $= 1607\mu s - 1727\mu s$									
	Epsilon					**Correlation**				
	SA1	**SA2**	**SA3**	**SA4**	**SA5**	**SA1**	**SA2**	**SA3**	**SA4**	**SA5**
AE1	-1,00E-03	-4,50E-04	5,00E-04	-5,00E-05	-1,20E-03	0,592539	0,517782	0,744245	0,957733	0,755882
AE2	-3,40E-03	-1,20E-03	-2,50E-04	-3,00E-04	-3,55E-03	0,87464	0,601742	0,638556	0,896277	0,654939
AE3	-1,00E-03	-1,05E-03	-4,75E-03	-4,50E-04	-2,35E-03	0,705366	0,759955	0,317783	0,710265	0,421055
AE4	-8,50E-04	-6,50E-04	-9,50E-04	-3,50E-04	-1,25E-03	0,735839	0,75601	0,566368	0,746454	0,710094
AE5	-5,50E-03	-1,90E-03	-5,00E-04	-2,00E-04	-1,35E-03	0,72473	0,765758	0,87911	0,896862	0,743398
AE6	-3,00E-03	3,50E-04	-3,75E-03	-3,00E-04	-3,95E-03	0,536652	0,451474	0,556272	0,79172	0,388834
AE7	-7,35E-03	-5,65E-03	-1,80E-03	3,50E-04	-3,55E-03	0,352159	0,500269	0,39278	0,451371	0,572773
AE8	-1,10E-03	-1,20E-03	-2,65E-03	7,90E-03	-1,80E-03	0,632099	0,280955	0,639729	0,246975	0,618674
AE9	6,50E-04	-2,15E-03	-1,25E-03	-3,45E-03	-3,65E-03	0,68952	0,642109	0,464625	0,585517	0,335584
AE10	-2,65E-03	-5,50E-03	-9,50E-04	-4,00E-04	-3,60E-03	0,795789	0,50286	0,682592	0,814118	0,766574
AE11	-3,35E-03	-3,95E-03	-1,60E-03	-4,35E-03	1,00E-02	0,64548	0,5049	0,364076	0,557477	0,21711
AE12	-3,00E-04	-1,05E-03	-5,85E-03	-2,95E-03	-3,00E-03	0,616306	0,541942	0,591536	0,408126	0,646673
AE13	-1,15E-03	1,00E-03	-3,70E-03	-1,30E-03	-3,50E-03	0,652506	0,451203	0,492188	0,844936	0,418969
all AEs	-4,00E-04	-1,05E-03	-5,15E-03	-2,50E-04	-3,25E-03	0,630032	0,479381	0,443306	0,831025	0,549543

ter 3. It took into consideration a layer of velocity change of $\Delta V = -150m/s$, $5cm$ thick, and $10m$ long, as depicted in Figure A.8. The aim, on which this research was based, consisted in understanding up to which distance the CWI technique was able to detect a

Table A.7: Stretching parameters and Correlation Coefficients for a time window centred in $t_{central} = 2050\mu s$ with length $120\mu s$ (colour settings analogous to table A.6).

	Window $= 1990\mu s - 2110\mu s$									
	Epsilon					**Correlation**				
	SA1	**SA2**	**SA3**	**SA4**	**SA5**	**SA1**	**SA2**	**SA3**	**SA4**	**SA5**
AE1	-1,45E-03	-8,50E-04	-4,00E-04	-1,50E-04	-3,00E-04	0,805262	0,613912	0,791755	0,941234	0,580002
AE2	-1,25E-03	-2,85E-03	-1,30E-03	-2,50E-04	-3,10E-03	0,754064	0,83419	0,935507	0,904726	0,833285
AE3	-1,85E-03	-0,00045	-6,50E-04	-1,05E-03	-3,05E-03	0,798094	0,510643	0,699618	0,631072	0,487287
AE4	1,00E-04	-3,05E-03	-6,35E-03	-3,50E-04	-1,10E-03	0,530891	0,833471	0,547233	0,727529	0,70088
AE5	-8,50E-04	-4,75E-03	-8,00E-04	1,00E-04	-0,0011	0,738937	0,715146	0,88631	0,936475	0,710977
AE6	-2,45E-03	-3,50E-04	-2,80E-03	-3,00E-04	-1,15E-03	0,612675	0,540287	0,739612	0,809131	0,820735
AE7	-2,00E-04	-2,60E-03	-5,75E-03	-3,50E-04	-6,45E-03	0,535661	0,761281	0,501311	0,540141	0,674641
AE8	-6,00E-04	-9,50E-04	-8,50E-04	-1,20E-03	-2,95E-03	0,408748	0,533052	0,843219	0,755828	0,540821
AE9	5,50E-04	-0,00325	-2,65E-03	-1,30E-03	-2,85E-03	0,805104	0,708865	0,492398	0,891858	0,681854
AE10	-1,00E-03	-1,40E-03	-4,50E-03	-1,00E-03	2,55E-03	0,795148	0,477538	0,845569	0,76993	0,728697
AE11	0,0036	-2,45E-03	-5,20E-03	-9,80E-03	-4,25E-03	0,360724	0,418958	0,7236	0,475522	0,722295
AE12	-1,95E-03	-2,75E-03	-2,25E-03	-1,40E-03	-3,20E-03	0,539296	0,61713	0,600053	0,574052	0,626205
AE13	-8,50E-04	-1,45E-03	-1,00E-02	-7,00E-04	-4,95E-03	0,696176	0,494932	0,48897	0,732369	0,643865
all AEs	-9,00E-04	-2,90E-03	-5,30E-03	-5,00E-04	-8,50E-03	0,766908	0,744671	0,66247	0,665138	0,597486

Table A.8: Table containing stretching parameters and Correlation Coefficients for a time window centred in $t_{central} = 2381\mu s$ with length $120\mu s$ (colour settings analogous to table A.6).

	Window $= 2321\mu s - 2441\mu s$									
	Epsilon					**Correlation**				
	SA1	**SA2**	**SA3**	**SA4**	**SA5**	**SA1**	**SA2**	**SA3**	**SA4**	**SA5**
AE1	-2,45E-03	-9,50E-04	-3,50E-04	-5,00E-04	-2,60E-03	0,77702	0,852545	0,891829	0,932032	0,843704
AE2	-3,50E-04	-8,00E-04	-5,00E-05	-2,50E-04	-6,65E-03	0,611353	0,481059	0,837941	0,908465	0,55026
AE3	-2,70E-03	-0,0026	-2,85E-03	5,50E-04	-2,65E-03	0,834331	0,788501	0,805897	0,707117	0,827151
AE4	-1,00E-04	-7,00E-04	-8,00E-04	0,00E+00	-3,15E-03	0,79826	0,716492	0,805793	0,632239	0,67027
AE5	1,00E-02	-1,10E-03	-2,00E-04	1,00E-04	-0,00115	0,572883	0,888443	0,897085	0,925544	0,903435
AE6	-2,50E-03	-4,05E-03	1,00E-02	-5,00E-04	-2,45E-03	0,918858	0,740215	0,549976	0,848028	0,843969
AE7	-3,95E-03	-9,00E-04	-2,60E-03	-4,05E-03	-4,10E-03	0,511758	0,774679	0,486316	0,739904	0,798303
AE8	-5,50E-03	-5,80E-03	-2,55E-03	-2,35E-03	-4,40E-03	0,357469	0,612636	0,693399	0,594418	0,560648
AE9	-6,50E-04	-0,00225	-4,45E-03	-2,10E-03	-4,10E-03	0,745411	0,602637	0,806728	0,830303	0,519778
AE10	-2,20E-03	-1,30E-03	-2,50E-04	-4,50E-04	-6,00E-04	0,824773	0,653549	0,78139	0,913747	0,923912
AE11	-0,0045	-4,05E-03	-1,40E-03	-2,70E-03	-3,70E-03	0,667177	0,412006	0,443443	0,743588	0,823646
AE12	-3,70E-03	-1,00E-02	-2,55E-03	-1,15E-03	-9,00E-03	0,522988	0,392585	0,686354	0,747226	0,372494
AE13	2,50E-04	-2,50E-04	4,40E-03	-2,35E-03	-4,35E-03	0,863898	0,584604	0,539654	0,889355	0,55155
all AEs	1,00E-02	5,75E-03	1,00E-02	-8,00E-04	-2,90E-03	0,36538	0,359578	0,544738	0,810243	0,484412

synthetically applied velocity change.

However, this analysis did not produce correct outcomes, as specified in Figure A.9 and Figure A.10 (therefore briefly mentioned in this Appendix). The two kernel approx-

Table A.9: Table containing stretching parameters and Correlation Coefficients for a time window centred in $t_{central} = 2064\mu s$ with length $793\mu s$ (colour settings analogous to table A.6).

	Window $= 1667\mu s - 2460\mu s$									
	Epsilon					**Correlation**				
	SA1	**SA2**	**SA3**	**SA4**	**SA5**	**SA1**	**SA2**	**SA3**	**SA4**	**SA5**
AE1	-1,30E-03	-6,50E-04	-3,00E-04	-1,50E-04	-1,40E-03	0,740227	0,623769	0,767755	0,931352	0,629154
AE2	-1,50E-03	-1,00E-03	-8,00E-04	-3,00E-04	-3,60E-03	0,719742	0,655942	0,81108	0,884541	0,666339
AE3	-8,50E-04	-0,00115	-8,50E-04	-5,00E-04	-2,55E-03	0,687479	0,574589	0,520102	0,701102	0,515044
AE4	-6,50E-04	-1,00E-03	-9,50E-04	-5,50E-04	-1,15E-03	0,719319	0,713771	0,59963	0,706835	0,581827
AE5	-1,20E-03	-1,05E-03	-5,00E-04	0,00E+00	-0,0015	0,683675	0,726275	0,874603	0,934262	0,745088
AE6	-2,80E-03	-3,50E-04	-7,00E-04	-2,50E-04	-1,70E-03	0,56003	0,483052	0,587627	0,799892	0,527852
AE7	-2,70E-03	-1,00E-03	-2,60E-03	-3,50E-04	-3,25E-03	0,445155	0,381425	0,343108	0,48283	0,497422
AE8	-9,50E-04	-1,40E-03	-2,70E-03	-1,10E-03	-2,25E-03	0,559578	0,339187	0,61041	0,452599	0,517393
AE9	-4,50E-04	-0,0015	-1,55E-03	-1,15E-03	-3,65E-03	0,708896	0,579719	0,49574	0,730512	0,473337
AE10	-2,60E-03	-3,70E-03	-1,15E-03	-4,00E-04	-2,90E-03	0,752931	0,453065	0,777807	0,829761	0,649263
AE11	-0,0034	-4,70E-03	-5,85E-03	-5,10E-03	-3,80E-03	0,518867	0,347658	0,445966	0,384869	0,337113
AE12	-5,50E-04	-2,90E-03	-5,50E-03	-2,85E-03	-2,70E-03	0,484516	0,37501	0,504795	0,428753	0,564148
AE13	-8,50E-04	-1,10E-03	-2,90E-03	-1,15E-03	-1,05E-03	0,664056	0,457574	0,425544	0,715497	0,515792
all AEs	-8,00E-04	-1,35E-03	-3,25E-03	-5,00E-04	-3,05E-03	0,559355	0,481616	0,487118	0,783415	0,55051

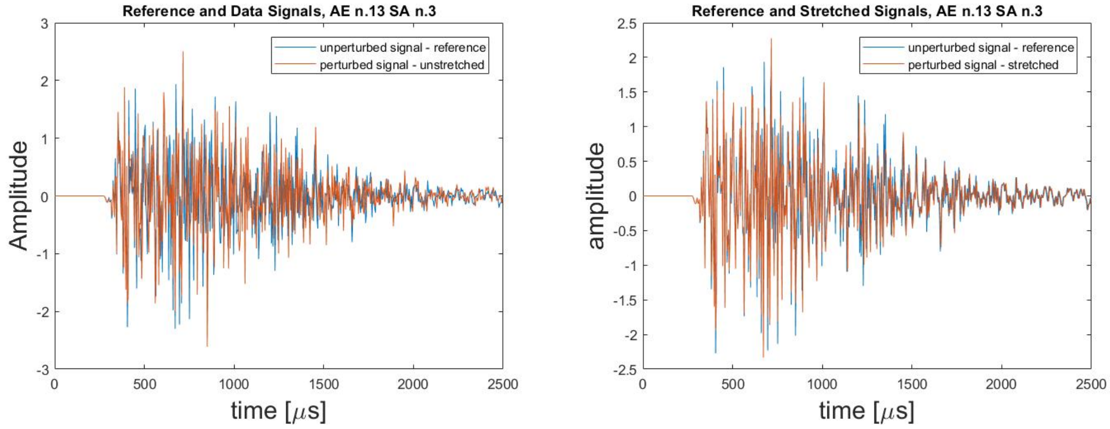

Figure A.3: Perturbed and unperturbed signals, stretched and non-stretched with highlighted different windows. For pair AE13-SA3.

imations are highlighted, for this test, in Figure A.10, although both of them did not provide reliable results.

Analogously to the main test, the assumption of averaging the totality of the extracted ϵ, over the entire coda section, in combination with the hypothesised $t_{central} = 2035\mu s$, led to the definition of a comprehensive, unique plot: Figure A.11 shows the gained plot with respect to either the radiative transfer and diffusion kernel evaluation.

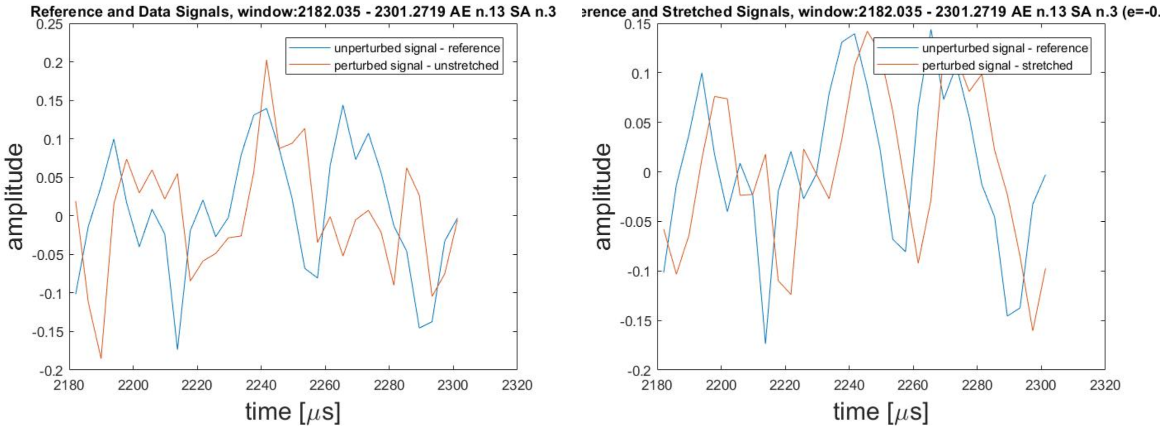

Figure A.4: Zoomed window of analysis at $2182\mu s - 2301\mu s$, stretched and non-stretched (pair AE13-SA3).

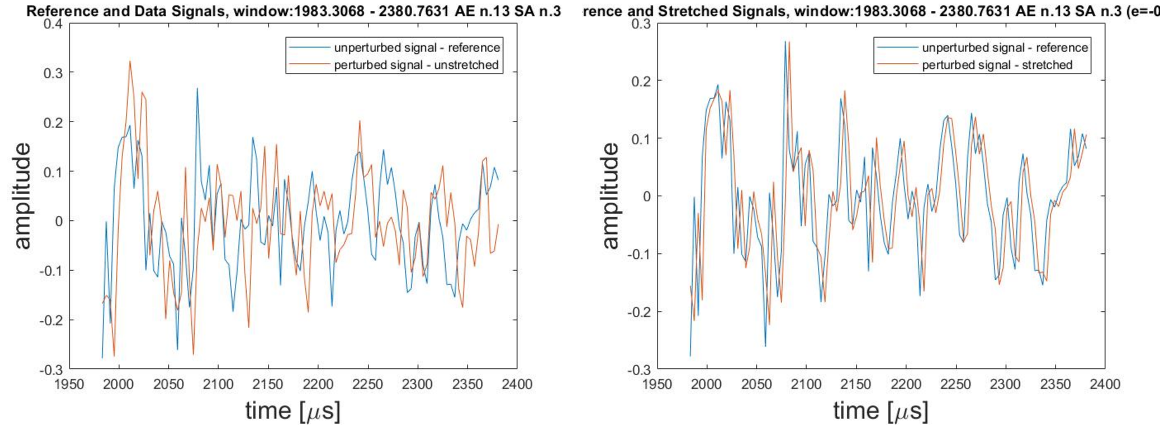

Figure A.5: Zoomed window of analysis at $1983\mu s - 2380\mu s$, stretched and non-stretched (pair AE13-SA3). This specific window has length $\approx 397\mu s$.

An additional step, defined in the literature [78] [103], would have regarded an analytical accuracy interpretation of the results by means of the cost function:

$$e_{optimal}(\boldsymbol{x}) = \sum_{i,j} \frac{[\epsilon_{ij}^{experimental}(t) - \epsilon_{ij}^{theoretical}(\boldsymbol{x}, t)]^2}{error^2} \tag{A.1}$$

where $\epsilon^{experimental}$ denotes the experimental measurements and $\epsilon^{theoretical}$ states the theoretical values, assumed at $\mathbf{x}$. The measured changes fluctuations describe the *error* value. Subsequently, the gained $e_{optimal}$ would have been strictly correlated to the maximum likelihood χ^2 and only the velocity values in map grid sector $\boldsymbol{x}$, with $\chi^2 \approx 1$, would have been taken into consideration.

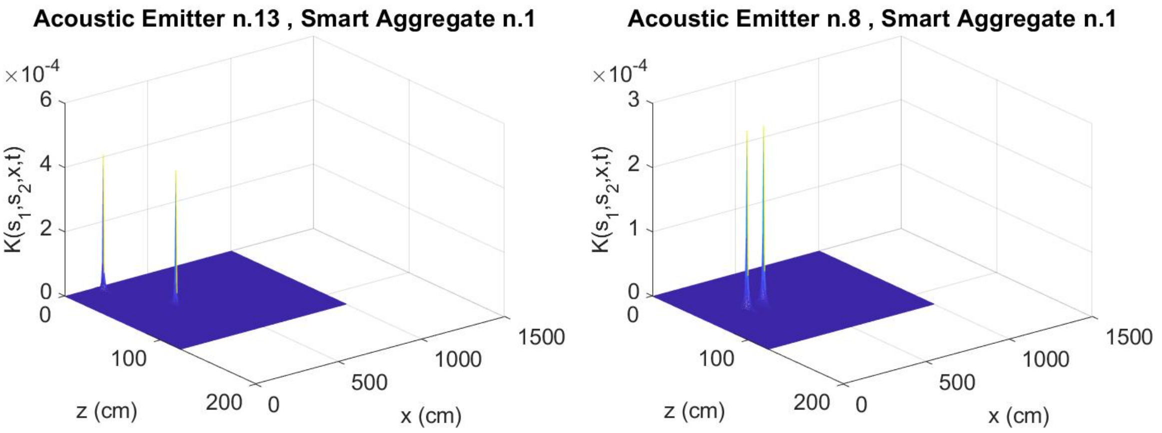
Acoustic Emitter n.13 , Smart Aggregate n.1

Acoustic Emitter n.8 , Smart Aggregate n.1

(a) pair: AE13-SA1 **(b)** pair: AE8-SA1

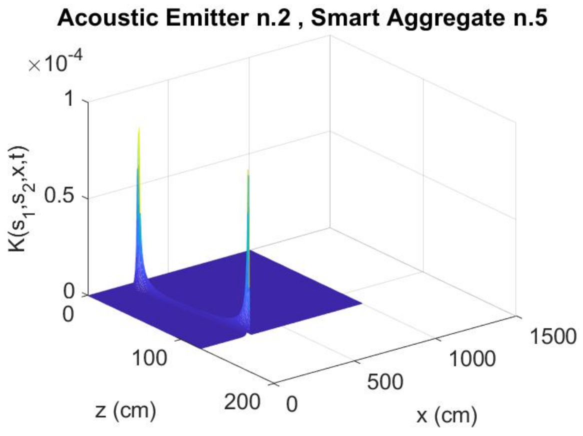
Acoustic Emitter n.2 , Smart Aggregate n.5

(c) pair: AE2-SA5

Figure A.6: Three different configurations of sensitivity kernel for $t_{central} = 1667\mu s$.

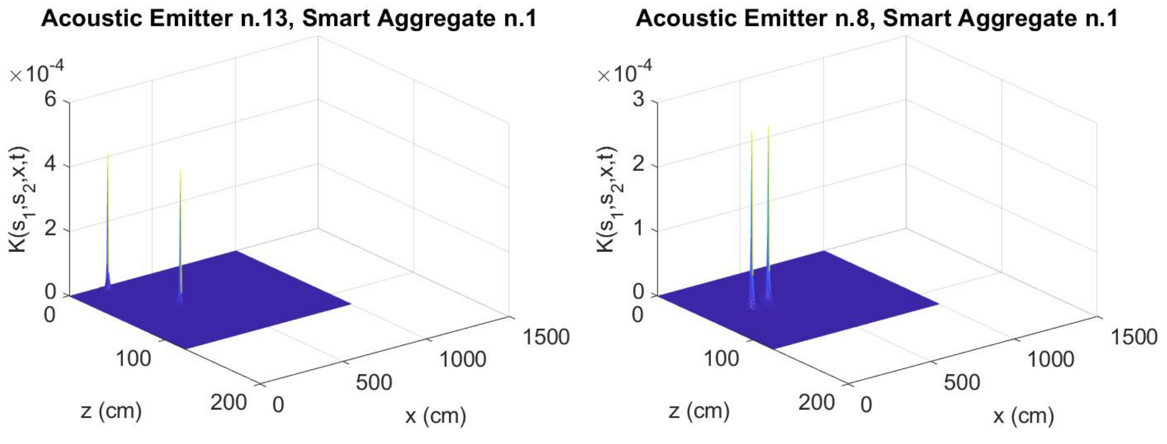

(a) pair: AE13-SA1

(b) pair: AE8-SA1

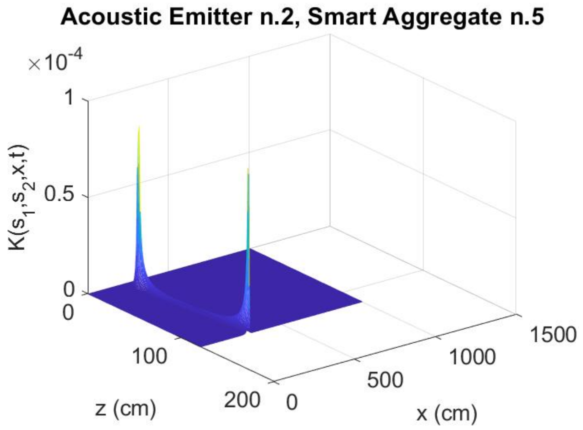

(c) pair: AE2-SA5

Figure A.7: Three different configurations of sensitivity kernel for $t_{central} = 2381\mu s$.

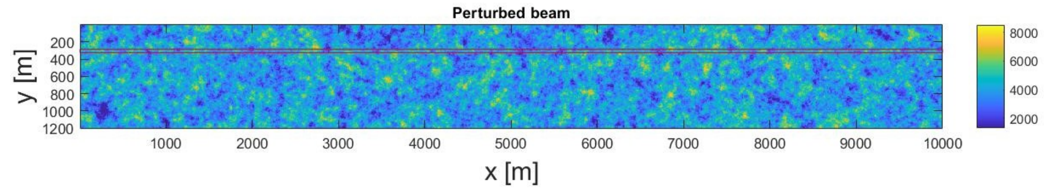

(a) Velocity distribution in perturbed beam; highlighted in red the area of synthetic variation.

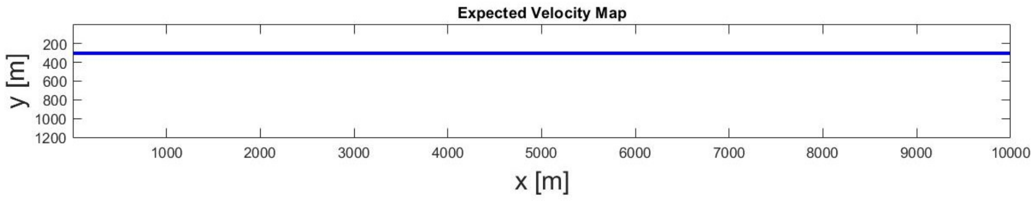

(b) expected velocity plot for the above applied velocity variation.

Figure A.8: Graphical representation of perturbed beam and expected velocity map

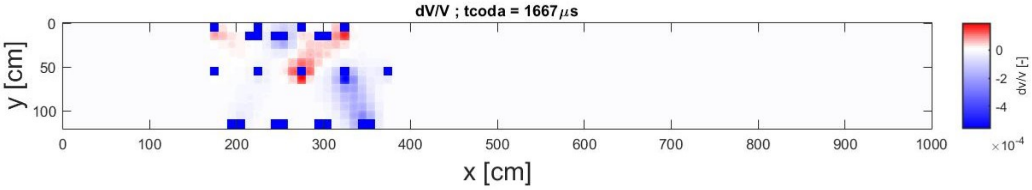

(a) Velocity plot for $t_{central} = 1667\mu s$.

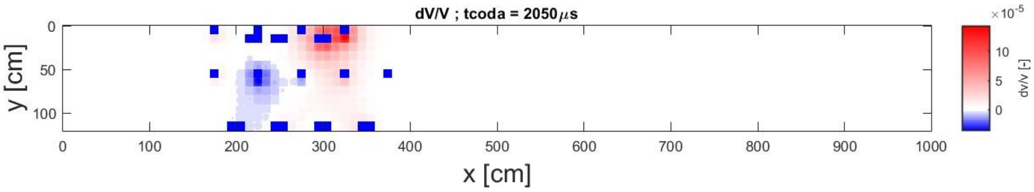

(b) Velocity plot for $t_{central} = 2050\mu s$.

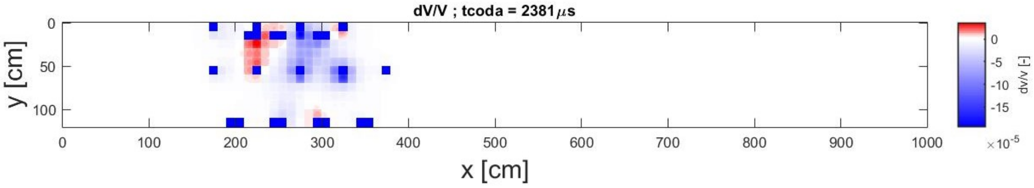

(c) Velocity plot for $t_{central} = 2381\mu s$.

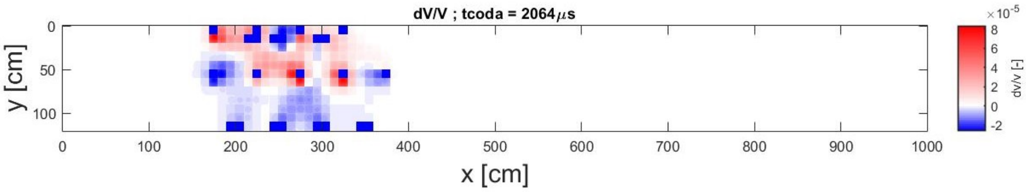

(d) Velocity plot for $t_{central} = 2064\mu s$.

Figure A.9: Four different combinations of velocity maps obtained with respect to the diffusive kernel approximation.

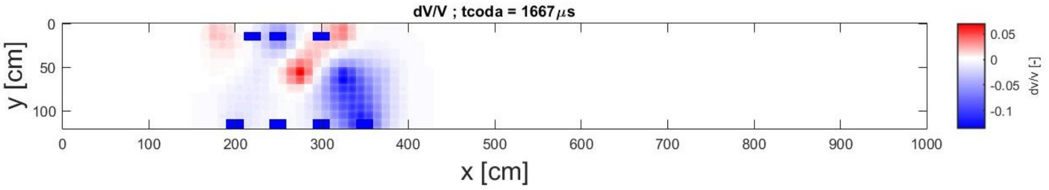

(a) Velocity plot for $t_{central} = 1667\mu s$.

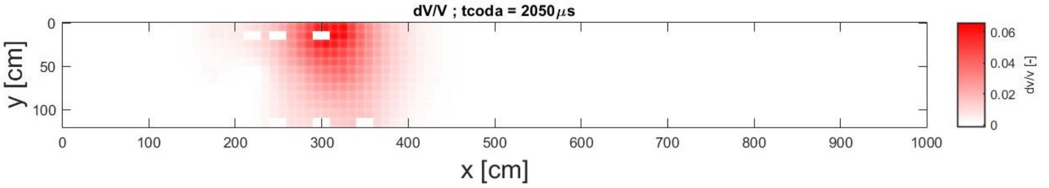

(b) Velocity plot for $t_{central} = 2050\mu s$.

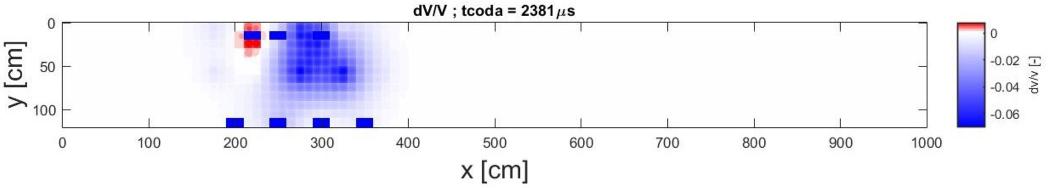

(c) Velocity plot for $t_{central} = 2381\mu s$.

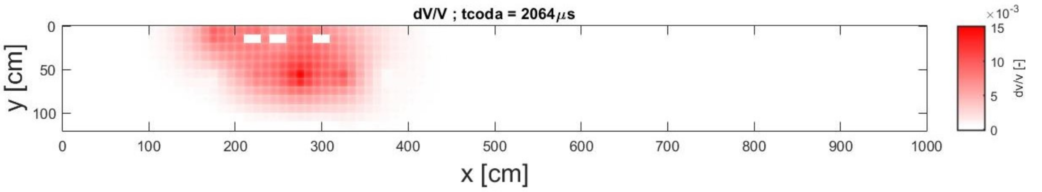

(d) Velocity plot for $t_{central} = 2064\mu s$.

Figure A.10: Four different combinations of velocity maps obtained with respect to the radiative transfer definition.

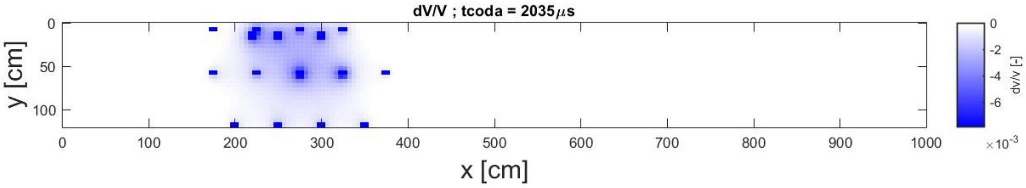

(a) Plot gained by diffusion approximation of sensitivity kernel

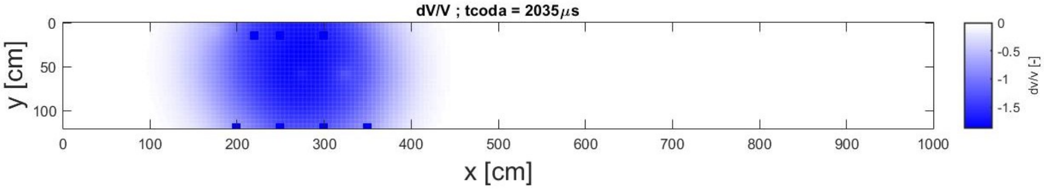

(b) Plot gained with respect to the radiative transfer kernel evaluation

Figure A.11: Overall averaged velocity plot for $t_{central}$ in between $1587\mu s$ and $2484\mu s$

B

Laboratory Study

B.1 Strecthing

B.1.1 Windows of Study

Stretched and unstretched signals of the synthetic perturbed data, with respect to their unperturbed references, are presented in this section. The windows length are $w = 120\mu s$ for the Figures B.1, B.2 and B.3. Figure B.4, instead, was tested with a time width of $1914\mu s$.

B.1.2 Parameters and Coefficients

Tables B.1, B.2 and B.3 were gained with respect to a stretching window of $120\mu s$. These tables represented the extracted stretched parameters as well as their correlation coefficients, for the windows and central instants of analysis, graphically characterised in Figures B.1, B.2, B.3 and B.4. It is immediate to verify the poor reliability index of such windows with respect to the overall signal; the colour scheme, chosen to identify the various correlation coefficients, was in accordance to the one developed for table A.6.

In addition to the three previously mentioned windows, a fourth (table B.4) was

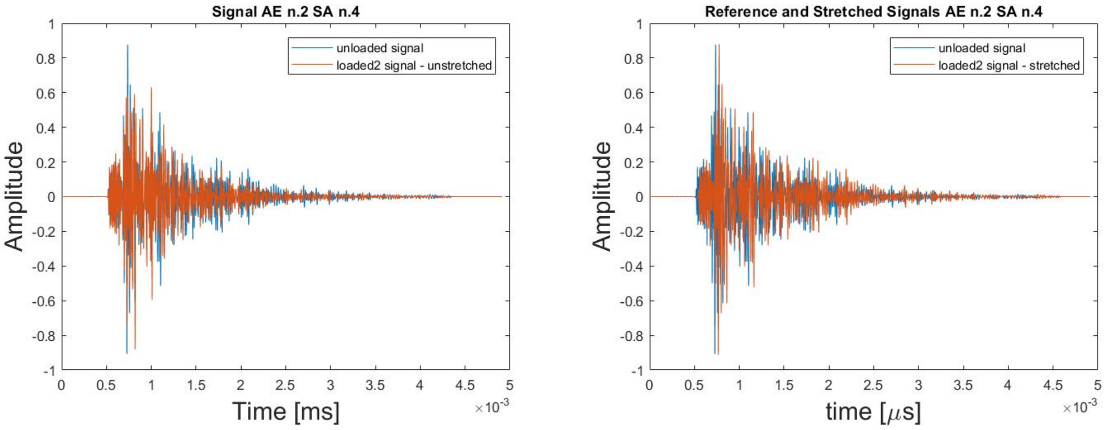

Figure B.1: Perturbed and unperturbed signals, stretched and non-stretched. Example for pair AE2-SA4.

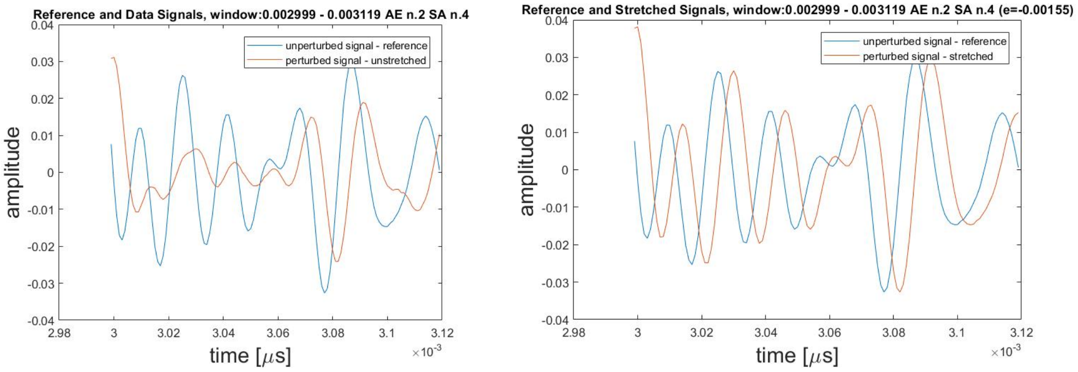

Figure B.2: Perturbed and unperturbed signals, stretched and non-stretched representing pair AE2-SA4. Window under study: $3439\mu s$ - $3559\mu s$

investigated to bring higher reliability to the data analysis. This had a $t_{central} = 3957$ for a width of $\Delta t = 1914\mu s$. Exactly like the synthetic analysis, all the stretching and correlation factors, derived for every $t_{central}$, were further proven by means of the comparisons with the averages parameters, extracted from smaller windows in the very same time length of study. This allowed to gain a stronger and more reliable data set for the successive phases. Nevertheless, the correlation coefficients were dangerously limiting to make them pass to the following step. Tables B.5, B.6 and B.7, instead, present higher correlation coefficients. Therefore, the values for the real CWI application are presented in these tables.

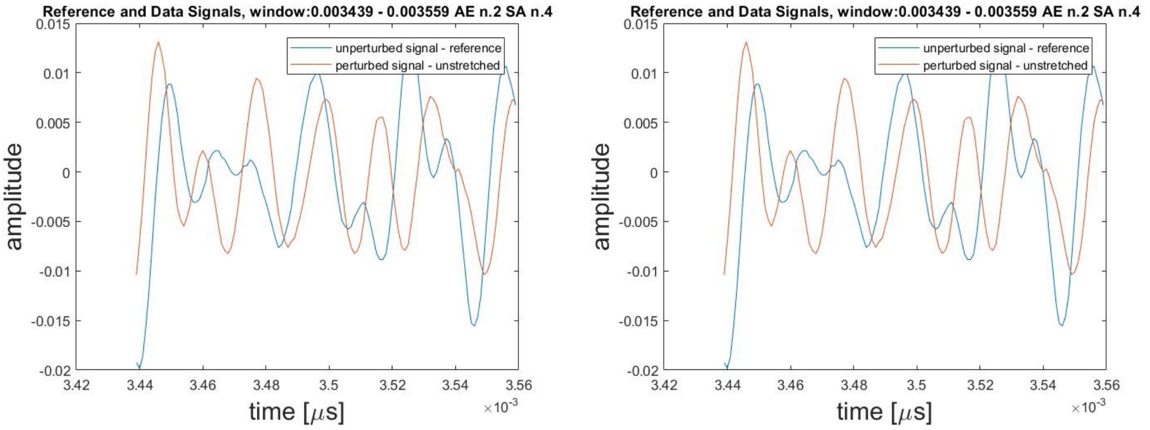

Figure B.3: Perturbed and unperturbed signals, stretched and non-stretched representing pair AE2-SA4. Window under study: 3059μs - 4059μs

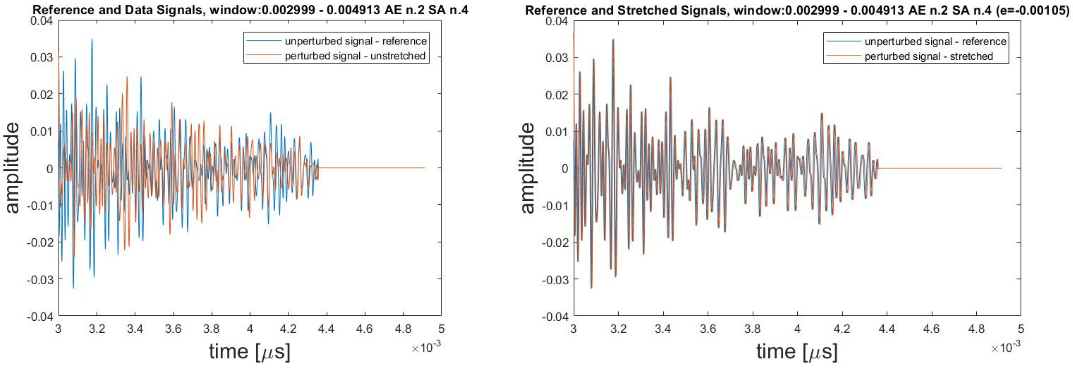

Figure B.4: Perturbed and unperturbed signals, stretched and non-stretched representing pair AE2-SA4. Window under study: 2999μs - 4913μs

B.2 Sensitivity Kernel

The sensitivity kernels for couple AE1-SA3 are presented at the end of Appendix B, for both graphical surface and mesh representations.

Table B.1: Stretching parameters and Correlation Coefficients for real data set with central time of the window $3060\mu s$ (colour settings analogous to table A.6).

	Window = $3000\mu s - 3120\mu s$									
	Epsilon					**Correlation**				
	SA1	**SA2**	**SA3**	**SA4**	**SA5**	**SA1**	**SA2**	**SA3**	**SA4**	**SA5**
AE1	8,75E-03	-1,35E-03	3,65E-03	-1,85E-03	8,65E-03	0,695657	0,826955	0,460313	0,689398	0,608733
AE2	-6,65E-03	-1,20E-03	-8,00E-04	-1,50E-03	5,80E-03	0,663902	0,895737	0,62488	0,643908	0,503774
AE3	-1,20E-03	-0,0008	-1,25E-03	-1,20E-03	-6,00E-04	0,722408	0,899744	0,566844	0,698016	0,944865
AE4	-9,50E-04	1,50E-04	5,00E-05	9,40E-03	7,50E-04	0,521754	0,795799	0,751777	0,511562	0,440701
AE5	-6,05E-03	-4,15E-03	-5,00E-04	-1,00E-02	-0,00105	0,289836	0,321037	0,591081	0,624093	0,762638
AE6	-1,05E-03	-5,00E-04	-7,50E-04	-1,10E-03	-6,00E-04	0,612087	0,807691	0,641768	0,770811	0,77687
AE7	-1,00E-03	-6,50E-04	9,55E-03	-5,00E-05	-8,05E-03	0,882611	0,741651	0,514807	0,800207	0,900664
AE8	-2,00E-04	-1,00E-02	-5,45E-03	-1,00E-04	-1,65E-03	0,740388	0,736664	0,309273	0,763233	0,847298
AE9	-1,40E-03	-0,00145	-7,00E-04	4,50E-04	-5,00E-05	0,836447	0,923289	0,785419	0,547343	0,698536
AE10	-4,50E-04	-1,50E-04	-2,25E-03	7,10E-03	8,45E-03	0,786374	0,823949	0,39349	0,655885	0,876053
AE11	-0,0023	-5,00E-05	9,80E-03	-2,50E-04	3,50E-04	0,454448	0,720325	0,577374	0,554292	0,620295
AE12	-1,00E-04	2,00E-04	-4,50E-04	9,50E-03	-3,50E-04	0,480857	0,737124	0,881964	0,609378	0,749665
AE13	-1,00E-04	-5,00E-04	8,10E-03	-8,00E-04	-8,50E-04	0,923104	0,98101	0,662199	0,867711	0,694689

Table B.2: Stretching parameters and Correlation Coefficients for real data set with central time of the window $3500\mu s$ (colour settings analogous to table A.6).

	Window = $3440\mu s - 3560\mu s$									
	Epsilon					**Correlation**				
	SA1	**SA2**	**SA3**	**SA4**	**SA5**	**SA1**	**SA2**	**SA3**	**SA4**	**SA5**
AE1	-1,75E-03	-1,10E-03	-6,45E-03	-6,55E-03	-2,20E-03	0,571712	0,638295	0,401427	0,438978	0,863249
AE2	-1,20E-03	-8,10E-03	-1,25E-03	-1,40E-03	-2,15E-03	0,856311	0,539575	0,832542	0,718904	0,788128
AE3	-1,75E-03	-0,00075	-1,35E-03	9,05E-03	6,85E-03	0,719113	0,846653	0,895151	0,316194	0,802152
AE4	-6,55E-03	5,50E-03	-8,40E-03	7,50E-04	6,65E-03	0,621231	0,662611	0,607334	0,63286	0,463228
AE5	-1,00E-03	6,10E-03	-9,65E-03	5,40E-03	-0,0004	0,639617	0,600362	0,64704	0,5242	0,928829
AE6	-7,00E-04	-7,00E-04	5,00E-03	6,50E-04	-8,55E-03	0,732811	0,646443	0,734522	0,595049	0,830725
AE7	-6,50E-04	-4,00E-04	-1,50E-04	-9,95E-03	-6,00E-04	0,608849	0,864929	0,570281	0,596747	0,646673
AE8	-4,00E-04	1,50E-04	8,05E-03	4,80E-03	-3,00E-04	0,589301	0,620934	0,821679	0,296881	0,688446
AE9	-9,00E-04	-0,00125	-5,00E-04	5,00E-04	-5,00E-04	0,576984	0,521766	0,715417	0,766613	0,887423
AE10	-9,15E-03	-1,50E-04	7,50E-04	7,35E-03	-7,05E-03	0,738833	0,684888	0,643117	0,649712	0,561643
AE11	-1,00E-04	-1,00E-04	2,00E-04	-7,00E-04	5,00E-05	0,661021	0,73197	0,518588	0,659624	0,863757
AE12	-1,25E-03	-3,00E-04	-1,60E-03	-1,50E-04	5,00E-04	0,891838	0,840161	0,755867	0,594517	0,785983
AE13	7,15E-03	-5,00E-04	-4,00E-04	5,05E-03	3,50E-04	0,873868	0,780234	0,720383	0,633405	0,862821

Table B.3: Stretching parameters and Correlation Coefficients for real data set with central time of the window 4060μs (colour settings analogous to table A.6).

	Window = $4000\mu s - 4120\mu s$									
	Epsilon					**Correlation**				
	SA1	**SA2**	**SA3**	**SA4**	**SA5**	**SA1**	**SA2**	**SA3**	**SA4**	**SA5**
AE1	-1,45E-03	-1,35E-03	1,55E-03	4,50E-03	-1,20E-03	0,696484	0,648153	0,349777	0,688093	0,760967
AE2	8,95E-03	4,65E-03	6,95E-03	-8,40E-03	-1,65E-03	0,883923	0,797084	0,666034	0,681736	0,564644
AE3	-9,75E-03	0,0092	-6,00E-04	-3,50E-04	-1,45E-03	0,881591	0,621875	0,890693	0,870161	0,84817
AE4	-8,35E-03	-6,15E-03	-7,95E-03	4,00E-04	5,00E-05	0,709544	0,51207	0,663438	0,571127	0,702053
AE5	-7,00E-04	6,60E-03	-1,80E-03	-1,35E-03	0,0041	0,775285	0,589772	0,664197	0,90865	0,523806
AE6	5,00E-05	-5,00E-05	8,85E-03	-9,50E-04	-1,60E-03	0,87977	0,79092	0,523814	0,678294	0,74027
AE7	-7,10E-03	6,75E-03	-7,25E-03	7,00E-04	-7,50E-04	0,410268	0,504179	0,620284	0,815317	0,76683
AE8	-7,00E-04	6,20E-03	-6,50E-04	-5,50E-04	-9,00E-04	0,809683	0,864741	0,933566	0,438228	0,898648
AE9	-1,35E-03	-0,0007	-5,00E-04	5,00E-05	-8,00E-04	0,712608	0,878831	0,798099	0,487137	0,916651
AE10	-9,80E-03	-1,00E-03	5,45E-03	8,30E-03	-1,20E-03	0,74137	0,722485	0,379506	0,479966	0,571079
AE11	-0,00145	-4,50E-04	8,65E-03	-5,00E-05	-5,35E-03	0,455991	0,666803	0,580102	0,665943	0,381575
AE12	-8,05E-03	-5,50E-04	7,10E-03	1,00E-04	-3,00E-04	0,618083	0,818642	0,723996	0,620549	0,761097
AE13	-7,50E-04	-6,25E-03	-7,75E-03	-8,25E-03	-6,00E-04	0,856639	0,803311	0,382577	0,85997	0,86085

Table B.4: Stretching parameters and Correlation Coefficients for real data set with central time of the window 3957μs and width = 1914μs (colour settings analogous to table A.6).

	Window = $3000\mu s - 4914\mu s$									
	Epsilon					**Correlation**				
	SA1	**SA2**	**SA3**	**SA4**	**SA5**	**SA1**	**SA2**	**SA3**	**SA4**	**SA5**
AE1	-1,17E-03	-1,11E-03	-1,12E-03	-1,75E-03	-1,17E-03	0,496069	0,518235	0,35936	0,338029	0,45398
AE2	-1,13E-03	-8,70E-04	-1,10E-03	-1,05E-03	-1,58E-03	0,46141	0,552411	0,439274	0,391567	0,448861
AE3	-6,85E-04	-0,00069	-6,45E-04	-3,90E-04	-8,50E-04	0,670499	0,783069	0,639708	0,643601	0,787615
AE4	-7,50E-05	-7,50E-05	1,25E-04	1,65E-04	-1,50E-05	0,515911	0,529044	0,454888	0,474841	0,596935
AE5	-8,70E-04	-9,95E-04	-4,80E-04	-6,70E-04	-0,00076	0,44574	0,478514	0,447243	0,437829	0,695968
AE6	-5,45E-04	-4,90E-04	-4,20E-04	-6,65E-04	-7,00E-04	0,516682	0,523881	0,447671	0,475633	0,589213
AE7	-1,13E-03	-4,45E-04	1,00E-05	-1,00E-04	-7,70E-04	0,69829	0,63229	0,474964	0,649841	0,652049
AE8	-5,80E-04	-5,20E-04	-6,50E-04	-3,25E-04	-7,00E-04	0,724708	0,578532	0,613526	0,617163	0,716329
AE9	-9,35E-04	-0,000615	-4,35E-04	1,40E-04	-2,35E-04	0,799952	0,80718	0,676573	0,829329	0,814614
AE10	-6,70E-04	-4,40E-04	-5,45E-04	1,50E-05	-8,75E-04	0,580874	0,662898	0,35452	0,460008	0,648288
AE11	7,50E-05	-1,10E-04	-2,35E-04	-5,35E-04	8,50E-05	0,587823	0,59077	0,47265	0,517217	0,657817
AE12	-8,00E-04	-3,10E-04	-4,30E-04	-1,50E-05	-2,80E-04	0,651486	0,667346	0,73844	0,73898	0,681911
AE13	-3,70E-04	-4,80E-04	-4,20E-04	-8,85E-04	-4,80E-04	0,76739	0,848585	0,514624	0,780406	0,78252

Table B.5: Table containing stretching parameters and Correlation Coefficients for a time window centred in $t_{central} = 3500\mu s$, with length $16\mu s$ (colour settings analogous to table 3.2).

	Window = $3492\mu s$ - $3508\mu s$									
	Epsilon					**Correlation**				
	SA1	**SA2**	**SA3**	**SA4**	**SA5**	**SA1**	**SA2**	**SA3**	**SA4**	**SA5**
AE1	3,60E-03	-1,70E-03	-6,20E-03	3,40E-03	-6,50E-03	0,918932	0,986413	0,988865	0,728246	0,990886
AE2	-3,60E-03	-7,30E-03	-5,70E-03	-8,00E-04	6,70E-03	0,989242	0,983332	0,940201	0,995549	0,987226
AE3	-1,00E-03	-0,0015	8,30E-03	-8,90E-03	-9,00E-04	0,991445	0,983246	0,989389	0,997918	0,999694
AE4	7,20E-03	7,00E-04	-7,40E-03	-3,90E-03	6,20E-03	0,981981	0,974245	0,996146	0,961675	0,987537
AE5	-9,00E-04	6,10E-03	-3,70E-03	-9,60E-03	0,0073	0,996592	0,990369	0,984079	0,947495	0,999844
AE6	-8,80E-03	-1,00E-03	5,10E-03	1,00E-02	-1,70E-03	0,917944	0,99753	0,961629	0,996964	0,981965
AE7	-6,60E-03	-3,00E-04	-5,80E-03	1,00E-04	-9,10E-03	0,991223	0,978852	0,996198	0,981058	0,676629
AE8	-9,00E-04	-1,00E-02	-5,00E-04	3,10E-03	-6,00E-04	0,995626	0,909433	0,99716	0,999679	0,909165
AE9	-4,00E-03	-0,0082	4,80E-03	-1,30E-03	1,00E-04	0,972402	0,999163	0,996234	0,990986	0,997359
AE10	1,40E-03	1,50E-03	1,00E-04	6,60E-03	5,10E-03	0,961165	0,994286	0,967218	0,963949	0,987575
AE11	-0,0003	-8,90E-03	-1,70E-03	5,00E-04	-6,00E-04	0,990177	0,946436	0,929666	0,978364	0,994206
AE1	-9,80E-03	4,70E-03	7,80E-03	-1,90E-03	4,00E-04	0,884084	0,994124	0,998286	0,972011	0,988287
AE13	7,30E-03	-8,20E-03	-4,20E-03	-7,00E-04	-3,00E-04	0,999645	0,968405	0,974284	0,99919	0,996838

Table B.6: Table containing stretching parameters and Correlation Coefficients for a time window centred in $t_{central} = 4060\mu s$, with length $16\mu s$ (colour settings analogous to table 3.2).

	Window = $4052\mu s$ - $4068\mu s$									
	Epsilon					**Correlation**				
	SA1	**SA2**	**SA3**	**SA4**	**SA5**	**SA1**	**SA2**	**SA3**	**SA4**	**SA5**
AE1	3,90E-03	3,60E-03	-9,30E-03	-7,30E-03	7,10E-03	0,942843	0,99787	0,991605	0,934117	0,96298
AE2	-2,80E-03	-6,00E-04	1,00E-04	-2,10E-03	4,70E-03	0,979027	0,982746	0,998354	0,994215	0,990328
AE3	-9,00E-04	-0,0061	-5,20E-03	-5,80E-03	-3,70E-03	0,999212	0,996828	0,971005	0,993166	0,926
AE4	-8,20E-03	-7,50E-03	-1,00E-04	7,30E-03	-3,60E-03	0,998968	0,997023	0,999313	0,982381	0,998125
AE5	-9,50E-03	-2,80E-03	2,70E-03	5,20E-03	-0,0052	0,979085	0,998064	0,996633	0,997261	0,998844
AE6	-1,00E-04	8,10E-03	7,50E-03	-3,50E-03	6,20E-03	0,996993	0,94865	0,989669	0,964289	0,997943
AE7	3,20E-03	3,10E-03	2,20E-03	-3,00E-04	3,60E-03	0,976094	0,901866	0,94642	0,992506	0,985828
AE8	-6,00E-04	-5,00E-04	-6,10E-03	-9,00E-04	8,70E-03	0,974643	0,993749	0,999404	0,986007	0,942825
AE9	-9,90E-03	-0,0069	5,20E-03	-9,10E-03	6,80E-03	0,9949	0,97401	0,998131	0,999654	0,998977
AE10	5,00E-03	-8,70E-03	-8,30E-03	9,10E-03	-5,00E-04	0,99437	0,994707	0,988775	0,996311	0,996544
AE11	-0,0061	6,70E-03	-2,40E-03	8,30E-03	2,60E-03	0,897603	0,968083	0,966563	0,986884	0,988306
AE1	-8,60E-03	-8,40E-03	7,10E-03	2,20E-03	-2,10E-03	0,990295	0,999411	0,999555	0,948693	0,978328
AE13	-5,70E-03	-1,20E-03	1,20E-03	-5,00E-04	-3,40E-03	0,995117	0,987159	0,974852	0,994543	0,976102

Table B.7: Table containing stretching parameters and Correlation Coefficients for a time window centred in $t_{central} = 3957\mu s$, with length $16\mu s$ (colour settings analogous to table 3.2).

	Window = $3949\mu s$ - $3965\mu s$									
	Epsilon					**Correlation**				
	SA1	**SA2**	**SA3**	**SA4**	**SA5**	**SA1**	**SA2**	**SA3**	**SA4**	**SA5**
AE1	-2,30E-03	5,50E-03	-9,70E-03	-1,40E-03	9,80E-03	0,99742	0,998494	0,965949	0,996702	0,989832
AE2	3,10E-03	-7,30E-03	-8,50E-03	2,00E-04	-1,90E-03	0,994957	0,880709	0,992987	0,989994	0,994846
AE3	9,10E-03	0,0074	8,50E-03	-6,30E-03	-8,30E-03	0,994278	0,989788	0,967738	0,991753	0,969237
AE4	5,00E-03	-7,20E-03	-8,70E-03	-5,80E-03	-1,00E-02	0,997401	0,986894	0,991174	0,987545	0,920182
AE5	3,70E-03	7,60E-03	3,40E-03	2,90E-03	-0,0013	0,996579	0,995486	0,994725	0,987374	0,996375
AE6	7,50E-03	8,30E-03	9,60E-03	7,10E-03	-9,30E-03	0,87475	0,975899	0,977026	0,893769	0,98575
AE7	-2,50E-03	-3,00E-04	-4,00E-04	4,40E-03	-4,30E-03	0,981431	0,755034	0,932347	0,788833	0,982366
AE8	2,90E-03	5,10E-03	9,10E-03	4,70E-03	8,70E-03	0,992911	0,999328	0,998016	0,973682	0,954179
AE9	-5,00E-04	-0,0007	-1,00E-02	3,00E-04	9,90E-03	0,984155	0,99921	0,977211	0,988432	0,996741
AE10	-6,70E-03	-7,60E-03	-3,00E-04	-1,60E-03	-1,90E-03	0,998074	0,998248	0,997308	0,985973	0,993561
AE11	0,0062	7,00E-04	7,40E-03	-6,00E-04	1,00E-02	0,985225	0,982816	0,994979	0,984064	0,994751
AE1	2,40E-03	9,20E-03	-5,00E-04	4,20E-03	6,20E-03	0,987774	0,98897	0,995547	0,989564	0,990921
AE13	3,00E-04	2,00E-04	4,00E-04	4,70E-03	-7,90E-03	0,998339	0,996697	0,999357	0,985237	0,999721

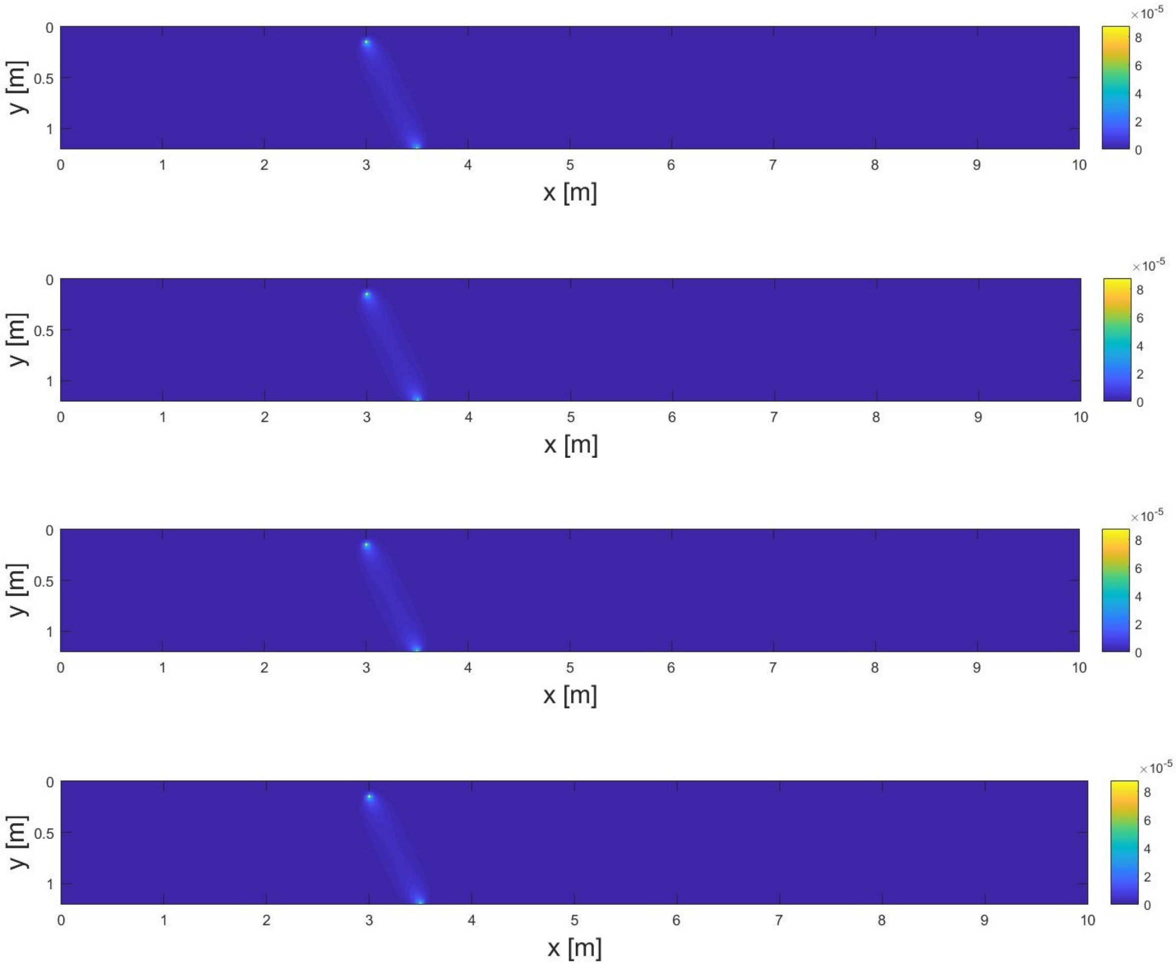

Figure B.5: Four Kernel surface representations for pair AE1-SA3. The time instants are, the same of Figure 4.8.

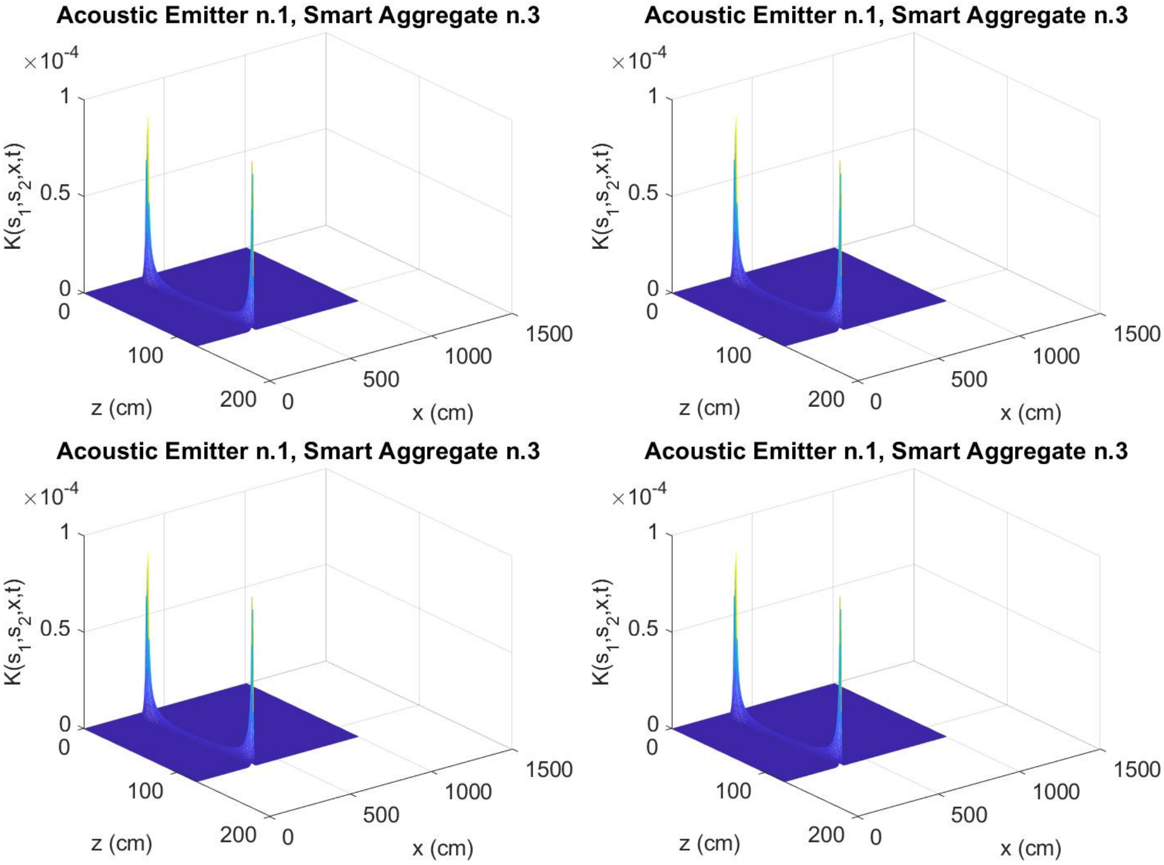

Acoustic Emitter n.1, Smart Aggregate n.3

Acoustic Emitter n.1, Smart Aggregate n.3

Acoustic Emitter n.1, Smart Aggregate n.3

Acoustic Emitter n.1, Smart Aggregate n.3

Figure B.6: Mesh representations for pair AE1-SA3 of the various kernels in Figure B.5. The central moments of analysis correspond to Figure 4.9

Bibliography

[1] Milton Abramowitz and Irene A Stegun. *Handbook of mathematical functions: with formulas, graphs, and mathematical tables*. Vol. 55. Courier Corporation, 1965.

[2] *Acoustoelastic effect - Wikipedia*. July 9, 2019. URL: `https://en.wikipedia.org/wiki/Acoustoelastic_effect`.

[3] Domitille Anache-Ménier. "Propagation des ondes dans les milieux désordonnés: étude de la phase des ultrasons et des ondes sismiques." PhD thesis. 2008.

[4] Phanidhar Anugonda, Joshua S. Wiehn, and Joseph A. Turner. "Diffusion of ultrasound in concrete". eng. In: *Ultrasonics* 39.6 (2001), pp. 429–435. ISSN: 0041-624X.

[5] Jérôme Azzola et al. "Direct modeling of the mechanical strain influence on coda wave interferometry". In: *Journal of Geophysical Research: Solid Earth* 123.4 (2018), pp. 3160–3177.

[6] S Banerji, A Bagchi, and S Khazaeli. "Energy harvesting methods for structural health monitoring using wireless sensors: a review". In: *Resilient Infrastructure, London 2016* (2016), pp. 1–10.

[7] Marek Barski et al. "Structural Health Monitoring (SHM) Methods in Machine Design and Operation". In: *Archive of Mechanical Engineering* 61.4 (Dec. 1, 2014), pp. 653–677. ISSN: 2300-1895. DOI: `10.2478/meceng-2014-0037`. URL: `http://journals.pan.pl/dlibra/publication/98509/edition/84946/content`.

[8] A. Behnia et al. "Integrated non-destructive assessment of concrete structures under flexure by acoustic emission and travel time tomography". eng. In: *Construction and Building Materials* 67 (2014), pp. 202–215. ISSN: 0950-0618.

[9] *Boltzmann distribution*. In: *Wikipedia*. Page Version ID: 918678331. Sept. 29, 2019. URL: `https://en.wikipedia.org/w/index.php?title=Boltzmann_distribution&oldid=918678331` (visited on 10/13/2019).

[10] Peter Bormann and Erhard Wielandt. "Seismic signals and noise". In: *New manual of seismological observatory practice* 2 (2002), pp. 1–62.

[11] Michel Campillo et al. "Monitoring the elastic properties of the crust: numerical analysis and applications using ambient seis-mic noise". In: (2013).

[12] Robby Caspeele, Luc Taerwe, and Dan M Frangopol. *Life Cycle Analysis and Assessment in Civil Engineering: Towards an Integrated Vision: Proceedings of the Sixth International Symposium on Life-Cycle Civil Engineering (IALCCE 2018), 28-31 October 2018, Ghent, Belgium.* Vol. 5. CRC Press, 2018.

[13] Guangzhi Chen. “Caractérisation de défauts dans les milieux multi-diffusants: analyse de la méthode non linéaire d’interférométrie de la coda ultrasonore”. PhD thesis. 2019.

[14] W. Chen, R. Mills, and R. S. Dwyer - Joyce. “Direct load monitoring of rolling bearing contacts using ultrasonic time of flight”. In: (2015). ISSN: 1364-5021.

[15] Kanu Chinaemerem. “Time-lapse monitoring of localized changes within heterogeneous media with scattered waves”. PhD thesis. Colorado School of Mines, 2014.

[16] Giorgia Coletta et al. “Ensemble Technique for Machine Learning with Application to Monitoring of Heritage Structures”. In: *Proceedings of the 13th International Conference on Damage Assessment of Structures*. Ed. by Magd Abdel Wahab. Singapore: Springer Singapore, 2020, pp. 333–349. ISBN: 9789811383304 9789811383311. DOI: `10.1007/978-981-13-8331-1_23`. URL: `http://link.springer.com/10.1007/978-981-13-8331-1_23`.

[17] R Courant, K Friedrichs, and H Lewyt. “On the Partial Difference Equations of Mathematical Physics”. In: (1967), p. 20.

[18] O. Coutant, A. Ratdomopurbo, and G. Poupinet. “On the use of earthquake multiplets to study fractures and the temporal evolution of an active volcano”. eng. In: *Annals of Geophysics* 39.2 (1996). ISSN: 1593-5213.

[19] *Critical Infrastructure Warning Information Network (CIWIN)*. Migration and Home Affairs - European Commission. Dec. 6, 2016. URL: `https://ec.europa.eu/home-affairs/what-we-do/networks/critical_infrastructure_warning_information_network_en` (visited on 09/10/2019).

[20] Joseph Davidson and Changki Mo. “Recent Advances in Energy Harvesting Technologies for Structural Health Monitoring Applications”. In: *Smart Materials Research* 2014 (2014), pp. 1–14. ISSN: 2090-3561, 2090-357X. DOI: `10.1155/2014/410316`. URL: `https://www.hindawi.com/archive/2014/410316/`.

[21] DR Dhakal et al. “Different techniques of structural health monitoring”. In: *Research and Development (IJCSEIERD)* 3.2 (2013), pp. 55–66.

[22] Richard Do. “Passive and active sensing technologies for structural health monitoring”. PhD thesis. UC San Diego, 2014.

[23] S.W. Doebling et al. *Damage identification and health monitoring of structural and mechanical systems from changes in their vibration characteristics: A literature review.* LA–13070-MS, 249299. May 1, 1996, LA–13070–MS, 249299. DOI: `10.2172/249299`. URL: `http://www.osti.gov/servlets/purl/249299-n4r7Vr/webviewable/`.

[24] Deyan Draganov and Elmer Ruigrok. “Passive seismic interferometry for subsurface imaging”. In: *Encyclopedia of earthquake engineering* (2014), pp. 1–13.

[25] Deyan Draganov et al. “High-Resolution Ultrasonic Imaging of Artworks with Seismic Interferometry for Their Conservation and Restoration”. In: *Studies in Conservation* 63.5 (July 4, 2018), pp. 277–291. ISSN: 0039-3630, 2047-0584. DOI: `10.1080/00393630.2018.1437870`. URL: `https://www.tandfonline.com/doi/full/10.1080/00393630.2018.1437870` (visited on 10/13/2019).

[26] Deyan Draganov et al. “Seismic interferometry, intrinsic losses and Q -estimation”. In: *Geophysical Prospecting* 58.3 (May 2010), pp. 361–373. ISSN: 00168025, 13652478. DOI: `10.1111/j.1365-2478.2009.00828.x`. URL: `http://doi.wiley.com/10.1111/j.1365-2478.2009.00828.x`.

[27] C. Du, Y. Yang, and D. A. Hordijk. “Experimental investigation on crack detection using imbedded smart aggregate”. English. In: *Life-Cycle Analysis and Assessment in Civil Engineering*. Ed. by Dan M. Frangopol, Robby Caspeele, and Luc Taerwe. CRC Press / Balkema - Taylor Francis Group, 2019, pp. 1199–1206. ISBN: 978-1-1386-2633-1.

[28] Luis Espinosa et al. “Accuracy on the time-of-flight estimation for ultrasonic waves applied to non-destructive evaluation of standing trees: a comparative experimental study”. In: *Acta Acustica united with Acustica* 104.3 (2018), pp. 429–439.

[29] C. R. Farrar and S. W. Doebling. “Damage Detection and Evaluation II”. In: *Modal Analysis and Testing*. Ed. by Júlio M. M. Silva and Nuno M. M. Maia. Dordrecht: Springer Netherlands, 1999, pp. 345–378. ISBN: 978-0-7923-5894-7 978-94-011-4503-9. DOI: `10.1007/978-94-011-4503-9_17`. URL: `http://link.springer.com/10.1007/978-94-011-4503-9_17`.

[30] Charles R. Farrar and Keith Worden. *Structural health monitoring: a machine learning perspective*. 1. ed. OCLC: 829058695. Chichester: Wiley, 2013. 631 pp. ISBN: 978-1-119-99433-6.

[31] Katharina Fischer, Francois Besnard, and Lina Bertling. “Reliability-centered maintenance for wind turbines based on statistical analysis and practical experience”. In: *IEEE Transactions on Energy Conversion* 27.1 (2011), pp. 184–195.

[32] EB Fokker and EN Ruigrok. “Quality parameters for passive image interferometry tested at the Groningen network”. In: *Geophysical Journal International* 218.2 (2019), pp. 1367–1378.

[33] *Fresnel zone*. In: *Wikipedia*. Page Version ID: 905476450. July 9, 2019. URL: `https://en.wikipedia.org/w/index.php?title=Fresnel_zone&oldid=905476450`.

[34] Akhilesh Ganti. *Correlation Coefficient Definition*. Investopedia. URL: `https://www.investopedia.com/terms/c/correlationcoefficient.asp` (visited on 08/08/2019).

[35] Amin Ghobadi. “Common type of damages in composites and their inspections”. In: *World Journal of Mechanics* 7.02 (2017), p. 24.

[36] Chaitan P Gupta. “Existence and uniqueness theorems for the bending of an elastic beam equation”. In: *Applicable Analysis* 26.4 (1988), pp. 289–304.

[37] Hiroki Ikeda and Ryota Takagi. “Coseismic changes in subsurface structure associated with the 2018 Hokkaido Eastern Iburi Earthquake detected using autocorrelation analysis of ambient seismic noise”. In: *Earth, Planets and Space* 71.1 (2019), p. 72.

[38] Hideaki Iwaki, Keiji Shiba, and Nobuo Takeda. "Structural health monitoring system using FBG-based sensors for a damage-tolerant building". eng. In: vol. 5057. 1. 2003, pp. 392–399. ISBN: 9780819448620.

[39] Milan Janic. "Integrated transport systems in the European Union: an overview of some recent developments". In: *Transport Reviews* 21.4 (2001), pp. 469–497.

[40] Hongki Jo et al. "Capacitance-based wireless strain sensor development". In: *Sensors and Smart Structures Technologies for Civil, Mechanical, and Aerospace Systems 2018*. Ed. by Hoon Sohn. Denver, United States: SPIE, Mar. 27, 2018, p. 26. ISBN: 978-1-5106-1692-9 978-1-5106-1693-6. DOI: `10.1117/12.2296716`.

[41] Chinaemerem Kanu and Roel Snieder. "Numerical computation of the sensitivity kernel for monitoring weak changes with multiply scattered acoustic waves". In: *Geophysical Supplements to the Monthly Notices of the Royal Astronomical Society* 203.3 (2015), pp. 1923–1936.

[42] Ioannis Karatzas and Steven E Shreve. "Brownian motion". In: *Brownian Motion and Stochastic Calculus*. Springer, 1998, pp. 47–127.

[43] Christopher Kevinly. "Application of coda-wave interferometry on concrete structures by utilizing smart aggregates". In: (2018), p. 140.

[44] Sakib Mahmud Khan et al. "Integration of structural health monitoring and intelligent transportation systems for bridge condition assessment: current status and future direction". In: *IEEE Transactions on Intelligent Transportation Systems* 17.8 (2016), pp. 2107–2122.

[45] Tribikram Kundu, ed. *Ultrasonic Nondestructive Evaluation: Engineering and Biological Material Characterization*. CRC Press, Dec. 29, 2003. ISBN: 978-0-8493-1462-9 978-0-203-50196-2. DOI: `10.1201/9780203501962`. URL: `https://www.taylorfrancis.com/books/9780203501962`.

[46] Tony Kuphaldt. *Lessons In Electric Circuits, Volume IV–Digital*. 2007.

[47] Eric Larose and Stephen Hall. "Monitoring stress related velocity variation in concrete with a 2× 10- 5 relative resolution using diffuse ultrasound". In: *The Journal of the Acoustical Society of America* 125.4 (2009), pp. 1853–1856.

[48] Eric Larose and Stephen Hall. "Monitoring stress related velocity variation in concrete with a 2 x 10(-5) relative resolution using diffuse ultrasound". eng. In: *The Journal of the Acoustical Society of America* 125.4 (2009), p. 1853. ISSN: 1520-8524.

[49] Eric Larose et al. "Locating and characterizing a crack in concrete with diffuse ultrasound: A four-point bending test". In: *The Journal of the Acoustical Society of America* 138.1 (July 2015), pp. 232–241. ISSN: 0001-4966. DOI: `10.1121/1.4922330`. URL: `http://asa.scitation.org/doi/10.1121/1.4922330`.

[50] Eric Larose et al. "Observation of multiple scattering of kHz vibrations in a concrete structure and application to monitoring weak changes". In: *Physical Review E* 73.1 (2006), p. 016609.

[51] Steven Lovejoy. "APPLICATIONS OF STRUCTURAL HEALTH MONITORING TO HIGHWAY BRIDGES". In: (), p. 23.

[52] R Marklein et al. “Ultrasonic and electromagnetic wave propagation and inverse scattering applied to concrete”. In: *Review of progress in quantitative nondestructive evaluation*. Springer, 1996, pp. 1839–1846.

[53] *Marshall Plan*. July 9, 2019. URL: `http://en.wikipedia.org/wiki/Marshall%20Plan`.

[54] *MATLAB - Il linguaggio del calcolo tecnico*. URL: `https://it.mathworks.com/products/matlab.html` (visited on 09/17/2019).

[55] T Dylan Mikesell et al. “A comparison of methods to estimate seismic phase delays: Numerical examples for coda wave interferometry”. In: *Geophysical Journal International* 202.1 (2015), pp. 347–360.

[56] Burkhard Monien, Wojciech Rytter, and Leopold SchaPers. “Fast recognition of deterministic cfl’s with a smaller number of processors”. eng. In: *Theoretical Computer Science* 116.2 (1993), pp. 421–429. ISSN: 0304-3975.

[57] *Murnaghan equation of state*. In: *Wikipedia*. Page Version ID: 911060918. Aug. 16, 2019. URL: `https://en.wikipedia.org/w/index.php?title=Murnaghan_equation_of_state&oldid=911060918` (visited on 09/10/2019).

[58] Francis Dominic Murnaghan. *Finite deformation of an elastic solid*. Wiley, 1951.

[59] Ernst Niederleithinger et al. “Embedded Ultrasonic Transducers for Active and Passive Concrete Monitoring”. In: *Sensors* 15.5 (Apr. 27, 2015), pp. 9756–9772. ISSN: 1424-8220. DOI: `10.3390/s150509756`. URL: `http://www.mdpi.com/1424-8220/15/5/9756`.

[60] Ernst Niederleithinger et al. “Processing ultrasonic data by coda wave interferometry to monitor load tests of concrete beams”. In: *Sensors* 18.6 (2018), p. 1971.

[61] Anne Obermann et al. “4-D Imaging of Subsurface Changes with Coda Waves: Numerical Studies of 3-D Combined Sensitivity Kernels and Applications to the Mw7.9, 2008 Wenchuan Earthquake”. In: *Pure and Applied Geophysics* 176.3 (2019), pp. 1243–1254.

[62] Anne Obermann et al. “Depth sensitivity of seismic coda waves to velocity perturbations in an elastic heterogeneous medium”. In: *Geophysical Journal International* 194.1 (July 1, 2013), pp. 372–382. ISSN: 1365-246X, 0956-540X. DOI: `10.1093/gji/ggt043`. URL: `http://academic.oup.com/gji/article/194/1/372/641325/Depth-sensitivity-of-seismic-coda-waves-to`.

[63] Anne Obermann et al. “Lapse-time-dependent coda-wave depth sensitivity to local velocity perturbations in 3-D heterogeneous elastic media”. In: *Geophysical Journal International* 207.1 (Oct. 1, 2016), pp. 59–66. ISSN: 0956-540X, 1365-246X. DOI: `10.1093/gji/ggw264`. URL: `https://academic.oup.com/gji/article-lookup/doi/10.1093/gji/ggw264`.

[64] A. Obermann et al. “Seismic noise correlations to image structural and mechanical changes associated with the *M* ¡i¿w¡/i¿ 7.9 2008 Wenchuan earthquake”. In: *Journal of Geophysical Research: Solid Earth* 119.4 (Apr. 2014), pp. 3155–3168. ISSN: 21699313. DOI: `10.1002/2013JB010932`. URL: `http://doi.wiley.com/10.1002/2013JB010932`.

[65] *Official website of the European Union*. European Union. June 17, 2016. URL: `https://europa.eu/european-union/index_en` (visited on 07/03/2019).

[66] J.C.J. Paasschens. “Solution of the time-dependent Boltzmann equation”. In: *Physical Review E - Statistical Physics, Plasmas, Fluids, and Related Interdisciplinary Topics* 56.1 (1997), pp. 1135–1141. ISSN: 1063651X.

[67] Carlos Pacheco and Roel Snieder. “Time-lapse travel time change of multiply scattered acoustic waves”. In: *The Journal of the Acoustical Society of America* 118.3 (Sept. 2005), pp. 1300–1310. ISSN: 0001-4966. DOI: `10.1121/1.2000827`. URL: `http://asa.scitation.org/doi/10.1121/1.2000827`.

[68] John H Page et al. “Classical wave propagation in strongly scattering media”. In: *Physica A: Statistical Mechanics and its Applications* 241.1-2 (1997), pp. 64–71.

[69] Gyuhae Park et al. “Energy harvesting for structural health monitoring sensor networks”. In: *Journal of Infrastructure Systems* 14.1 (2008), pp. 64–79.

[70] T. Planès and E. Larose. “A review of ultrasonic Coda Wave Interferometry in concrete”. In: *Cement and Concrete Research* 53 (Nov. 2013), pp. 248–255. ISSN: 00088846. DOI: `10.1016/j.cemconres.2013.07.009`. URL: `https://linkinghub.elsevier.com/retrieve/pii/S0008884613001701`.

[71] Thomas Planès. “Imagerie de chargements locaux en régime de diffusion multiple”. PhD thesis. Grenoble, 2013.

[72] Thomas Planès et al. “Decorrelation and phase-shift of coda waves induced by local changes: multiple scattering approach and numerical validation”. In: *Waves in Random and Complex Media* 24.2 (2014), pp. 99–125.

[73] H Politano and A Pouquet. “von Kármán–Howarth equation for magnetohydrodynamics and its consequences on third-order longitudinal structure and correlation functions”. In: *Physical Review E* 57.1 (1998), R21.

[74] Matteo Pozzi and Armen Der Kiureghian. “Assessing the value of information for long-term structural health monitoring”. eng. In: vol. 7984. 1. 2011, 79842W–79842W-14.

[75] A. Raghavan and C. E. S. Cesnik. “Review of Guided-wave Structural Health Monitoring”. In: *The Shock and Vibration Digest* 39.2 (Mar. 1, 2007), pp. 91–114. ISSN: 0583-1024. DOI: `10.1177/0583102406075428`. URL: `http://svd.sagepub.com/cgi/doi/10.1177/0583102406075428`.

[76] Mohammad Riahi and Alireza Ahmadi. “Comparison and analysis of two modern methods in the structural health monitoring techniques in aerospace”. eng. In: vol. 9804. SPIE, 2016, 98041Y–98041Y-7. ISBN: 9781510600454.

[77] Sheldon M. Ross. *Introduction to probability models*. Eleventh edition. Amsterdam ; Boston: Elsevier, 2014. 767 pp. ISBN: 978-0-12-407948-9.

[78] Vincent Rossetto et al. “Locating a weak change using diffuse waves: Theoretical approach and inversion procedure”. In: *Journal of Applied Physics* 109.3 (Feb. 2011), p. 034903. ISSN: 0021-8979, 1089-7550. DOI: `10.1063/1.3544503`. URL: `http://aip.scitation.org/doi/10.1063/1.3544503`.

[79] Haruo Sato, Michael C. Fehler, and Takuto Maeda. *Seismic Wave Propagation and Scattering in the Heterogeneous Earth : Second Edition.* Berlin, Heidelberg: Springer Berlin Heidelberg, 2012. ISBN: 978-3-642-23028-8 978-3-642-23029-5. DOI: `10.1007/978-3-642-23029-5`. URL: `http://link.springer.com/10.1007/978-3-642-23029-5`.

[80] Dennis P. Schurr et al. "MONITORING DAMAGE IN CONCRETE USING DIFFUSE ULTRASONIC CODA WAVE INTERFEROMETRY". In: REVIEW OF PROGRESS IN QUANTITATIVE NONDESTRUCTIVE EVALUATION: Volume 30A; Volume 30B. San Diego, California, (USA), 2011, pp. 1283–1290. DOI: `10.1063/1.3592081`. URL: `http://aip.scitation.org/doi/abs/10.1063/1.3592081`.

[81] Lawrence A. Shepp. *Computed tomography.* eng. Proceedings of symposia in applied mathematics 27. Providence: AMS, 1983.

[82] Roel Snieder. "Coda wave interferometry and the equilibration of energy in elastic media". In: *Physical Review E* 66.4 (Oct. 21, 2002), p. 046615. ISSN: 1063-651X, 1095-3787. DOI: `10.1103/PhysRevE.66.046615`. URL: `https://link.aps.org/doi/10.1103/PhysRevE.66.046615`.

[83] ROEL SNIEDER, ALEJANDRO DURAN, and ANNE OBERMANN. "Locating velocity changes in elastic media with coda wave interferometry". In: *Seismic Ambient Noise* (2019), p. 188.

[84] Hoon Sohn et al. *A review of structural health monitoring literature : 1996-2001.* eng. LA-13976-MS. Los Alamos: Los Alamos national laboratory, 2001.

[85] Gangbing Song, Haichang Gu, and Yi-Lung Mo. "Smart aggregates: multi-functional sensors for concrete structuresa tutorial and a review". eng. In: *Smart Materials and Structures* 17.3 (2008), p. 033001. ISSN: 0964-1726.

[86] W. J. Staszewski, C. Boller, and Geoffrey R. Tomlinson, eds. *Health monitoring of aerospace structures: smart sensor technologies and signal processing.* West Sussex, England: Hoboken, NJ : J. Wiley, 2004. 266 pp. ISBN: 978-0-470-84340-6.

[87] *Structural health monitoring.* In: *Wikipedia.* Page Version ID: 909239402. Aug. 4, 2019. URL: `https://en.wikipedia.org/w/index.php?title=Structural_health_monitoring&oldid=909239402` (visited on 08/14/2019).

[88] Zhen Sun and Hongbin Sun. "Jiangyin Bridge: An Example of Integrating Structural Health Monitoring with Bridge Maintenance". eng. In: *Structural Engineering International* 28.3 (2018), pp. 353–356. ISSN: 1016-8664. URL: `http://www.tandfonline.com/doi/abs/10.1080/10168664.2018.1462671`.

[89] Albert Tarantola and Bernard Valette. "Generalized nonlinear inverse problems solved using the least squares criterion". In: *Reviews of Geophysics* 20.2 (1982), pp. 219–232.

[90] Valerian Ilich Tatarski. *Wave propagation in a turbulent medium.* Courier Dover Publications, 2016.

[91] Peter Temin. "The golden age of European growth reconsidered". In: *European Review of Economic History* 6.1 (2002), pp. 3–22.

[92] Idriss El-Thalji and Jayantha Liyanage. "Integrated asset management practices for Offshore wind power industry: A Critical review and a Road map to the future". In: vol. 1. June 2010.

[93] Idriss El-Thalji, Jayantha P Liyanage, et al. “Integrated asset management practices for Offshore wind power industry: A Critical review and a Road map to the future”. In: *The Twentieth International Offshore and Polar Engineering Conference*. International Society of Offshore and Polar Engineers. 2010.

[94] Jan Thorbecke. “2D Finite-Difference Wavefield Modelling”. In: (2019), p. 66.

[95] J A Turner and P Anugonda. “Scattering of elastic waves in heterogeneous media with local isotropy”. eng. In: *The Journal of the Acoustical Society of America* 109.5 Pt 1 (2001), p. 1787. ISSN: 0001-4966.

[96] Cornelis Weemstra et al. “Seismic attenuation from recordings of ambient noiseAttenuation from ambient noise”. In: *Geophysics* 78.1 (2013), Q1–Q14.

[97] Cornelis Weemstra et al. “Time-lapse seismic imaging of the Reykjanes geothermal reservoir”. In: *EGU General Assembly 2016, 2016-04-17 2016-04-22, Austria Center Vienna, Vienna, Austria* (2016), p. 10.

[98] Jan Wenske. “Science & Research Abstract for EWEA 2016 Annual Conference/WindEurope Summit 2016, Hamburg, 27-30 September 2016”. In: *WindEurope Summit 2016, Hamburg, 27-30 September 2016* (2016).

[99] *What is Hooke’s Law?* Khan Academy. July 9, 2019. URL: `https://www.khanacademy.org/science/physics/work-and-energy/hookes-law/a/what-is-hookes-law` (visited on 09/10/2019).

[100] T-T Wu and T-F Lin. “The stress effect on the ultrasonic velocity variations of concrete under repeated loading”. In: *Materials Journal* 95.5 (1998), pp. 519–524.

[101] Yaowen Yang and Yuhang Hu. “Electromechanical impedance modeling of pzt transducers for health monitoring of cylindrical shell structures”. eng. In: *Smart Materials and Structures* 17.1 (2008), p. 015005. ISSN: 0964-1726.

[102] Y. Yang et al. “A comparative study of acoustic emission tomography and digital image correlation measurement on a reinforced concrete beam”. English. In: *Life-Cycle Analysis and Assessment in Civil Engineering*. Ed. by Dan M. Frangopol, Robby Caspeele, and Luc Taerwe. CRC Press / Balkema - Taylor Francis Group, 2019, pp. 2419–2426. ISBN: 978-1-1386-2633-1.

[103] Yuxiang Zhang et al. “Diffuse ultrasound monitoring of stress and damage development on a 15-ton concrete beam”. In: *The Journal of the Acoustical Society of America* 139.4 (Apr. 2016), pp. 1691–1701. ISSN: 0001-4966. DOI: `10.1121/1.4945097`. URL: `http://asa.scitation.org/doi/10.1121/1.4945097`.

[104] Yuxiang Zhang et al. “Three-dimensional in-situ imaging of cracks in concrete using diffuse ultrasound”. In: *Structural Health Monitoring* 17.2 (Mar. 2018), pp. 279–284. ISSN: 1475-9217, 1741-3168. DOI: `10.1177/1475921717690938`. URL: `http://journals.sagepub.com/doi/10.1177/1475921717690938`.

[105] Daniel Zymelka et al. “Printed strain sensor with temperature compensation and its evaluation with an example of applications in structural health monitoring”. eng. In: *Japanese Journal of Applied Physics* 56.5S2 (2017), 05EC02. ISSN: 00214922.